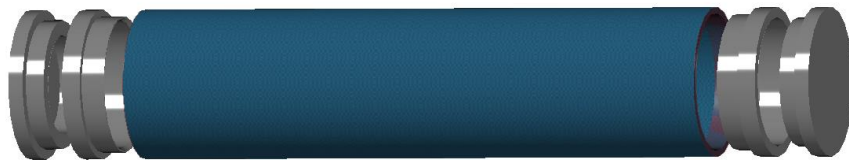National Technical University of Athens

School of Naval Engineering and Marine Architecture

Shipbuilding Technology Laboratory

Diploma Thesis

Adhesive Joining of Metal End-caps to Composite Pressure Vessels

Korina Zervou

Thesis supervisors: Professor N. Tsouvalis & Professor N. Carrere

March 2023

Acknowledgements

With this work my undergraduate studies come to an end, and this is an outcome of, among others, long-lasting efforts of many people who contributed and whom I would like to thank.

I would like to express my gratitude to my supervisor professor at NTUA, Nicholas Tsouvalis, for his guidance, patience, and willingness to provide help and feedback for any issue. His punctiliousness has kept me improving throughout my diploma thesis project.

As a major part of this thesis took place at ENSTA Bretagne and at Dupuy de Lome Research Institute (IRDL) I would like to thank all the people that made this collaboration fruitful. I wish to express my gratitude to my supervisor professor at ENSTA Bretagne, Nicolas Carrere, for all his guidance and assistance during my stay in Brest. I am also thankful to Georgios Stamoulis for all the advice and aid he provided.

I am obliged to Naval Group for all the aid and resources they provided. I would like to extend a special thanks to Emilien Billaudeau and Maëlle Sergolle for their helpful comments and support on this thesis.

To my companion in this experience, Catherine Chatzipli, with whom we developed our diploma theses in parallel and under the same general project, this would not have been such an interesting journey without you. Thank you for being a helpful and inspiring colleague, but most importantly, a valuable friend. Thank you for sharing your unique way of thinking, your positivity and motivation with me.

I would like to give my profound thanks to my parents, my sister and my friends for their love, support and encouragement during this process. Without you, mum and dad, this journey would not have been possible.

Last but not the least, a sincere thanks to my dear, Alex Argyris, for deeply understanding, believing and wholeheartedly standing by me from the beginning till the end, even when great distance separated us.

Abstract

The use of composite materials is becoming increasingly wider in marine industry due to their light weight, high strength and corrosion resistance, leading to energy-saving structures. In parallel, the application of the adhesive joints, instead of conventional bolted or welded connections, is gaining great interest especially in structural components made of fiber-reinforced composites. This joining method is preferred since it offers the possibility of joining dissimilar materials, prevents from local damage of fibers and introduction of stress concentrations, traditionally caused by the fastener holes. Additional advantages like the water-tightness of an adhesively bonded structure and the possibility of on the spot maintenance, without need of dry docking, make the adhesive joining even more desirable in the field of composite pressure vessels used for underwater applications.

The efficient design of a composite pressure vessel, including an adhesive joint between a composite cylinder and a metal end-cap, is a challenging task. It combines the difficulty in understanding composite materials structural behavior, due to their anisotropic nature, the limited literature and lack of design rules regarding complicated adhesive joint configurations. Moreover, since the analysis of the mechanical behavior of the composite cylinder and the adhesive joint constitute two separated issues, structural analyses, including both issues, from literature are hard to find.

In the context of this work, the design of the adhesive joint configuration between a filament wound pressure vessel and aluminum end-caps is examined, resulting in a series of proposed design concepts. Afterwards, the finite element modelling of the proposed designs of the pressure vessel with the adhesively attached aluminum end-caps is investigated under hydrostatic pressure, using ABAQUS software.

The first finite element model simulates a 10° slice of the half of the pressure vessel, using 3D solid elements. It is used for a linear static analysis, focusing on the adhesive joint area. The dominant failure mode and its location are determined. Since this slice model is cost-saving, a parametric study is conducted in order to examine the effect of geometry, stacking sequence and material properties variation. The conclusions of the parametric study are applied in the model in order to optimize the structural design and minimize the risk of failure.

The second finite element model simulates the full cylindrical structure, including the composite cylinder, the metal parts and the adhesive joints between them, using 3D solid elements. It is used for validating the results of the corresponding slice model, for conducting an eigenvalue buckling and a nonlinear buckling analysis. The latter is crucial for the final optimization as it is closer to real-life conditions. Following the whole study, the optimized design in terms of structural reliability, functionality and manufacturing feasibility is reached.

Contents

Nomenclature

Abbreviations

AE Acoustic Emission
ASME American Society of Mechanical Engineers
AUV Autonomous Underwater Vehicles
BC Boundary Conditions
BV Bureau Veritas
BPVC Boiler and Pressure Vessel Code
CC Coupled Criterion
CZM Cohesive Zone Model
DC Design Concept
DCB Double Cantilever Beam
DLJ Double Lap Joint
DOF Degree of Freedom
DSV Deep Submergence Vehicle
ENF End-Notched Flexure
ENS End Loaded Split
FE Finite Element
FEM Finite Element Method
FRP Fiber-Reinforced Polymers
FW Filament Winding
IMO International Maritime Organization
MCS Mesh Convergence Study
NDT Non Destructive Testing
SLJ Single Lap Joint
VCCT Virtual Crack Closure Technique

Stresses

$\sigma_{xx}, \sigma_{yy}, \sigma_{zz}$ the stress in x-axis, in y-axis and in z-axis directions respectively in a Cartesian coordinate system

$\tau_{xy}, \tau_{yz}, \tau_{xz}$ the shear stress in x-y plane, y-z plane and x-z plane respectively in a Cartesian coordinate system

S11, S22, S33 the stress in radial (r), in circumferential (θ) and in axial (z) directions respectively in a cylindrical coordinate system (Figure A)

S12, S23, S13 the shear stress in r-θ plane, in θ-z plane and in r-z plane respectively in a cylindrical coordinate system (Figure A)

Sff, Spp, Snn the stress aligned with the fiber direction (f), perpendicular to the fiber direction (p) and normal to the plane of the ply (p) directions respectively in a local laminate coordinate system (Figure B)

Sfp, Spn, Sfn the shear stress in f-p plane, in p-n plane and in f-n plane respectively in a local laminate coordinate system (Figure B)

Displacements

U1, U2, U3   the displacement in radial (r), in circumferential (θ) and in axial (z) directions respectively in a cylindrical coordinate system

UR1, UR2, UR3 the rotational displacements around the radial (r), circumferential (θ) and axial (z) directions respectively in a cylindrical coordinate system
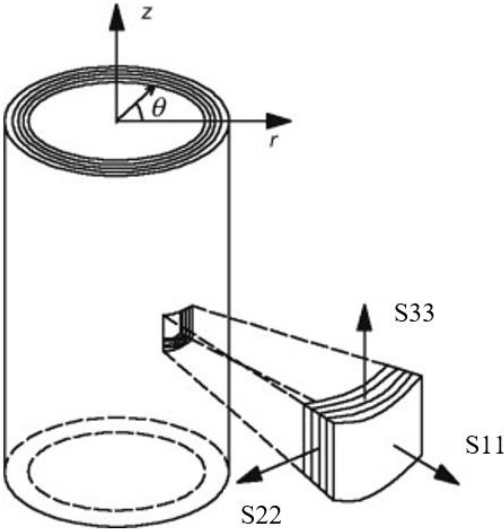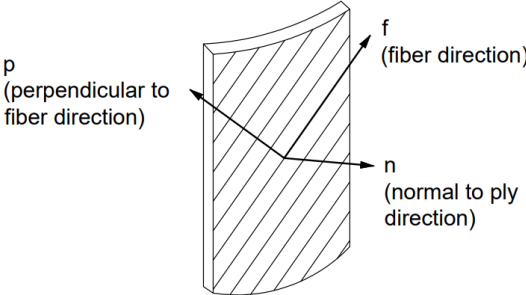

Figure A Cylindrical coordinate system

Figure B Local laminate coordinate system

CHAPTER 1

Introduction in joining metal end caps to composite pressure vessels

1.1 Composite materials and their use in marine applications

1.1.1 A brief introduction to composite materials

The process of introducing and developing structural materials for ship construction is endless. For centuries, wood was the main shipbuilding material until ship builders realized that ships built in iron or steel were stronger, lighter, and easier to maintain than those made of wood. During the 1960s composites were widely used in boat building industry in recreational, commercial and military industries. Through the following years, considerable progress has been made on developing the fabrication techniques and on understanding the behavior of these materials and the tailored structures under mechanical, thermal and fire induced load scenarios. Recently, as the IMO's environmental regulations have been strengthened requiring energy saving and eco-friendly material technology, the IMO has also begun to consider operational economics such as energy reduction through lightening the hull. Demand for lighter weight technology using composite materials is increasing. Examples would include lightweight large structures using composite materials, composite materials replacing metal design parts, and polymer composite materials applicable to marine environments.

The term composite materials signifies that two or more components are combined so that the properties of the final material are better than the properties of the components separately. This kind of materials consists of the matrix which sets up the part geometrically, gives cohesion to the material, it is usually flexible and not very resistant and transmits loading from one fiber to another and the reinforcement which provides rigidity and resistance. Composite materials, with specific reference to fiber-reinforced polymers (FRP), have been extensively incorporated in the marine industry thanks to the high strength-to weight ratio. According to Rubino et al. (2020), additional advantages of FRP are the ability to tailor the layup for optimum strength and stiffness offering excellent properties, improved fatigue life, corrosion resistance, and (with good design practice) reduced assembly costs due to fewer detail parts and fasteners.

Composite materials have been used for diverse applications ranging from high performance composites used in sailboats racing in the America's Cup or in Route du Rhum, to less sophisticated applications of glass reinforced polymers used in fishing boats (Chen et al., 2003). Nowadays, composite materials are increasingly being applied to commercial high-speed ships both catamarans and monohulls. Ship hulls in composite materials can usually be regarded as assemblies of a series of stiffened composite panels. Marine composite applications include mast and propeller, and other components for recreational or racing sailboats, like the trimaran shown in Figure 1.1. Composites can be found in many more areas of a maritime vessel, including interior mouldings and furniture on super yachts.

Figure 1.1 Racing sailboat made of CFRP, participating in Route du Rhum

The use of composites in the integrated superstructure started from naval ships since it reduces the weight and center of gravity of the hull structure but also improves the stability and speed of the ship. Except for the superstructure, naval ships have composite sonar domes, manufactured with vacuum resin transfer molding as presented in the Figure 1.2.

Figure 1.2 Composite sonar under construction [Holland composites]

When it comes to engineering parts that can withstand the sea loading, composites have the advantage over traditional materials. Composite materials can be custom-made to: resist corrosion, withstand water pressure at great depths, provide water-tight seals, as well as meet many other specific requirements. Many traditional rubber parts for example, which were once used as marine gaskets, are now being made from much stronger composite materials. The same goes for components used in marine engine, propulsion and pump system including bearings, ducts, shafts, piping, even propellers and rudders. As the marine industry continues to push for

more energy-efficient engines, and better preforming parts, the reliance on composites to improve efficiency is growing (Rubino et al., 2020).

Composites have been used underwater for many years. The main industries concerned today are offshore oil and gas, oceanography, and military. Composite materials are usually chosen in oil and gas exploration and production field due to their corrosion resistance and compatibility with the chemicals used downhole and offshore. Razavi Setvati et al. (2014) presents a list of composite applications in offshore marine industry including aqueous piping system, water and fuel storage tanks, low pressure composite valves, floating risers, and sub-sea structural components. The composites play their role also in submersibles. According to Mouritz et al. (2001), covering the steel hull of a submarine with composite panels is expected to increase the overall buckling strength, lower fatigue strain, reduce corrosion and lower the acoustic, magnetic, and electric signatures.

Composite materials are also being used in external and internal hull structures in smaller submersibles. Conventional submersibles feature steel, aluminum or titanium internal pressure hulls. Metallic hulls, however, because they are not buoyant in designs for depths of more than 2,000m, present challenges when it comes to managing ballast for ascent and descent. In particular, metal-hulled craft require the use of syntactic foam attached to the outside of the craft to achieve neutral buoyancy. In 2014, submersibles manufacturer OceanGate Inc. (Seattle, WA, US) was coming off the successful launch of "Cyclops 1", its steel-hulled craft, rated for underwater exploration to a depth of 500m. In 2016, the company was set to embark on development of "Titan", a cyclops-class submersible, designed for a maximum depth of 4,000m, replacing the metallic hull with a composite one. Figure 1.3 shows the structural configuration of "Titan".

OceanGate signed a contract with Spencer Composites Inc. for the "Titan" carbon-fiber/epoxy internal hull in early January 2017 and was presented with the following parameters: Length, 2,540 mm; outside diameter, 1,676 mm; service pressure, 6,600 psi; pressure safety factor, 2.25. According to Spencer Composites Inc. the thickness of the internal composite cylinder was estimated using micromechanics, and then verified with finite element analysis (FEA). Modeling was done in SolidWorks and analysis was done with COSMOS/M, supplied by Dassault Systèmes subsidiary Structural Research and Analysis Corp. The manufacturers opted for a layup strategy that combined alternating placement of prepreg carbon fiber/epoxy unidirectional fabrics in the axial direction, with wet winding of carbon fiber/epoxy in the hoop direction, for a total of 480 plies. Initial design work indicated that the hull, to be rated for 4,000m depth with a 2.25 safety factor, should be 114 mm thick or 4.5 inches, which OceanGate opted to round up to 5 inches (127 mm) to build in an additional safety margin.

After layup and winding was complete, the cylinder was bagged with cellowrap and then cured in an oven at 137°C for 7 days. Afterwards, the cylinder was being prepared for machining to cut it to length, square up the ends and bond it to the titanium end caps.

OceanGate designed and applied on the "Titan" a Real Time Hull Health Monitoring (RTM) system. Utilizing co-located acoustic sensors and strain gauges throughout the pressure boundary, the RTM system makes it possible to analyze the effects of changing pressure on the vessel as the submersible dives deeper, and accurately assess the integrity of the structure. This onboard health analysis monitoring system provides early warning detection for the pilot with enough time to arrest the descent and safely return to surface.

Its first mission, in May 2018 in the North Atlantic, was a descent to the wreckage of the *Titanic*, which sits 3,688m under the surface.
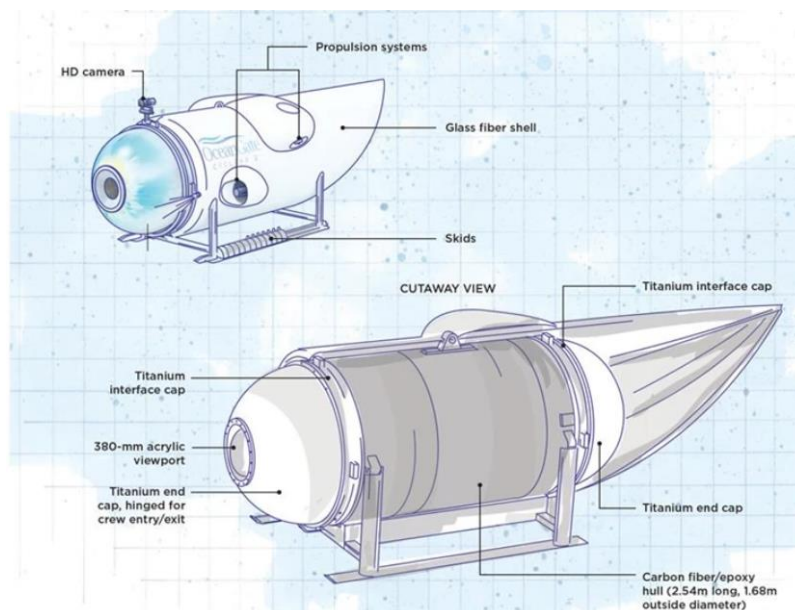
Figure 1.3 Sketch of Titan, the OceanGate 4,000m submersible

According to Davies, 2016 composites are also used in the structure of unmanned underwater drones and autonomous underwater vehicles (AUVs). Carbon fiber reinforced composites are used to improve the hydrodynamics of the fairing structure. A more recent application is the pressure resistant housing of profilers, oceanographic instruments which are deployed within the international ARGO project (Figure 1.4). Approximately 4000 robotic instruments, participating in the project, descend to a given depth and then make measurements of seawater properties (salinity, temperature) while following the ocean currents. They rise to the surface periodically to send the data via satellite, and then re-descend. The name Argo was chosen because the array of floats works in partnership with the Jason earth observing satellites that measure the shape of the ocean surface (https://argo.ucsd.edu/).

Figure 1.4 Oceanographic instrument protection casings (a) Glass/epoxy filament wound housings (500mm long, 150mm inner diameter) (b) Deep Arvor profiler engaged in ARGO project (1000mm long, 100mm inner diameter) (Davies, 2016)

1.1.2 The manufacturing process of filament winding

For many of the applications, mentioned in the previous section, the principal manufacturing technique today is filament winding (FW), which enables composite cylindrical tubes to be manufactured.

In this method, the fiber strands/filaments are wound continuously on a supportive shape form or mandrel. This method can create items in the form of cylinders and tubing, for example, high-pressure containers, tubes, and shafts. FW is an inexpensive and automated method for placing fibers in a precise pattern that adapts to the path of stress by allowing the efficient use of high-strength fibers for enhanced structural efficiency. In other words, the anisotropic fiber properties are optimized. In addition, mass production can cut down the cost further.

Figure 1.5 shows a sketch of the FW method. A stationary rotating mandrel is used in the FW process, while a carriage arm moves horizontally with the mandrel. The arm contains a guide or delivery eye which groups and dispenses pre-impregnated fibers called rovings; rovings are usually carbon, Kevlar™, glass fiber, or a hybrid (Azeem et al., 2022). As the mandrel turns, the rovings wrap around it to form a composite winding over the mandrel's surface. The composite winding's exact direction is determined by the carriage rate and the mandrel's rotary velocity. The fibers are impregnated in the resin before they wrap over the mandrel and later solidify with the fiber. After the overwrapping of fiber has been finished, the entire assembly, mandrel plus composite overwrapped layers, is put in the oven to be heated at the required temperatures for curing. The mandrel is removed when the composite resin is fully cured, leaving the hollow composite structure. Nevertheless, optimization of resin type, fiber type, fiber tension, winding thickness, winding angle, and speed, etc., is needed to tailor the product's required final quality (Tsouvalis, 1998).
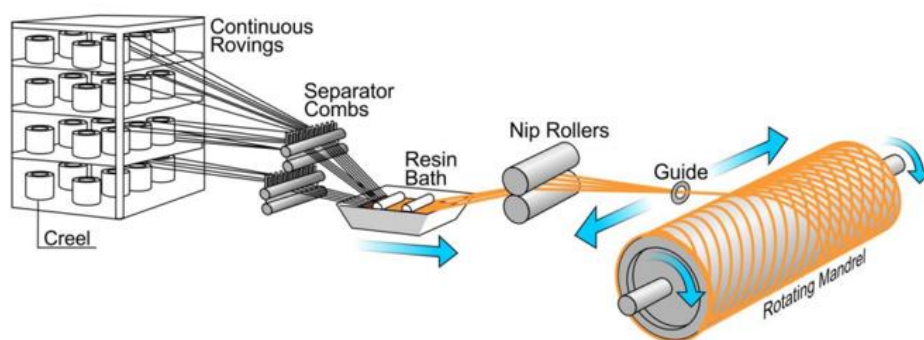
Figure 1.5 Schematics of filament winding process (Tsouvalis, 1998)

There are two typical types of winding machines: helical and polar. In the helical winding machine, which is illustrated in Figure 1.6 (a,b), the mandrel rotates continuously while the delivery eye moves back and forth. The rotational speed of the mandrel and the linear speed of the delivery eye can be programmed to produce any fiber orientation between 5° and 85°, since filament winding of 0° axial plies or 90° circumferential plies on a tubular structure are not practical in terms of manufacturing feasibility (Peters, 2011; Azeem et al., 2022). Several back-and-forth travels of the carriage are needed to complete a lamina covering the mandrel.

Such a lamina is always a two-ply balanced laminate at ±θ. In polar winding, composite fibers pass tangentially to the polar position and cover the fiber along the polar path, reverse direction, and pass tangentially to the opposite polar position at the other end. In one-word, composite fibers are wound from one pole to pole, while the mandrel arm rotates around the longitudinal axis. Polar winders, like the ones shown in Figure 1.6 (c,d), are used to produce spherical vessels or cylindrical vessels with length/diameter ratio less than 2.0. A typical polar winder consists of an arm that rotates around the mandrel delivering the roving into a planar shape. The mandrel is stepped slowly that the arm covers its surface. Except for the perfect sphere, the planar path always has a slip angle with respect to the geodesic path that limits the applicability of polar winding to nearly spherical shapes. An unusual type of winding machine is illustrated in Figure 1.6 (e). It is a high-speed robotic filament winding machine designed to produce complex, non-linear – or curved – parts in varying cross sections and with a high degree of precision.

The major limitations of filament winding are size restrictions, geometric possibilities, the orientation of fibers, the surface finish of the final product and residual stresses after curing process. Void content may be high since no vacuum or autoclave is used and the resin cures at low temperature.

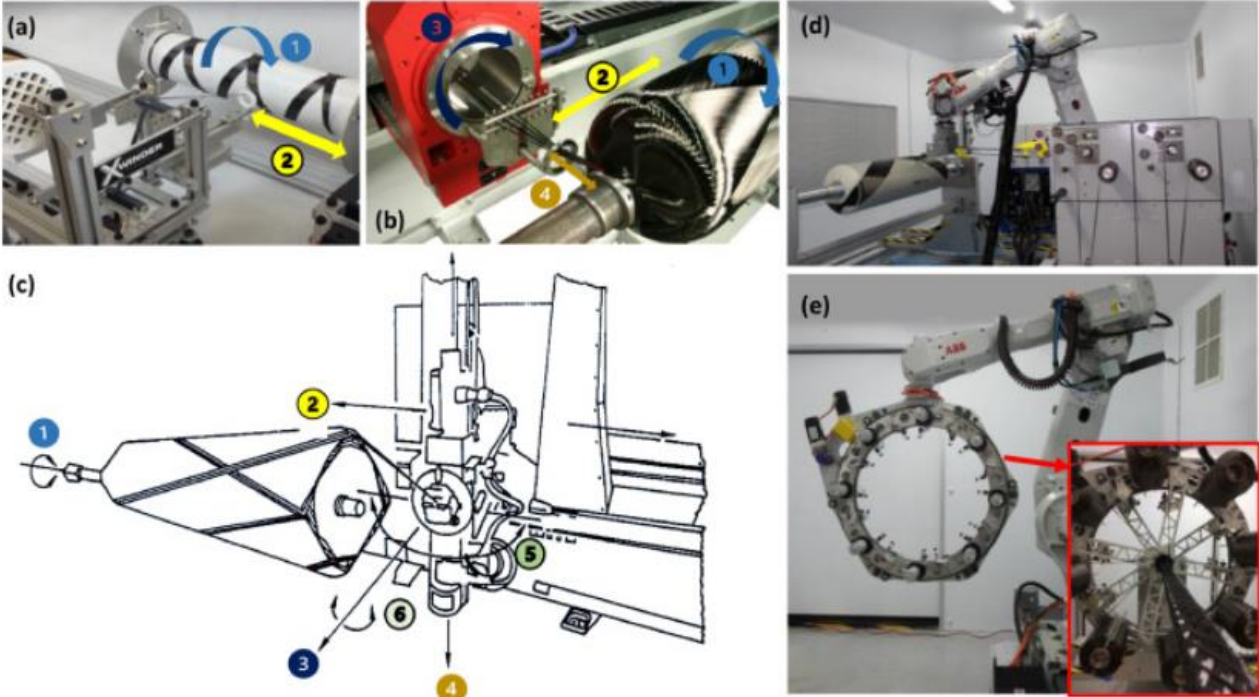

Figure 1.6 (a) 2-axes winder (Source: Xwinder), (b) 4-axes module (Source: MICROSAM), (c) 6-axes winder (Source: McClean Anderson), (d) Robotic winder (Source: Cygnet Texkimp), (e) 3D winder with multiple payout eyes (Source: Cygnet Texkimp)

1.1.3 Composite pressure vessels

High-pressure vessels represent one of the largest and fastest-growing markets for advanced composites, particularly for filament-wound carbon fiber composites. Although they are used in self-contained breathing apparatuses and provide oxygen and gas storage on aerospace vehicles, the primary end markets are for storage of liquid propane gas (LPG), compressed natural gas (CNG), renewable natural gas (RNG) and hydrogen gas (H_2) in passenger cars, buses, trucks, and other vehicles or for bulk transportation. While LPG tanks can be used in vehicles, there is also a growing market for cooking and heating in developing countries. Pressure vessels are considered as important equipment in petroleum and chemical industries especially as storages for oil and chemical components. Their functions are extended, also, from heat exchangers and boilers to underwater vessels. Conventional pressure vessels constitute cylindrical drums with end domes, since the cylindrical construction eliminates the stress concentrations in the sharp-cornered structure.

They are organized in five types, visualized in Figure 1.7: all-metal construction (Type I), metal with some fiber overwrap in the hoop direction, mostly steel or aluminum with a glass fiber composite (Type II), metal liner wholly overwrapped in a fiber resin system, including the domes (Type III), polymeric liner fully wrapped with a fiber-resin system (typically carbon fiber or hybrid carbon/glass fibers); plastic liner also serves as a mandrel for the FW operation (Type IV) and linerless, all-composite construction (Type V). A comparison among the principal characteristics of the distinct types of pressure vessels is presented in Table 1.1.
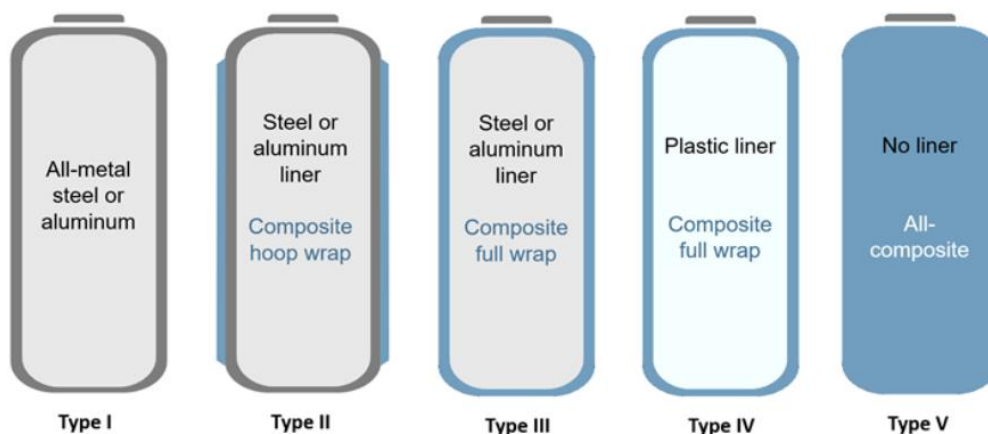

Figure 1.7 Pressure vessel types

Table 1.1 Comparison of various pressure vessels (Azeem et al., 2022)

Vessel Type	Built features and; *Pressure limits*	Weight (Kg/Liter)*Comparison*	Cost/Liter and; *Comparison*	Liner material;*Load bearing*	Composite layers load sharing
Type 1	Full metal; *Limited to 500 bars*	0.80 - 1.4 *(Heaviest)*	$3 - $5 /liter	Aluminium or steel (or their alloys) *100% load bearing*	—
Type 2	Composite hoop wrapped on metallic liner; *No pressure limit*	0.50 - 0.68 *(15 to 35% lighter than type 1)*	$5 - $7/liter *(50% costly than type 1)*	Aluminium or steel (or their alloys) *55% load bearing*	45% load bearing
Type 3	Composite hoop and helically wrapped on metallic liner; *Pressure upto 450 bar (cyclic) and upto 700 bar (static)*	0.41 - 0.45 *(44% - 48% lighter than type 1)*	$9 - $14/liter (twice of type 2)	Aluminium or steel (or their alloys) *20% load bearing*	80% load bearing
Type 4	Composite hoop and helically wrapped on polymeric liner; *Up to 1000 bar*	0.25 - 0.39 *(70% - 75% lighter than type 1)*	$11 - $18/liter (3.5 times of type 1)	HDPE, Polyamide; *0% load bearing*	100% load bearing
Type 5	Composite hoop and helical composite layers	10 - 20% lighter than type 4	—	Linerless	100% load bearing

Usually, the inner pressure is higher than the external pressure. However, pressure vessels, subjected to higher external pressure, often appear in the form of submarine pressure hulls, offshore drilling rigs and immersed tubes. The use of composites for pressure hulls of underwater vehicles and submarines has been an ongoing research topic for many years. According to Moon et al., 2010, for an underwater vehicle operated in deep sea, hydrostatic pressure–induced buckling tends to dominate structural performance. Therefore, a cylindrical structure generally experiences unstable buckling which leads to a decrease of the load-carrying capacity of the structure. Furthermore, the larger the structural weight, the more buoyancy is required. A solution to the challenging design of submersible pressure vessels seems to be the use of composite materials for underwater vehicles. On the one hand, these materials enable the efficient use of high-strength fibers, aiming to higher buckling resistance. On the other hand, they contribute to the reduction of their total weight and expand the depth of operation because the less weight can allow for greater structural reinforcement.

Depending on the type of application of the pressure vessel, there is a variety of shapes of the vessel heads that can be used. Commonly used pressure vessels are constructed either as a uniform structure, including the ends, or as cylinders closed by ellipsoidal or hemispherical heads. The applications of such heads provide the minimum stress concentration as the transition from cylinder to the cap is curved, avoiding sharp edges. The curvilinear shapes are

much more frequently used in the case of vessels with bigger diameter values and rather thin-walled vessels. In certain situations (i.e., small internal diameters), flat endplates can be more useful, which are less complex in shape and much cheaper in fabrication. The procedure of spinning and pressing of the curvilinear tank heads demands the application of the cost generating molds or technologies, which becomes effective only in the case of mass production. When the tubes are subjected to high pressures, the calculated wall thickness becomes big, and the use of flat ends is also more rational and justified, due to their relatively simple form (Romanowicz & Szybiński, 2021).

The area of the greatest interest, due to the development of exceedingly high stresses, is the joint between flat ends closures and the cylinder.

1.2 Structural adhesive joining

1.2.1 A brief introduction to adhesive joining

A variety of methods can be used to join materials. The principal joining techniques were by purely mechanical fastening or by welding and soldering in the case of metallic components, up until the introduction of the polymeric adhesives around the time of the Second World War. Since that time, advances and improvements have been made in adhesive bonding technology. The aerospace field was the first sector that promoted the use of adhesives in the aircraft manufacturing process; hence, the growth of the aircraft and aerospace industries has influenced adhesive technology in a great extent. Figure 1.8 illustrates a schematic of Boeing 787 which holds approximately 50% bonded composite structure.
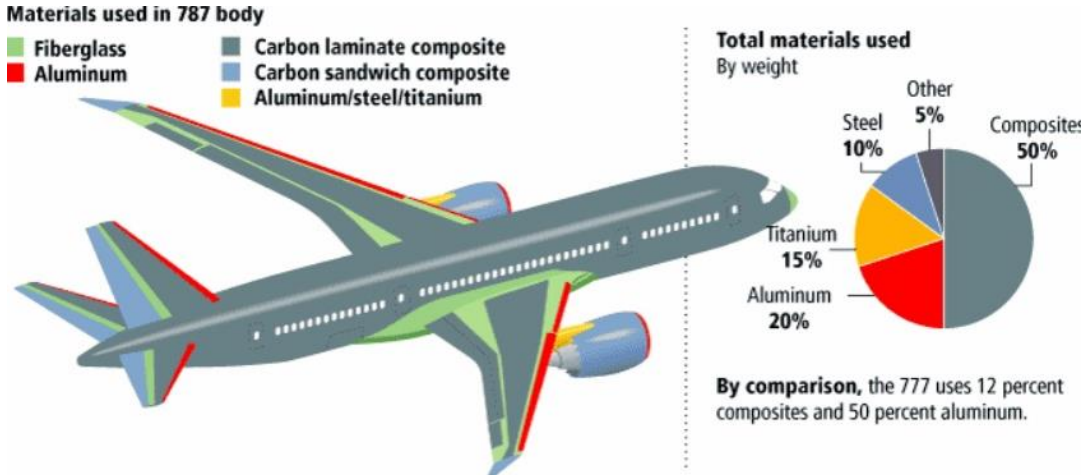
Figure 1.8 Adhesive bonding applications in the Boeing 787 (Yudhanto et al., 2011)

In recent years, a wide range of industrial fields rely on structural bonding and adhesively bonded assemblies for several reasons, such as their contribution in building lighter and therefore more energy-saving structures. Furthermore, this technique allows for multi-materials assembling, and features fairly good stress distribution properties. Among these fields, one may mention aeronautics, marine systems or automotive, each one being extremely careful regarding the mechanical strength of their structures. In particular, the naval engineering sector started using adhesive bonding in the 1980s. Since then, it has been a field of study for

various scientists, with deck-to-hull and bulkhead-to-hull joints receiving the most attention. For instance, deck-to-hull bonding requirement of high Young modulus combined with high-bond-thickness to compensate for large production tolerances, is met due to an appropriate adhesive joining solution as shown in Figure 1.9. Moreover, superstructures, bulkheads, masts, and even the entire deck can be replaced with composite materials that have been appropriately produced and adherently attached to metal or composite elements. Adhesive bonding is becoming increasingly appealing to automotive manufacturers as well. In the promising field of electric motors, magnet bonding solutions enable the efficient assembly of magnets in electric motors without the necessity of mechanical fixation. In the case of mini cameras, embedded in modern vehicles, their tiny size makes it impossible for them to be bolted into place. Instead, special adhesives adapted to the respective materials are used to bond the plastic housings and fix the lenses.
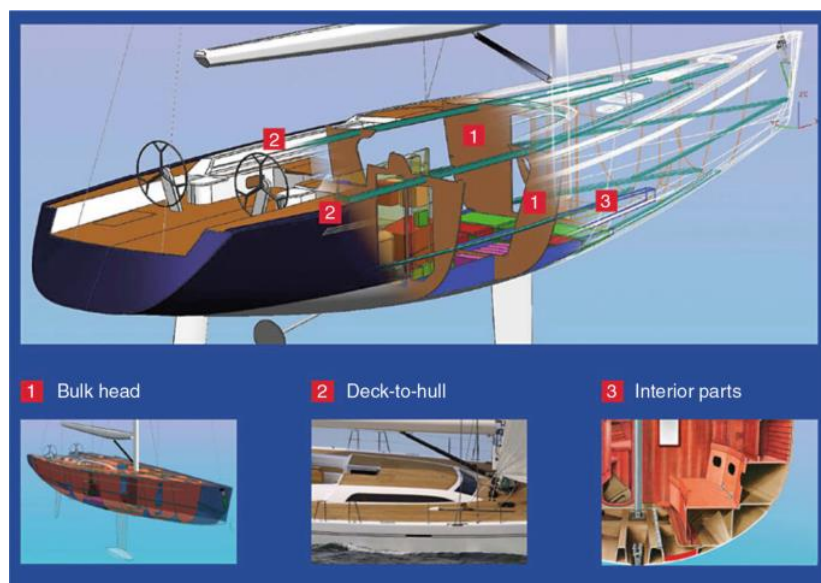
Figure 1.9 Bulkhead-to-hull, deck-to-hull, and interior part joint examples
(Handbook of Adhesion Technology, 2019)

The reason for the increased use of adhesive joining is that it provides structural and financial advantages over the more traditional methods of joining, assuming that the joint is properly designed. Among these advantages are their high strength to weight ratio and their lower fabrication expenses according to Banea and da Silva, 2009. Additionally, adhesive bonding offers the possibility to join completely dissimilar materials, enabling the designer to choose the proper material for each part of the structure. Other important contributing factors are the electrical and thermal insulation properties and the superior fatigue resistance. According to Anyfantis, 2012 the fatigue life of adhesively bonded assemblies has shown twenty times better than riveted structures of identical components. Adhesive joints also provide galvanic isolation, a fact that reduces corrosion when joining different metals. The improved hydrodynamic/ aerodynamic surface design and the visual appearance consist other reasons why adhesive joining is so desirable from industry. In terms of structural perspective, a critical factor is the better load carrying capability adhesively bonded joints offer, since the stresses are distributed more evenly. The application of these joints, especially in structural components made of fiber-reinforced composites, prevents from local damage of fibers and

introduction of stress concentrations, traditionally caused by the fastener holes (da Silva et al., 2011).

Focusing on the naval applications, a few more advantages can be mentioned when choosing adhesive bonding. The hot work of welding is avoided, reducing the risk of fire. In the case of maintenance work, it can be done on the spot with no need of dry-docking of the ship. Additionally, the sealing of the cracks made by adhesive joining is water-tight and offers the flexibility to be performed even on complex geometries. This type of repair can fit into spaces where conventional welding would not easily reach. Because of the low weight of materials used, their transportation and application are easy without demand of heavy lifting machinery (Andrianakis, 2011).

As with any other technology, there are also limitations to consider when using adhesives in engineering. Some of them have been mentioned by Fredrik Fors, 2010 and Stratakis, 2017. The strength of some types of adhesives is negatively impacted by elevated temperatures and high humidity, especially under continuous stress. As with other polymeric materials, creep effects must be considered. Moreover, the adhesive bond requires additional equipment and fixtures in order to immobilize and set the structure in the proper position during the bonding process. To guarantee good quality bond, surface preparation and thorough cleaning are critical.

1.2.2 Adhesive joint geometries/ configurations

The cross-sectional shape of the joint is one of the first issues that comes up while designing an adhesively bonded structure. The strength of a given type of joint depends, for a given type of load, on the stress distribution within the joint, which in turn depends on the joint geometry and the mechanical properties of adhesive and adherend. Figure 1.10 shows the most commonly used engineering adhesive joints. In the case of FRP composite substrates, the high through-thickness stresses at the overlap ends are of particular concern, due to the relatively low through-thickness strength of most composite materials. This often means that joints made with high strength adhesives are more likely to fail prematurely in the composite before failure in the adhesive occurs (Banea and da Silva, 2009).

Figure 1.10 Typical adhesive bonded joints configurations
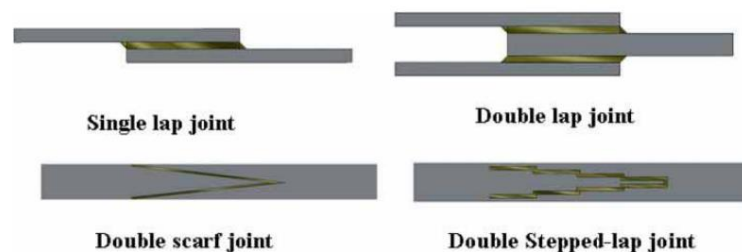
According to the overview in adhesively bonded joints of Banea & da Silva, 2009, one of the simplest types of joint, the single-lap joint (SLJ), is due to the easy fabrication process commonly occurring and frequently used for test specimens. The load bearing capabilities are however limited by peel stresses induced by a bending moment resulting from the pulling forces

11

not being collinear. Another concern associated to this joint is the fact that the stress distribution (shear and peel) is concentrated at the ends of the overlap.

Following the comparison among different adhesively bonded joint types in experimental and numerical way, Barbosa et al. (2018) suggest that double-lap joints (DLJ) are also simple to fabricate but there is a need to have access to both sides of the structures to perform these joints. In fact, the efficiency of this joint is much higher than that of the SLJ because of duplicating the shear-resistant area for the same overlap length. Banea and da Silva (2009), add that the peel stresses can be severely reduced thanks to the symmetry about its longitudinal centerline of a DLJ but even with the peel reduced to manageable levels, the stress state in the adhesive is complicated and not easily determined. Tsouvalis & Karatzas (2010) proposed an adhesive joint configuration based on a butt - double lap geometry subjected to tensile tests. This simple concept composite-to-metal joint can be simply and easily manufactured using even conventional manufacturing methods of composite materials. The authors have showed that their proposed joint yields comparable strengths to those attained from the double strap steel-to-composite joints and superior to the strength of other novel concept steel-to-composite joints, either with CFRP or with GFRP.

Two other joint types which have an improved overall performance for the same bonded area are scarf joints and the stepped-lap joints. However, the components to be bonded need milling operations, which makes the joints more demanding to fabricate and less desirable in the case of prone to local damage materials, such as FRP. Hart-Smith (1973) conducted a pioneering study of the development of scarf joints and lap-stepped joints between metal and composite adherents for astronautic and aeronautic applications. Since Hart-Smith (1973), several researchers have been focused on stepped-lap butt joints and scarf joints between similar and dissimilar adherents. According to the study of Barbosa et al. (2018), the scarf joint, particularly, provides the smoothest peel stress distribution along the bond length, especially for large overlap length values, which is due to the highly advantageous tapering effect of the adherents and corresponding adherent stiffness reduction at the scarf tips. Gacoin et al (2009) conducted a further investigation on the damage evolution of the adhesively bonded scarf and double scarf joint of adherends made of mild steel, concluding that in either case the behavior of the adhesively bonded joint is better when the scarf angle is lower than a=18°, as it is shown in Figure 1.11.

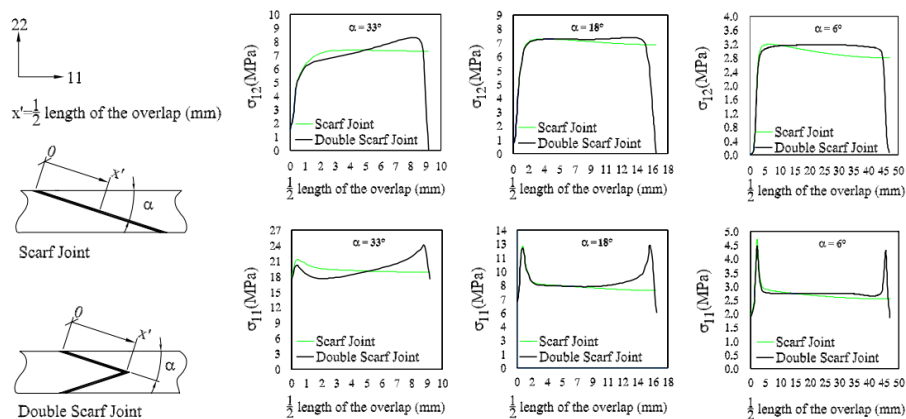Fig. 8. Distribution of the stresses in the middle of the bonded joint for different value of the scarf angle α when $F = 3$ kN. (Up) Shear stresses σ_{12}. (Down) peel stresses σ_{11}.

Figure 1.11 Distribution of the stresses in the middle of the bonded joint for different value of the scarf angle a (Up) Shear stresses σ12. (Down) Peel stresses σ11. (Gacoin et al, 2009)

Regarding the stepped-lap joints, a state-of-the-art study, examining the effect of steps on the load bearing capacity of 3D-printed single lap joints numerically and experimentally as well, concludes that the addition of steps in overlap area can increase fracture load and improve structural integrity of the single lap joint. Mohammad Reza Khosravani et al (2023) mentions that the application of steps with equal lengths is the most preferable.

1.2.3 Analysis of adhesively bonded joints

Analytical methods

The most important functional characteristic of a joint is the strength, since its contribution toward stiffness is typically small. Complex adhesive bonding cases and applications for composite materials have highlighted the importance of accurate stress and strain calculations and, hence, the conditions that may result in failure (Adams & Comyn, 2000). In fact, adhesive joints are demanding in terms of design, especially in composite structures, since they entail discontinuities in the geometry of the structure and/or material properties and introduce high local stress concentrations which can lead to failure.

Theoretical prediction of joint failure is most commonly achieved by calculation of adhesive stresses, followed by the application of suitable failure criteria. An assumption which simplifies the problem is that the failure occurs within the adhesive, rather than at the interface between adherend and adhesive. Whilst experience has shown this to be the case for most well-made metallic joints, composite adherends can often fail by delamination before the adhesive failure (Adams & Comyn, 2000). Structural adhesives perform best in shear, and worst in tension or cleavage as depicted in Figure 1.12. Designs are therefore generally arranged to cause the adhesive to be loaded in shear.
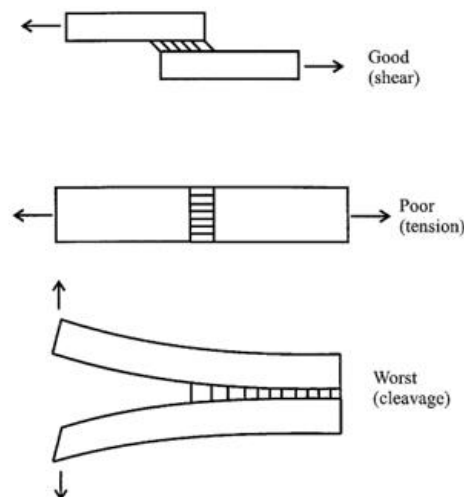
Figure 1.12 Different modes of adhesive loading (Adams & Comyn, 2000)

Much stress and strain analysis has been conducted on the simplest and the most common joints that can be found in practice, the single-lap joint (SLJ) which performs mainly in shear. The simplest analysis is based on this type of joint (Adams et al., 1997). Based on this analysis, the adhesive is considered to deform only in shear and the adherents to be rigid. The

adhesive shear stress (τ) is constant over the overlap length, as shown in Figure 1.12, and is given by τ = P/bl, where P is the applied load, b is the joint width and l is the overlap length. The value of the shear stress can be interpreted as the average shear stress acting on the adhesive layer. Volkersen (1938) improved this simple model by considering the tensile extensions in the adherends. His shear-lag equations adapted these elastic deflections in the shear deformation of the adhesive and predicted that the shear stress should peak towards the ends of the adherends, as shown in Figure 1.13. In the middle of the joint, the shear stress will be a minimum. Adherends which are unequal in stiffness will produce an asymmetric shear stress distribution. A serious drawback connected to the theory of Volkersen is that it neglects the eccentricity in the applied load which is caused by the non-symmetric geometry of single-lap joints. The eccentricity serves to introduce bending moments in the adherents, often causing significant joint rotation and adherend bending before failure. Another consequence of this rotation is that the adhesive is deformed in shear, tension, and compression. Goland and Reissner (1944) tried to take this effect into account by creating a bending moment factor, relating the moment at the adherend ends to the applied load. Figure 1.14 illustrates the joint deformation they predicted under tensile loading. It is clearly seen that the peel stresses peak at the ends of the overlap, where Volkersen also predicted that the shear stresses should peak. Nevertheless, according to da Silva et al., 2011 the work done by Volkersen (1938) and Goland and Reisner (1944) has several limitations: firstly, the variations of the adhesive stresses through the thickness direction, especially close to the interface, are not taken into account and secondly, the peak shear stress occurs at the ends of the overlap, which violates the stress-free condition, overestimates the stress at the ends of the overlap and results in conservative failure load predictions.
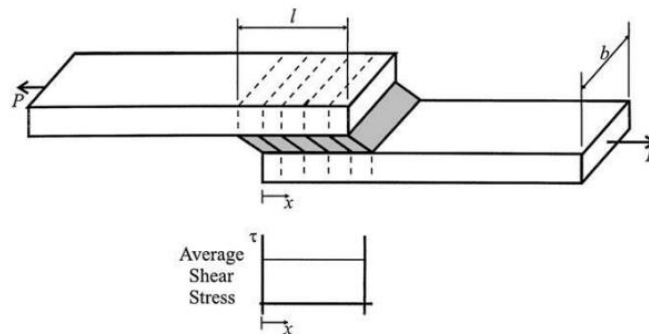
Figure 1.12 Simple rigid adherend model of single lap joint (Adams & Comyn, 2000)
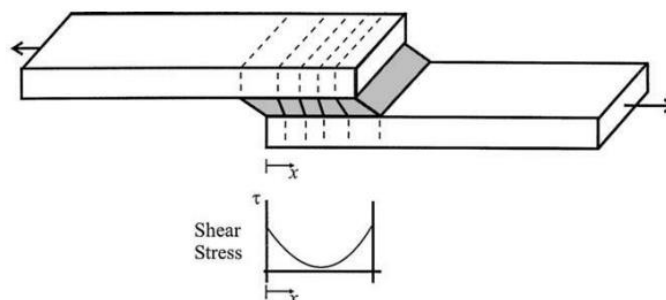
Figure 1.13 Volkersen's elastic adherend model (Adams & Comyn, 2000)
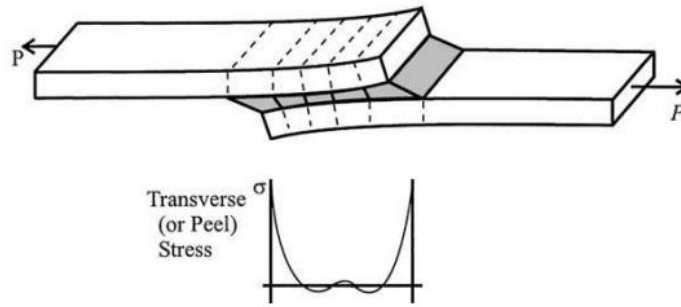
Figure 1.14 Goland and Reissner bending model (Adams & Comyn, 2000)

Ojalvo and Eidinoff (1978) used a more complete strain/displacement equation for the adhesive layer to examine the influence of adhesive thickness on the stress distribution. Since then, scientists have conducted thorough studies on the accurate strength calculation of adhesively bonded joints using analytical methods.

Numerical methods

The most common technique used in the context of adhesively bonded joints is the Finite Element Method (FEM). One of the first reasons for the use of the FE method was to assess the influence of the spew fillet. Spew fillet is the adhesive geometry at the joint's boundaries, where a portion of the adhesive bridges the adherends with a gradual inclination. It reduces the joints' stiffness discontinuity at the bonding area's edges to smooth the load transfer and reduce stress concentrations. This is proven in Figure 1.15 which shows a single lap joint (a) without and (b) with spew fillet and compares the stress distribution of these two cases along the overlap distance.
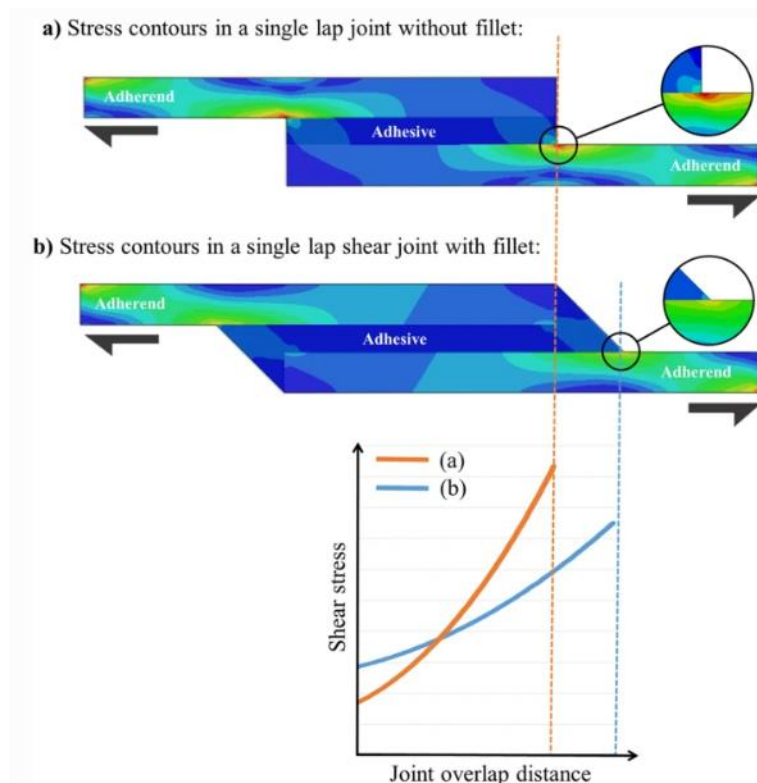
Figure 1.15 The effect of fillet presence on shear stress in a single lap joint (Omairey, S. et al., 2021)

The joint rotation and the adherents and adhesive plasticity are other fields that are easier to be analyzed with a FE analysis (Anyfantis 2012). Linear and nonlinear FE models have been conducted on distinct types of adhesive joints, and the adhesive effective stresses and strains have been evaluated. Banea & da Silva (2009) suggest that a fine mesh is necessary in areas where the adhesive layer is thin compared with the thickness of the adherends.

Adhesive bonded joints contain inherent defects from their manufacture. The crack initiation starts from these defects and leads later to failure of the assembly. The fracture strength of adhesive joints depends on several factors and their combinations, e.g., adhesive type, cure cycle, adherend type, bond line thickness etc. In order to decrease the amount of costly testing at the design stage, an accurate strength prediction of adhesively bonded joints is essential. Currently used approaches for predicting the strength of adhesively bonded joints are: the continuum mechanics approach (stress based), fracture mechanics, and damage mechanics approach.

Continuum mechanics approach

The adhesive and adherends are modelled by using continuum elements, assuming that the adhesive is perfectly bonded to the adherends. The assumption of a perfect bond means that the finite-element analysis takes no account of the adhesion properties of the interface, neither of imperfections of the material. The maximum values of stress, strain, strain energy or plastic energy density, predicted by the FE analyses, are introduced in the failure criterion, and are compared with the corresponding material allowable values.

The maximum principal stress failure criterion was proposed for very brittle materials whose failure mode is at right angles to the direction of maximum principal stress. This criterion ignores all the other principal stresses, even though they are not zero. Establishing the failure modes in lap joints bonded with brittle adhesives, Adams et al. (1997) have extensively used this criterion to predict joint strength effectively. However, it is difficult to use maximum stress or strain criteria due to the bi-material singularities inherent in a bonded joint. Since this singularity at the ends of idealized bonded joints will not be avoided easily, the maximum stress or strain for such a model will coincide with the value at the singularity and thus will be dependent on the mesh refinement.

Crocombe (1989) and Zhao (1991) used the maximum stress and strain failure criteria, but this time applied at a certain distance from the singularity. This method is connected to a criterion based on a critical stress at a critical distance away from the crack tip. Since stresses around the crack tip are most responsible for the joint failure, it is therefore proposed that failure is governed by the -averaged- stresses or strains within a critical distance from stress singular points. The critical distance may be chosen in such a way that the averaged stress or strain equates to the failure stress or strain in tensile tests.

When ductile adhesives are used, criteria based on stresses are not appropriate because joints can still endure large loads after adhesive yielding. For ductile adhesives, Adams and Harris (1984) used the maximum principal strain as failure criterion for predicting the joint strength. This criterion can also predict the failure mode. However, it is equally sensitive to the mesh size as the maximum principal stress approach.

Fracture mechanics approach

Cracks are the most common defect in structures, for which fracture mechanics has been developed. In the fracture mechanics approach, the basic concept is the energy approach to crack growth, introduced by Griffith in 1921. The central idea is the energy release rate, G, which is defined as the rate of change for the potential energy of the crack area and thus has the units of energy over area (J/m²). The energies related to the growth of a crack in a material are mainly the free surface energy needed to create new free surfaces on the sides of the propagating crack and the strain energy stored in the loaded material.

This concept has gradually gained ground in other engineering fields. Many studies dealing with adhesive joints use the strain energy release rate, G, and respective critical value or fracture toughness, G_C instead of stress intensity factors because these are not easily determinable when the crack grows at or near to an interface.

The Virtual Crack Closure Technique (VCCT) is a common fracture analysis method that is utilized for the numerical simulation of the failure behavior of adhesive joints when plastic dissipation does not exist. According to this method, the parameters of internal nodal forces and the relative displacements of the adjacent nodes are calculated at the crack tip, as depicted in Figure 1.16. These magnitudes are used for the calculation of the energy release rate (G_i, i = I, II or III where G_I, G_{II} and G_{III} are the energy release rates at Mode I, II and III fracture, as shown in the Figure 1.17), which is further compared with the experimentally measured fracture toughness (G_{ic}, i = I, II or III) of the material system. Crack propagation then occurs if the energy release rate magnitude is greater than the G_{ic} magnitude. An advantage of VCCT is its numerical simplicity and effectiveness. The method is quite accurate for calculation of the fracture energy at the crack tip, especially when homogenous materials are analyzed. However, when the crack path lies in a bi-material interface, VCCT results concerning mode partition become sensitive to the mesh size around the crack tip according to Agrawal & Karlsson, 2006. Moreover, the technique has limitations that stem from its two basic hypotheses: 1) the energy released during crack growth is identical to the energy required to close the crack, and 2) when the crack extends, the stress state does not change significantly. These hypotheses suggest that dissipation mechanics, such as plasticity, are ignored in the analysis.
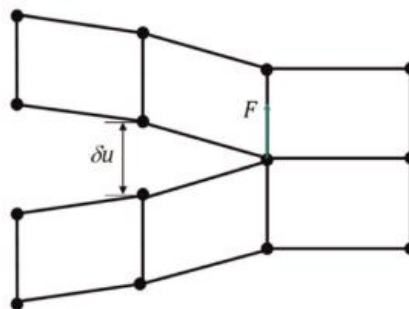

Figure 1.16 Internal node force and separation δu applied in VCCT analysis
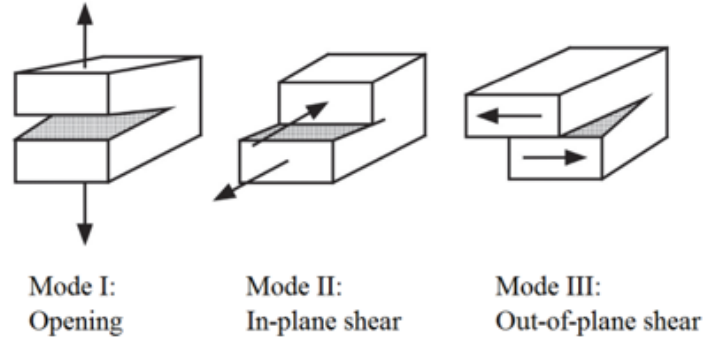
Figure 1.17 Basic loading and fracture modes of an adhesive joint

Damage mechanics approach- Cohesive Zone Model approach

Enhanced modeling techniques are required that comprise accurate failure predictions, surpassing the limitations associated to the continuum and fracture mechanics approaches, to effectively model damage evolution within a material or structure with bonded components. Damage mechanics permits the simulation of step-by-step damage and fracture at a predefined crack path or arbitrarily within a finite region up to complete structural failure.

The use of cohesive zone models (CZM's) coupled to conventional FE analyses is the most widespread method of predicting static or fatigue damage uptake in structures according to Anyfantis, 2012. Barenblatt (1959) and Dugdale (1960) proposed the CZM in 1960"s, where stresses across a potential crack path are bounded and that a traction-separation law can describe locally the fracture behavior inside the cohesive zone ahead of the crack tip. But something more was needed to relate the local cohesive zone to the global behavior. And that was done by Rice (1968) with his theory of J-integral, where large-scale plasticity and the interfacial nonlinear behavior can be considered. And the fact that the status of the energy release rate during crack initiation can be related to a status of the local traction-separation law made the connection between local and global behavior.

A general explanation is that the stress along the crack faces of the fracture process zone and the corresponding separations can be described by a traction-separation law in Mode I, II and III loading (Figure 1.17) and fracture. In particular, the local normal stress σ_n and the local shear stress σ_s inside the process zone are dependent on the local normal crack opening δ_n and tangential sliding δ_s. This can be written as: $\sigma_n = \sigma_n (\delta_n, \delta_s)$ and $\sigma_s = \sigma_s (\delta_n, \delta_s)$. According to Sørensen and Kirkegaard (2006) the evaluation of the path-independent J-integral along a path around the fracture process zone yields:

$$J = \int_0^{\delta_n^*} \sigma_n(\delta_n, \delta_s)d\delta_n + \int_0^{\delta_s^*} \sigma_s(\delta_n, \delta_s)d\delta_s \qquad (1.1)$$

where δ_n^* and δs^*defined as the normal opening and tangential sliding displacement at the precrack tip.

The importance of cohesive laws is that they can be introduced in Finite Element models and predict the failure of adhesive joints. So far, many models have been used in the literature

18

assuming an idealized shape and function of the cohesive law. The most commonly used are of the following shapes: bilinear, exponential, and trapezoidal, presented in Figure 1.18.
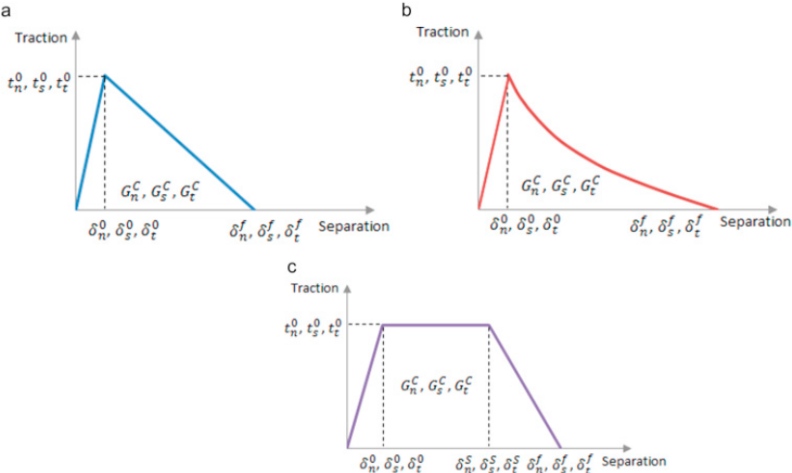
Figure 1.18 Damage evolution laws considered (a) bilinear, (b) exponential and (c) trapezoidal

Cohesive zone elements can be introduced in Finite Element codes and simulate quite well crack initiation and propagation. The CZM laws are established between paired nodes of cohesive elements, and they can be used to connect superimposed nodes of elements representing different materials or different plies in composites, to simulate a zero thickness interface (local approach; Figure 1.19a), or they can be applied directly between two non-contacting materials to simulate a thin strip of finite thickness between them, e.g. to simulate an adhesive bond (continuum approach; Figure 1.19b) as mentioned in the PhD Thesis of Anyfantis, 2012.
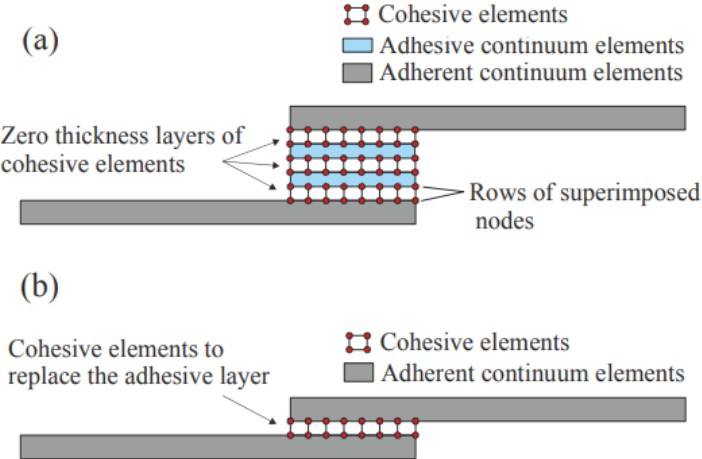
Figure 1.19 Cohesive elements simulating (a) interfacial failure between materials and (b) failure along the adhesive bond (Anyfantis, 2012)

Experimental methods measuring cohesive laws

For the cohesive laws to be implemented in the Finite Element models, their parameters are needed to be measured first. Various experimental testing methods have been used to measure these parameters, depending on the mode type of cohesive law that needs to be measured. The parameters that are measured usually during the experiments are the fracture toughness denoted as G_C or J_C, the maximum stress σ_{max} and the maximum opening displacement δ_{max}. Next are presented experiment set-ups used to measure cohesive laws.

- Mode I

Sørensen and Jacobsen (2003) determined the cohesive laws by a J-integral approach by using a Double Cantilever Beam (DCB) specimen (Figure 1.20 (a)). The end-opening displacement was measured with extensometers at the neutral axis on the beam at the initial crack tip. A meaningful cohesive law was obtained by differentiating the J-integral (determined from the load) with respect to the end-opening displacement. Ji et al. (2010) measured the Mode I cohesive laws of a bonded DCB joint, trying to provide data for the parameter calibrations in numerical models and to investigate the relation between adhesive thickness and interface toughness.

Ouyang Zh. et al. (2011) used the same test configuration to obtain pure Mode-I cohesive laws but using dissimilar adherends (Figure 1.20 (b)). According to their paper, the energy release rate was calculated and then the cohesive law was also obtained by differentiation. However, the problem they had to solve was how to achieve pure Mode-I loading in the dissimilar DCB specimen and avoid as much as possible the presence of shear stresses that will appear due to the asymmetry of the geometry. What they proposed is a decoupling condition under which the shear stresses vanish. After giving a theoretical demonstration of the feasibility of the idea, a comparison between numerical and experimental results was presented in order to evaluate the proposed method. The decoupling condition proposed is written as: $\frac{h1}{h2} = \frac{D1}{D2}$ where h1 and h2 are the beam thicknesses and D1 and D2 are the bending stiffness per unit width under plane strain conditions of material of beam 1 and 2, respectively.
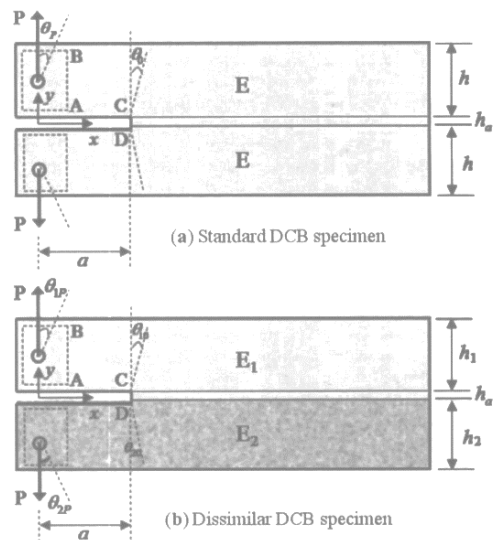
Figure 1.20 (a) Standard DCB specimen and (b) dissimilar DCB specimen

- Mode II

To measure the Mode II cohesive laws different experiment set-ups have been used with the most common being the End-Notched Flexure (ENF). This set-up was used from the scientific community for quantifying energy release rate G_{II} for metallic and laminated polymer composite adherends and investigating the shear behavior of adhesive layers. The beam is simply supported with a displacement-controlled point load of magnitude P applied at the midpoint of the top face. The geometry of the specimen is presented in Figure 1.21.
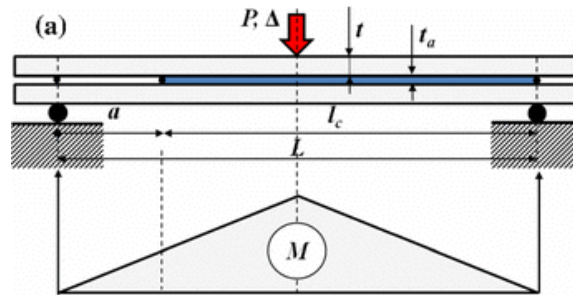
Figure 1.21 End Notched Flexure set up

Another experimental set-up, called End Loaded Split (ELS) is also used in literature for the determination of Mode II fracture toughness which then can lead to the calculation of the Mode II cohesive law. The ELS method employs a specimen similar to the DCB specimen, which is held at one end in the support fixture and loaded through an end block bonded to the other end. The support fixture is large, weighing approximately 25 kg to prevent vertical movement of the fixture. The fixture has been designed to slide on a linear bearing trolley so that load point is kept fixed. The ELS method is used for measuring the stable crack growth resistance of bonded joints and composites under Mode II loading; however test fixture costs are high in comparison with the ENF test. The experiment set-up is seen in Figure 1.22.
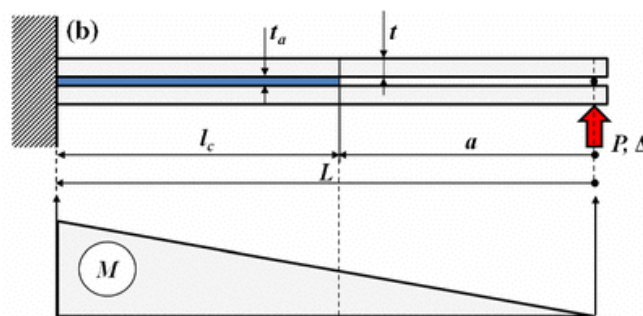
Figure 1.22 End Loaded Split set up

A drawback concerning Mode II tests where a transverse force is transmitted between the crack faces is the possible friction between the two separating faces. The friction coefficient can reach high values, increasing the toughness of the interface and thus making it difficult to calculate its contribution to the total fracture toughness.

- Mixed mode

In-service structures are commonly subjected to a combination of peeling and shear stresses. This means that a combination of modes I and II loadings occur at the crack tip. A variety of mixed-mode fracture test methods has been developed for the measurement of mixed mode cohesive laws parameters.

One of the most used experiment set-ups is the Mixed Mode Bending (MMB) introduced by Reeder and Crews providing an easy variation of the mode ratio by just altering the lever length of the loading lever c (see Figure 1.23). This set-up is used in in order to test Maritime pine wood (Andrianakis, 2011). The MMB test stands out for its easy implementation, reliability, and capability of testing a wide range of mode-mixities with only one specimen geometry. It can be considered as a superposition of the DCB and the ENF tests mentioned before. The MMB test concerning metal bonded joints presented a difficulty due to extensive adherend yielding.
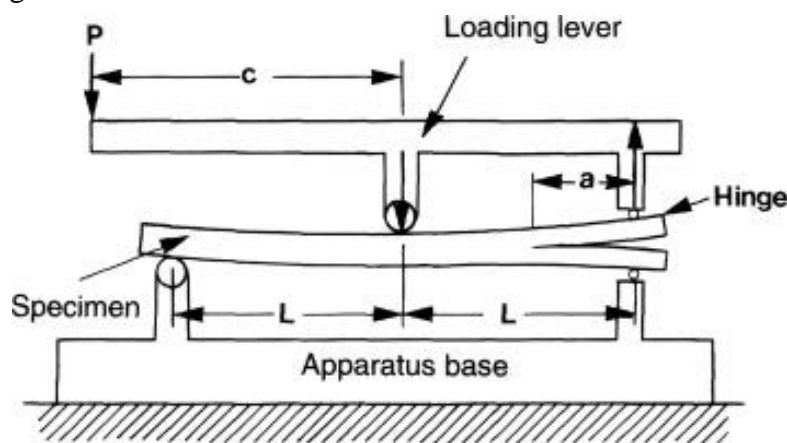
Figure 1.23 Mixed Mode Bending set up

A very promising experimental test for measuring pure and mixed mode cohesive laws is the Double Cantilever Beam with Uneven Bending Moments (DCB-UBM) introduced by Sørensen & Kirkegaard, 2006. In this study, the principle of creating different bending moments in the two free beams of the DCB-UBM specimen is shown schematically in Figure 2.24. Forces of identical magnitude, P_1 and P_2, are applied perpendicular to two transverse arms connected to the end of the beams of the DCB specimen. The un-cracked end of the specimen is restricted from rotation but can move freely in the axial-direction. Different moments are obtained if the length of the two moment arms, l_1 and l_2, of the transverse arms are uneven ($M_1 = P_1*l_1$ and $M_2 = P_2*l_2$). This test configuration presents numerous advantages, as Andrianakis (2011) highlights. Firstly, there is no need to measure the crack propagation since the energy release rate can be calculated analytically. Moreover, the specimen loading with pure moments and no transverse forces transmitted, disappears any friction between the opening faces. An additional advantage is the utility of the specimen geometry for all the range of mode mixities, so that there are no inaccuracies associated with differences in the process.
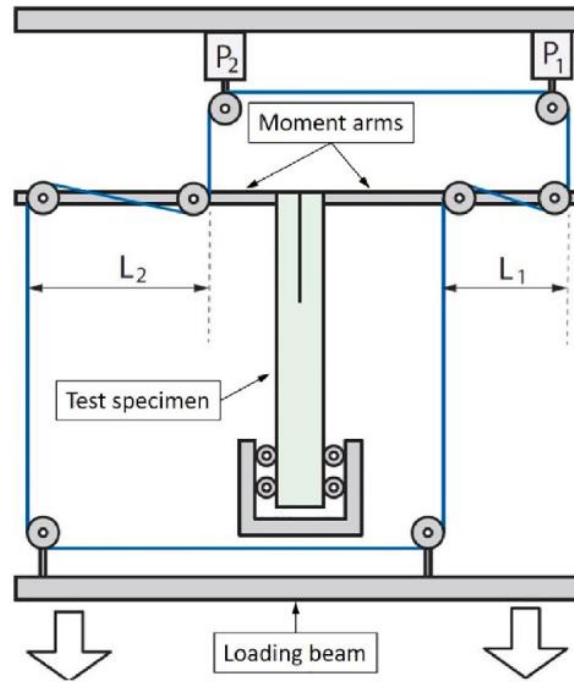
Figure 1.24 Double Cantilever Beam with Uneven Bending Moments set up

MMB and DCB-UBM specimen and experimental fixture are unable to fit in the oven used often to perform the tests under temperature, due to their large dimensions. Another test configuration, the modified Arcan test, is more compact and efficient in examining the fracture properties under mode I, mode II and mixed-mode loadings for a variety of materials such as adhesive, composite, and metallic adherents. It employs special loading fixture, in which by altering the loading angle a full range mode mixity loading is achieved. The experiment set-up and the geometry of the specimen used is shown in Figure 1.25.
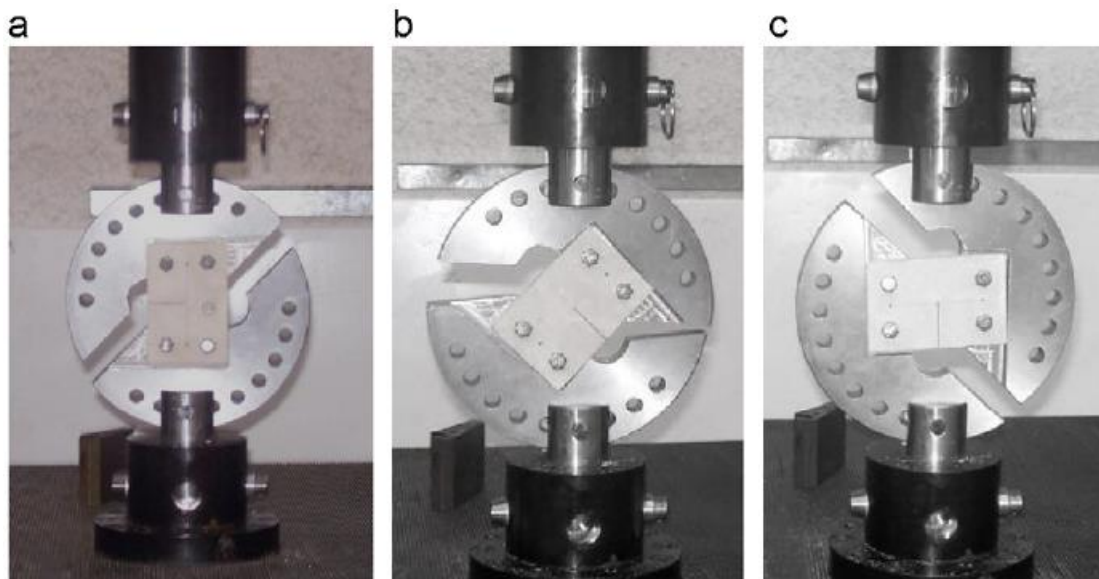
Figure 1.25 Modified Arcan test fixture and specimen
(a) mode-I, (b) mixed-mode and (c) mode-II loading.

1.2.4 Common adhesives and joining processes

Common adhesives

Based on the definition provided by Adams et al., 1997 an adhesive is a polymeric substance that is applied to substrates surfaces to join them and hinder separation. In order to select proper structural adhesive to achieve the highest strength and durability, a range of factors must be considered such as chemical compatibility between adhesive and adherends, fabrication requirements (i.e., surface treatment and hardening process), and service circumstances (i.e., loading and environmental conditions). Generally, structural adhesives are divided into four general categories as provided in Table 1.2. To adhesively bond composites to metals it is necessary to use an adhesive that is compatible with the two distinct materials being joined. Based on a literature review, it can be seen that for bonding CFRP (which have an epoxy matrix) to titanium or aluminum; toughened-epoxies adhesives are suitable (Papanicolaou et al., 2015; Seong et al., 2008).

Table 1.2 Characteristics and properties of typical adhesives
(Banea & da Silva, 2009; Delzendehrooy et al., 2022)

Adhesive	Benefits	Challenges	Service temperature (°C)	Cure	Marine application
Epoxy	The capability of adding additives to increase its strength, fire resistance, and toughness. Generation of strongest bonds. Good durability. Become soften but not melt on heating. Fill small gaps well with little shrinkage	Require vigorous surface preparation	-40 to +100 (180°C)	One-part epoxies cure with temperature. Two-part epoxies cure at room temperature	Construction of bulkheads, deck cleats, rub rails, gunwales. Cargo tanks
Acrylics	Fast polymerization. Good gap filling properties. Tolerates of contamination and less prepared surfaces. Offer flexible bonds providing good peel and impact resistance. Providing energy-absorbing bond line. Resistance to UV, moisture, and general outdoor conditions	Lower strength in comparison with epoxies. Flammable in the uncured state	-40 to +120	Cure through a free radical mechanism	Bonding topside and superstructures

Methacrylate	Provide a unique balance of high tensile, shear, and peel strengths Maximum resistance to shock, stress, and impact across a wide temperature range Remain strong and durable under severe environmental conditions Resistance against water and solvents Resistance against water and solvents Time and costsaving Excellent fatigue life	Lower strength in comparison with epoxies Slightly expensive compared with epoxies Fast cure rate which limits the perfect positioning	-40 to +80	Fast cure (minutes) upon expose to moisture at room temperature	Bonding of the hull to the deck Bonding of the bulkheads to the side shell of the hull Bonding stringers to FRP hull
Polyurethane	Good gap filling properties High degree of adhesion to composites A great deal of flexibility and impact resistance Resistant to seawater	Low strength Low modulus adhesives Require a primer to bond to metal structures	-200 to +80	Room temperature	Manufacturing multilayered panels Hull-to-deck joints

Joining process

The typical manufacturing process of adhesively bonded joints consists of six main phases including; adhesive and adherend selection, surface pretreatment, coating of the primer, application of adhesive on surfaces, assembly and pressing the joint in a mould or use grips to conduct the hardening process, and eventually, adhesive hardening (Delzendehrooy et al., 2022).

To achieve a good bond, it is necessary to start with a good adhesive. Banea & da Silva (2009) mention that the selection of the appropriate adhesive is not simple because of the broad range of available options. Before an adhesive can be specified for an application, screening tests should be conducted to compare and evaluate the various adhesion parameters. Properties of adhesives can vary greatly, and an appropriate selection is essential for a proper joint design. The main approaches for determining the properties of adhesives are two: the measure of the properties of bulk adhesive specimens and the use of standard designed joint geometries with a thin bond line (often referred to as 'in situ' testing).

Another critical stage of adhesive joint manufacturing is the substrates' surface pretreatment to ensure a strong bond that in the end will result in a cohesive failure. In most of the cases, this operation consists of cleaning the specimens using grit blasting and then applying a degreaser. By increasing the surface roughness to an optimum value, and consequently enhancement of mechanical interlocking, surface pre-treatment causes maximum strength, fatigue life, and durability. In order to select the most suitable method of surface pretreatment, the properties and type of the adhesive and adherend must be investigated by designers. For instance, whilst epoxies require vigorous surface preparation, methacrylates can be applied on the substrates with minimum surface preparation. Due to the less clean environmental condition of a typical shipyard in the marine industry, surface preparation is vital. Commonly, two

techniques include simple mechanical grinding using hand-held 'angle grinders' and utilizing peel ply in which a textured polymer sheet covers the uncured laminate and peeled off when to provide a clean adherend surface. Furthermore, the surface of the substrate can be cleaned by using a dry cloth and then wiping acetone. It is important to keep in mind that a clean surface is a necessary condition for adhesion, but it is not a sufficient condition for bond durability.

Most metal adherends are coated with adhesive primers after cleaning and surface preparation. Adhesives primers are dilute solutions of adhesive in an organic solver, specially formulated to be a strong intermediate layer between the aluminum surface and the adhesive bond line (Pate, 2002). Their main function is to wet the freshly prepared surface easily and, after drying or curing, to protect the adherend' s surface from oxidation, extending the time that may elapse between surface preparation and adhesive application. Its corrosion-inhibiting contribution is also important.

The last part of the manufacturing process includes the adhesive application, the assembly and, most of the time, the curing of the substrates. Common film adhesives are applied by laying the adhesive manually on the facing surface, taking care not to allow wrinkles to develop, or air to become entrapped between the adhesive and the substrate surface. Two great challenges of the process of assembling are (a) the proper alignment of the substrates and (b) the consistency and the uniformity of the bond line thickness across the entire bonded area. Some types of tooling or assembly equipment, in the form of jigs, fixtures or glass beads (ballotini), shown in Figure 1.26 and spacers added in the adhesive, is required to control accurately the alignment, the tolerance and fit of the adherends. Hydraulic presses and ovens or autoclaves are variously required depending on the size of the components and the adhesive to be used. In large scale production, dispensing/ application equipment will be necessary. The function of assembly equipment is to locate and retain components together throughout the bonding process (Adams & Comyn, 2000; An overview of assembly tooling for adhesive bonding 2005).
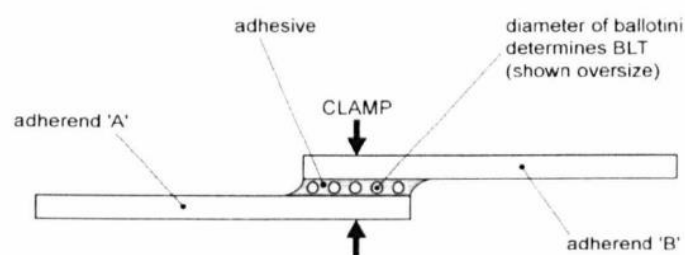
Figure 1. 26 Lap joint using ballotini-loaded adhesive for bond line thickness (BLT) control
(An overview of assembly tooling for adhesive bonding, 2005)

Monteiro et al., 2015 while conducting experiments to measure the properties of the structural adhesive Sikapower 4720, described the steps they followed in order to achieve a precisely controlled set up. In particular, the adherends were cured in a jig (Figure 1.27) that ensures the precise alignment of the adherends and correct overlap length. The specimens were assembled using 1 mm spacers between adherends to attain the correct value of overlap length. These spacers and all the mounting jig surfaces potentially in contact with the adhesive were coated with demolding agent to facilitate extraction of the specimens after curing.
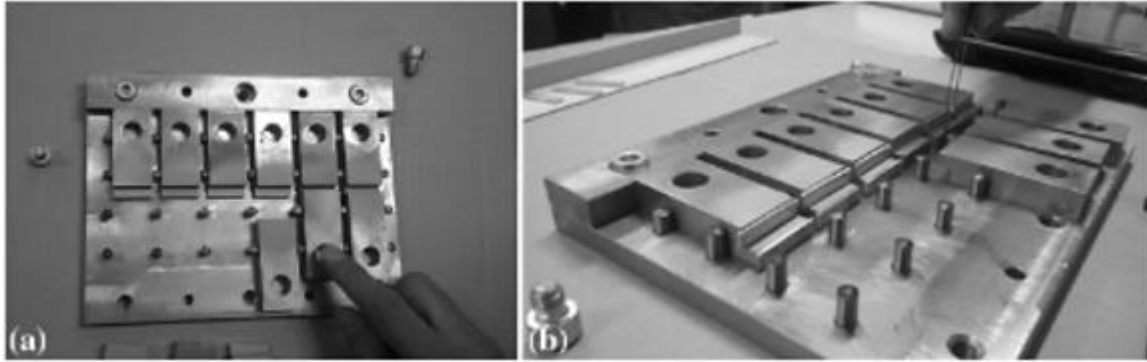
Figure 1.27 Adherents placing in the jig: (a) alignment of the adherends and (b) placement of the spacers.

In case of tubular adhesive joints, the accomplishment of the co-axiality of the tubular adherends is a challenging part of the process. Le Pavic et al. (2020) used the set-up visible in Figure 1.28 to ensure the co-axiality of the adherents. The position of the first substrate is made by a mechanical stop. After applying adhesive on both sides of the substrate, the second substrate is put in position according to an adjustment ring which determines the bonding length. The sample is clamped onto the bonding set-up as illustrated in Figure 1.28 (e) during the curing process.
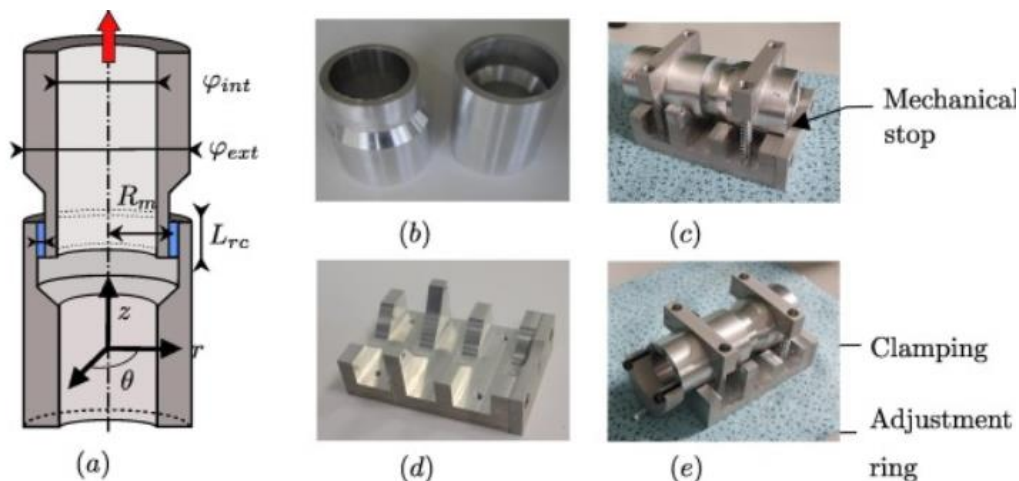
Figure 1.28 Tubular sample (a) schematic view cut and dimensions (b) aluminum substrates (c) adhesive bonding set-up (d) and (e) clamping and adhesive length control.

Barbosa et al. (2018) described the experimental set ups, required for the experimental part of the structural comparison of different joint configurations. The SLJ, DLJ, stepped lap and scarf joints were assembled to cure in a steel mould, to ensure a proper adherends' alignment and the correct value of overlap length. To obtain the specified adhesive thickness, steel blocks with calibrated dimensions were used to support the upper adherend (SLJ) and inner and upper adherends (DLJ). The other joint types did not require this setup because the adherends are naturally aligned. For the scarf joints, clamps were used to position and align the adherends and, to obtain the specified adhesive thickness, calibrated wire with 0.2 mm of diameter was applied between the adherends. The time of cure for all joints was a minimum of 48 h, at room temperature. To remove the excess adhesive at the overlap zone, milling techniques were applied.

1.2.5 Common failure modes of adhesive joints

Due to the developments in adhesive technology, the interest for the failure mechanism of adhesively bonded joints has increased significantly. Depending on the design, a bonded joint which includes at least one fiber composite substrate fails in different ways. In the standard ASTM D5573, a classification of the different failure modes has been published. The standard distinguishes between six different failure modes presented in Figure 1.29. The factor which determines the failure mode of a specimen is the difference between the cohesive and adhesive resistances and the resistance of the substrate. The failure will firstly occur at the point of least resistance.
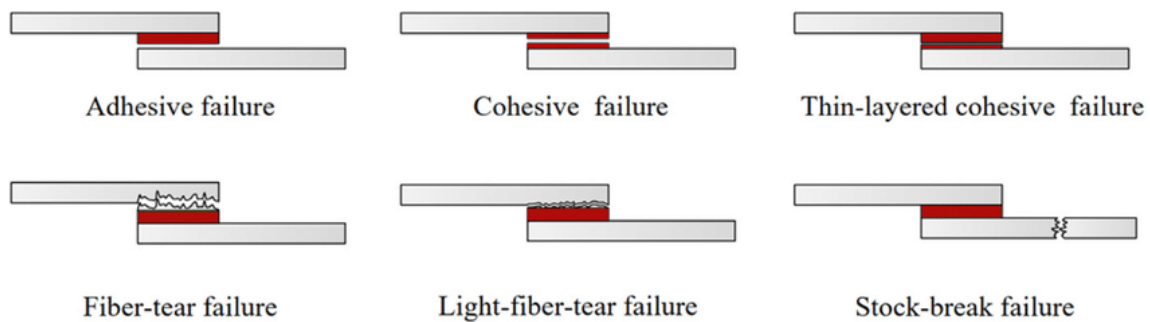
Figure 1.29 Sketches illustrating failure modes in adhesively bonded joints according to ASTM D5573

Adhesive failure describes an interfacial bond failure between the adhesive and the adherend. This failure mode occurs usually due to an inadequate bonding process, especially due to insufficient surface pretreatment. This type of failure must be avoided under all circumstances. Cohesive failure refers to a failure purely within the bondline, allowing a layer of adhesive to remain on both surfaces. In this failure mode, the cohesive strength of the adhesive or fusion bond is reached. Thin-layered cohesive failure describes a cohesive failure near the interface of adhesive and adherend. This occurs when cracks initiated in the adhesive layer tend to propagate towards one adherend. If failure is located in the adherends near the bond, the failure is termed fiber-tear or light-fiber-tear failure. The presence of these types of failure depends on the transverse properties like interlaminar composite strength and the stacking sequence in the composite adherends. If the bond strength is greater than the laminate strength, stock-break failure occurs. In this case, the structure fails due to adherend breakage outside of the bond. Cohesive failure or adherend failure is the ideal failure mode because the adhesive joint can obtain maximum strength under these circumstances. According to Sun et al., 2019, a large number of research have shown that the design parameters of the adherend and adhesive, such as overlap length, adherend width, adhesive thickness, adherend thickness, surface pretreatment state and the environmental factors all have influences on the strength and the carrying efficiency of SLJs.

In case of composite structures, primary failure modes for composite substrates are buckling, local delamination, and fatigue. Buckling, in particular, is one of the most important failure modes for composite structures which have low modulus of elasticity. For all kinds of loading on skins and joints between composite materials, local delamination is one of the most severe failure modes since it can result in catastrophic failure for the global system structure.

28

Interlaminar shear strength and through-thickness normal strength must then be carefully designed to prevent composite structures from local delamination. The initiation of the various failure modes depends on the material properties of the constituents (facings, adhesive, and core), geometric dimensions, and type of loading (Banea & da Silva, 2009).

In conclusion, the ultimate strength of a joint is a more important criterion than the mode of joint failure. An analysis of failure mode, nevertheless, can be an extremely useful tool in determining whether the failure was due to a weak boundary layer or due to improper surface preparation.

1.3 Literature survey

1.3.1 Cylindrical pressure vessels

Over the years various naval research programs and European projects have conducted studies on a range of materials and geometries of pressure vessels, able to withstand the underwater loading conditions. Several academic studies have worked on the performance and the optimization of these pressure vessels, especially focusing on the buckling effect caused by high external pressure.

Tsouvalis et al. (2000) conducted a parametric study of a carbon/epoxy composite laminated cylinder under the action of external hydrostatic pressure. The cylinder had an internal diameter of 175mm and length of 400mm. It was modeled in SOLVIA, version 95.0 as presented in Figure 1.30. The structure included flat metallic or hemispherical composite end closures. The domes were connected to the composite cylinder via two pairs of metallic transition rings, adhesively bonded to the cylinder. The results of the study showed that the cylinders with flat, rigid end plates were quite stiffer with respect to buckling, for all thicknesses and stacking sequences examined. Also, it was observed that cylinders with end plates achieved their maximum buckling load when angle θ varies in the range between 50° and 60°, depending on the R/t ratio, accounting for the stacking sequences 90°n/(±θ)n, (90°/±θ)n and (±θ)n.
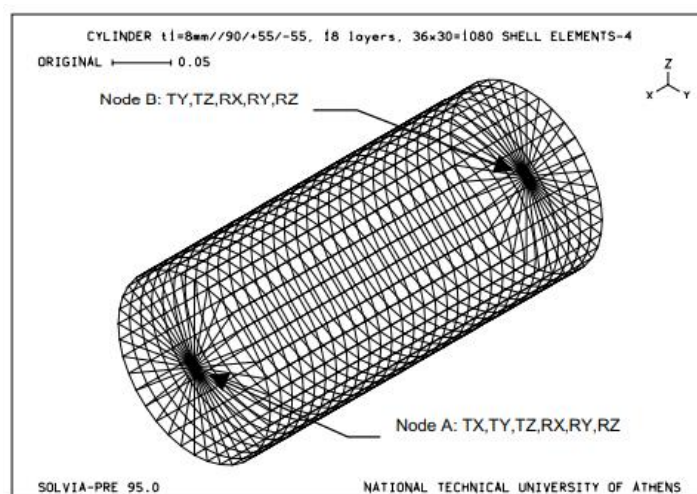
Figure 1.30 Finite Element Model with flat ends (Tsouvalis et al., 2000)

Ross et al. (2009) described an experimental and an analytical investigation into the collapse of 44 circular cylindrical composite tubes under external hydrostatic pressure (shown in Figure 1.31). The specimens had an external diameter of 45mm, thickness of 1.4mm and various lengths. For sealing the two ends of each specimen under external water pressure, two end steel bungs with 'O' rings had to be manufactured. The authors conclude that the short vessels collapsed through axisymmetric deformation while the longer tubes collapsed through non-symmetric bifurcation buckling. In addition, the tested specimens failed at locations were the lay-up of the single layers changed. These changes seem to reduce the strength of the composite in this location.
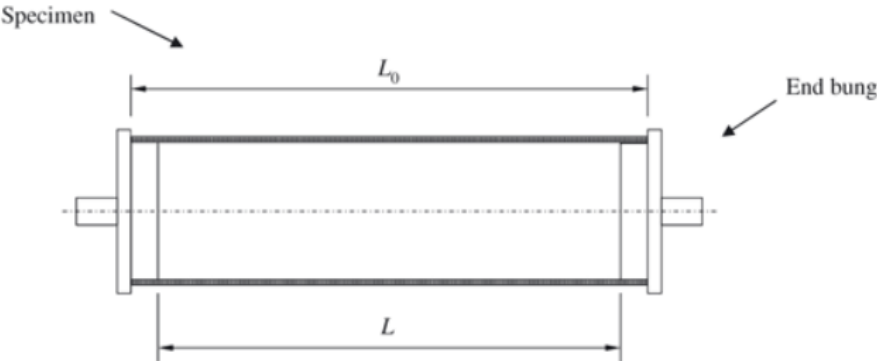
Figure 1.31 Composite cylinder specimen where Lo, the nominal length and L, the unsupported length (Ross et al., 2009)

Another study that examines, through finite element analysis and testing for underwater vehicle applications, the buckling and failure characteristics of moderately thick-walled filament-wound carbon–epoxy composite cylinders under external hydrostatic pressure was conducted by Moon et al. (2010). All the cylinders had a 300-mm nominal inner diameter, a 695-mm nominal axial length and an 8-mm nominal thickness. The tested winding angles were $[\pm 30/90]_{FW}$, $[\pm 45/90]_{FW}$ and $[\pm 60/90]_{FW}$. The composite cylinders were bonded with flanges made of A36 steel at room temperature by a hardening adhesive, as presented in Figure 1.32. In both the experiments and analyses, the cylinders with a $\pm 60°$ helical wind angle showed the highest buckling pressure.
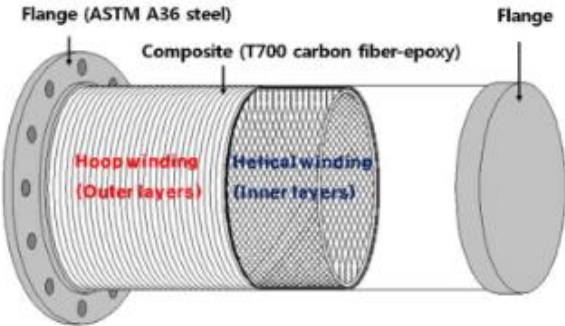
Figure 1.32 Schematic of a filament-wound composite cylinder with flange (Moon et al., 2010)

A more recent study, conducted by Arhant et al. (2019) focused on designing, manufacturing, and testing thermoplastic composite pressure vessels for 4500 m depth. The implosion performance of thermoplastic composite cylinders was compared to the filament

wound C/Epoxy reference, experimentally and numerically. The results showed that the cylinders reinforced with fibers at [± 55°] a higher implosion pressure was achieved for the C/Epoxy reference, at 772 bar. The C/PA6 stacking sequence was then optimized to [±0°/ 88°], which provided a much stiffer behavior than the [± 55°] angle. This cylinder imploded at 610 bars. Figure 1.33 presents the damaged specimens after implosion.

Figure 1.33 Composite cylinders after implosion tests. From left to right (i) C/PA6 [± 0°/88°], (ii) C/PA6 [0°/ ± 55°], (iii) C/Epoxy [± 55°] (Arhant et al., 2009)

1.3.2 Adhesive joints characteristics

The structural behavior of single lap adhesive joints (SLJs) under tensile loading has concerned the scientific community. Sun et al. (2019) implemented both experimental tests and numerical simulation to investigate the tensile performance of adhesively bonded CFRP SLJs. It was found that increasing the adherend width can improve the load carrying capacity of the joint better than increasing the overlap length does. Moreover, choosing 0° ply as the first ply (the ply in contact with the adhesive layer) is also beneficial for upgrading joint's strength. With respect to failure modes, cohesive failure in adhesive and delamination in adherend take dominant, while matrix cracking and fiber fracture only play a small part. Ozel et al. (2014) investigates the mechanical properties of SLJ geometry with different configurations and materials of lower and upper adherends under tensile loading. According to the results obtained from finite element analysis, peel and shear stresses took maximum values at the ends of the overlap length while, stress values decreased and nearly became zero towards the middle parts of the overlap length. Moreover, in every case of the examined joints, the increase in the overlap length increased the load carrying capacity. Regarding the case of two dissimilar (aluminum and carbon/epoxy) substrates of the same thickness, a stacking sequence of $[0°]_{16}$ carried more load than joint types having other stacking sequences, with the second better option, in terms of joint strength, stacking sequence with the first ply 0°.

Drive shafts and piping systems made of composite material attract particular interest in recent years. Flanges or similar components are necessary for the connection of the shaft to

the engine system or the connection of the pipes to the entire network. Since, the materials are dissimilar in most cases, the connection is accomplished by SLJs. Many research and studies focus on the tubular lap joints, mainly, subjected to torsional and tensile loading. Kim et al. (2001) investigated the torque transmission capability of the adhesively bonded composite shaft with respect to overlap bonding length and end-cap thickness by finite element method and compared with the experimental result. In the research work of Das & Pradhan (2010), material strength as well as a fracture mechanics approach were employed to study the effect of fiber architecture on the failure characteristics of an adhesive joint subjected to tensile loading. It was finally concluded that the magnitudes of the peel stresses are significantly higher compared to the shearing stresses in all the critical surfaces in the overlap region. Adhesion failure initiates at the edge of the inner adherend– adhesive interface of the overlap length nearer to the clamped end of the tubular single lap joint, shown in Figure 1.34.
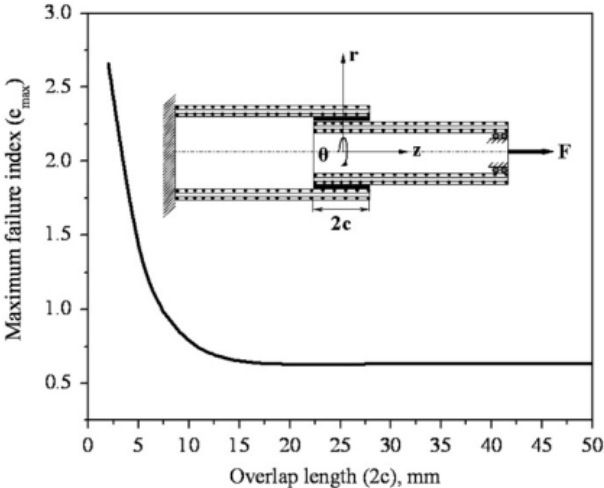
Figure 1.34 Failure index in relation with overlap length (Kim et al., 2001)

In the framework of his diploma thesis, Fredrik Fors (2010) investigates numerically the design of a turbine exhaust duct, subjected to internal pressure and made of carbon fiber composite material with adhesively attached titanium flanges, using a cohesive zone material (CZM) to model the adhesive layer. Figure 1.35 shows the meshed submodel which is used for the detailed analysis of the tubular scarf joint. The results show that the applied thermal and structural loading causes local stress concentrations on the adhesive surface, but the stresses are not high enough to cause damage to the joint if a suitable joint design is used.
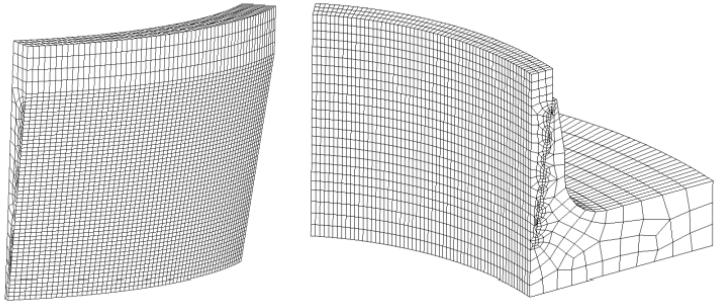
Figure 1.35 Meshed geometry of the submodel (Fors, 2010)

1.4 Objectives of the thesis

As composite pressure vessels with adhesively bonded metal components are widely used in various fields such as the oceanographic and marine industries, the knowledge of their mechanical behavior and failure risks becomes of greater importance. High strength, light weight, fatigue, and corrosion resistance are the main advantages.

However, their efficient design remains an issue. One of the reasons is the problem of understanding and analyzing composite material structural behavior and their failure modes and mechanisms, due to their anisotropic nature. Consequently, the failure mode of the composite cylinders is hard to be calculated and, accurately, predicted. The inherent complexity of composite pressure vessels at the design stage imposes the adoption of conservative safety factors, resulting in FRP structures with low performance.

As it has been seen in the previous section, the focus of the adhesive joint literature references is the SLJ configuration. Therefore, more complicated joint configurations, such as L-shape or T-shape joints, suffer from a lack of design rules, empirical data, and models, required to optimize the design of structures using them. Barbosa et al. (2018) mentions that adhesively bonded joints are yet not dependable in critical connections because of issues like fatigue and long-term behaviour uncertainties, and large scatter in the failure loads.

The analysis of the mechanical behavior of the composite cylinder and the adhesive joint constitutes two separated issues, even if they concern the same structure. Consequently, complete structural analyses of every component of the pressure vessels are hard to find.

This thesis investigates the efficient design of a filament-wound pressure vessel with adhesively attached aluminum end-caps under hydrostatic pressure. The focus of the project has been on stress analyses of the adhesive joints between the composite cylinder and the metal end-caps using Finite Element Methods (FEM). Initially, a linear static analysis is used for the design optimization of the adhesive joint area through a parametric study. The parametric study is done based on a FE model of solid sliced part of the whole structure, since it less source demanding. Afterwards, eigenvalue and nonlinear buckling analysis, which reflects reality better, are conducted to determine the final geometry of the vessel. These two analyses are conducted using a solid full cylindrical FE model.

CHAPTER 2

Governing regulations and problem description

2.1 Classification societies rules

As composite cylinders and pressure vessels are gaining ground in marine applications, international standards and codes as well as regulations from shipping registers try to follow up the increasing demand for rules and regulations for the use of composite materials on pressure vessels.

European standard EN13445:2021 Unfired pressure vessels

EN13445 specifies the requirements for design, construction, inspection, and testing of unfired pressure vessels. The term unfired excludes vessels that are subject to direct generated heat or flame impingement from a fired process. This European standard includes 10 parts, which are presented briefly in Table 2.1.

Table 2.1 Presentation of the 10 parts of EN13445 (BS EN13445)

Part	Description
#1	contains general information on the scope of the standard
#2	deals with the general philosophy on materials, material grouping and low temperature behaviour, limited to steel and steel castings
#3	gives the rules to be used for design and calculation under internal and/or external pressure, local loads, and actions other than pressure.
#4	specifies requirements for the manufacture of unfired pressure vessels and their connections to non-pressure parts (manufacturing tolerances, welding requirements, requirements for permanent joints other than welding).
#5	covers all those inspection and testing activities associated with the verification of the pressure vessel for compliance with the standard,
#6	contains special rules for material, design, fabrication, inspection, and testing of pressure vessels made from spheroidal graphite cast iron.
#7	part gives guidance on how to use the conformity assessment procedures in the Pressure Equipment Directive 97/23/EC.
#8	contains special rules for material, design, fabrication, inspection, and testing of pressure vessels made from aluminum and aluminum alloys.
#9	details the conformance of the whole EN 13445 series to ISO 16528-1 "Boilers and pressure vessels — Part 1: Performance requirements". This is a CEN Technical Report.
#10	contains special rules for material, design, fabrication, inspection, and testing of pressure vessels made from nickel and nickel alloys.

Even though pressure vessels made of metal and not composite materials are included in the regulatory framework, it seems interesting to mention the content which is close to our field of interest. Hence, the points where the existing rules can be extended to the use of composite materials will be clearer.

Part 3 of European Standard (EN13445-3:2021) specifies requirements for the design of pressure vessels. In Section 8.4, it is mentioned that the thickness of a component under external pressure shall be not less than that required by this standard under the same pressure applied internally. Additionally, the minimum safety factor which applies throughout this clause is given by: For design conditions S = 1.5 and for testing conditions S= 1.1. In Chapter 10, methods for determining the thickness of circular and non-circular unstayed flat ends under pressure are specified. Flat ends welded or bolted to the cylindrical shell are considered. Chapter 11 analyzes design of circular bolted flange connections, while chapter 12 specifies the design of bolted domed ends, with either full face or narrow face gaskets.

Part 5 of European Standard (EN13445-5:2021) specifies the inspection and testing of individual and serially produced pressure vessels made of steels. Each individual vessel shall be inspected during construction and upon completion. Inspections shall be made to ensure that in all respects the design, materials, manufacturing, and testing comply with the requirements of this standard. Documented evidence shall be prepared to verify implementation of this requirement. The type and amount of non-destructive testing of a pressure vessel shall be based upon the testing group or combination of testing groups according to Chapter 6.

Boiler and Pressure Vessel Code (BPVC) ASME

The ASME Boiler & Pressure Vessel Code (BPVC) is an American Society of Mechanical Engineers (ASME) standard that regulates the design and construction of boilers and pressure vessels. It provides rules and requirements across new materials, applications, and technologies, including safety rules and guidelines for construction of pressure devices. The Code does not contain rules to cover all details of design and construction of pressure vessels. Where complete details are not given, it is intended that the manufacturer, subject to the acceptance of the Authorized Inspector, shall provide details of design and construction which will be as safe as otherwise provided by the rules in the Code. The latest official edition, ASME BPVC 2021, is categorized in 13 sections, as presented in Table 2.2.

Table 2.2 Presentation of the 13 sections of the ASME BPVC
(https://www.asme.org/codes-standards/bpvc-standards)

Section	Description
I	Rules for construction of power boilers
II	Materials
III	Rules for construction of nuclear facility components
IV	Rules for construction of heating boilers
V	Nondestructive examination
VI	Recommended rules for the care and operation of heating boilers
VII	Recommended guidelines for the care of power boilers
VIII	Rules for construction of pressure vessels
IX	Welding, brazing and fusing qualifications
X	Fiber-reinforced plastic pressure vessels
XI	Rules for in-service inspection of nuclear power plants
XII	Rules for construction and continued service of transport tanks
XIII	Rules for overpressure protection

Specifically, Section X establishes the minimum requirements for the construction of fiberglass-reinforced thermosetting plastic pressure vessels for general service and sets limitations on the permissible service conditions. A thorough search was conducted but the latest version of Section X with free access was not available. The following information come from the version of 1969 of Section X, the official brochure "2017 ASME Boiler and Pressure Vessel Code, AN INTERNATIONAL CODE" and a presentation in the context of ASME National Board Chief Inspectors Technical Program 2015.

Section X includes three Classes of vessel design: Class I (concerning 150, 1500 and 3000 psig maximum pressure), Class II (concerning 250 psig maximum pressure) and Class III (concerning 15,000 psig maximum pressure). It should be noted that pounds per square in gauge or psig, is a measure of pressure with respect to the atmospheric pressure (1 psig = 0.069 bar). The maximum temperature limitations are 250° F for Class I and II and 185°F for Class III or 35°F below the maximum use temperature of the resin, while the minimum temperature limitations are -65°F.

During the fabrication process, documents that specify the materials and the procedure employed to fabricate or assemble a part, called Data Report Forms, are mandatory to be filled by the manufacturers and signed by authorized Boiler and Pressure Vessel Inspectors. For instance, the Form Q-120 for the procedure specification for Class II vessels (version 2017) was found on the Internet. According to the form, the material properties used in design as well as in fabrication phase should be noted. In addition, the results of quality checks, including visual check, thickness, and dimensional checks, Barcol hardness check and thermoplastic liner integrity (if applicable) are mandatory to be mentioned. The Form includes also assembly identification data (surface preparation method and distance from mating joint to name but a few) in case of joint existence between two or more separately fabricated parts.

Testing procedures are required by Section X of ASME BPVC and categorized depending on the Class of the pressure vessel. In Class I, a wide variety of laminates can be used, and the vessel is qualified through a cyclic and destructive test of prototype. In Class II, also a wide variety of laminates can be used. Design of Class II vessels by a licensed professional engineer was mandatory, using material properties derived from representative lamina mechanical testing. The reason is that unlike metal industry, FRP fabrication industry determines material properties in place as the vessel is finally cured. Mandatory acoustic emission (AE) testing of completed vessels would verify design adequacy, that the tank was structurally sound and free of major manufacturing defects (Richter, 2004). In Class III, filament wound laminates are typically used with the possibility of using a load sharing metallic or non-metallic liner. Design, fabrication, and examination requirements have been specified, included Acoustic Emission testing at time of manufacture. The Code rules include the design qualification testing of prototype vessels. Qualification includes proof, expansion, burst, cyclic fatigue, creep, flaw, permeability, torque, penetration, and environmental testing (Newhouse et al., 2010).

More specifically, the acoustic emission (AE) testing is an active method of non-destructive testing (visualized in Figure 2.1), monitoring the acoustic response to an applied load. AE works as a pass/fail test for Class II and Class III vessels. The Barcol hardness testing determines the surface indentation hardness of the resin, which is directly related to the degree of cure, in accordance with ASTM 2583. As for the pressure testing, it includes cyclic loading

and 6 times design pressure application for Class I vessels. A hydrostatic head test, which is a measure of the opposition to the passage of water through the fabric, and 1.1 times the design pressure are applied and tested with AE for Class II vessels, while a hydrostatic head and 1.25 times the design pressure are applied for Class III vessels.
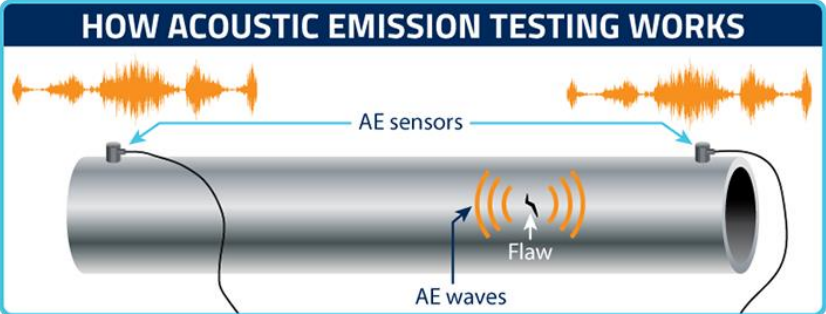
Figure 2.1 AE testing (https://www.acuren.com/)

Rules specifications of Bureau Veritas

Bureau Veritas (BV) does not offer rules specifically dedicated to filament wound cylinders, however it offers a rule note for the manufacture and study of hulls made of composite materials.

"Hull in Composite Materials and Plywood, Material Approval, Design Principles, Construction and Survey, October 2021" Rule Note NR546 is applicable to ship structures having their hull and superstructure totally or partly made of composite materials or plywood. The document is categorized in eleven sections, presented in the Table 2.3. As it is visible in the Table, many sections concern ship equipment. Focusing on parts related to composite materials and adhesive joining, sections, and subsections in the field of our interest are analyzed in particular.

Table 2.3 Presentation of the eleven sections of the BV NR546

Section	Description
1	General requirements and calculation principles
2	Scantling criteria and hull strength analysis
3	Main structure arrangements and special features
4	Raw materials for laminates
5	Individual layers for laminates
6	Laminate characteristics and panel analysis
7	Stiffener analysis
8	Plate and stiffener analysis for plywood structure
9	Scantling of pillars in composite materials
10	Composite shaft line
11	Hull construction, survey, tank tests and mechanical tests and raw material homologation

In Section 2, the scantling criteria and the hull strength analysis are described. In subsection 1.2, the types of stresses considered are defined. As it is written specifically, *the different types of stresses considered to estimate the actual safety factors are: a) For main stresses analysis in each individual layer ("ply by ply" analysis): • Main tensile or compressive stresses σ_1 in the longitudinal direction of the fiber, mostly located in: - 0° direction of unidirectional tape - 0° and 90° directions of woven roving when the set of fibers are interweaved • Main tensile or compressive stresses σ_2 in the perpendicular direction of the fiber, mostly located in: - 90° direction of unidirectional tape or combined fabrics when the set of fibers are stitched together without crisscrossing of fiber • Main shear stresses parallel to the fiber located in the plane of the individual layer (τ_{12}) and/or between each individual layer (τ_{IL1} and τ_{IL2}, also designated as inter-laminar shear stresses).* For buckling analysis in the whole laminate: • *compression stresses in the longitudinal and transverse directions of the panel or structure element • shear stresses in the plane of the panel or structure element.*

The minimum rule safety factors (SFs) are defined in relation with the following partial safety factors:

- C_V (partial safety factor taking into account the ageing effect),
- C_F (partial safety factor taking into account the fabrication process and the reproducibility of the fabrication, directly linked to the mechanical characteristics of the laminates),
- C_i (partial safety factor taking into account the type of loads (sea pressure, dynamic sea pressure or internal pressure)),
- C_{CS} (partial safety factor for combined stresses in the individual layers of the laminates)
- C_B (partial safety factor for laminate panel buckling)

In the case of combined stress analysis, the minimum rule SF in each layer is to fulfil the following condition:

$$SF \geq C_{CS} \cdot C_F \cdot C_V \cdot C_i \tag{2.1}$$

The minimum buckling rule safety factor SF_B, applicable to the whole laminate panel or stiffener is to fulfil the following condition:

$$SF_B \geq C_B \cdot C_F \cdot C_V \cdot C_i \tag{2.2}$$

In the current study, the partial safety factors are taken equal to the values defined in Table 2.4 and are introduced in the relations (2.1) and (2.2). Therefore, in case of stress analysis, the minimum permissible SF equals to 2.24 and in the case of buckling analysis, the minimum permissible SF_B equals to 1.91.

Table 2.4 Partial Safety Factor values

Coefficient	Symbol	Value	Description
Coefficient considering the ageing effect of the composites	C_V	1.2	Monolithic laminate
Coefficient considering the fabrication process and reproductibility	C_F	1.1	Preg, filament winding
Coefficient for combined stress	C_{CS}	1.7	UD, Biaxial, Triaxial
Type of load factor	C_i	1	
Buckling coefficient	C_B	1.45	

Section 4 concerns the materials used for the laminates. In the beginning, the different resin systems, polyester, vinyl ester and epoxy resin systems, and their characteristics are stated. Afterwards, the reinforcement materials (glass, carbon, and para-aramid) and their configuration (unidirectional UD, woven rovings WR, chopped strand mats CSM and combined fabrics) are analyzed in terms of their mechanical characteristics. Structural adhesives are also included in this section. As it is mentioned in the document, the definition of typical mechanical characteristics of gluing joint is difficult due to the extensive range of adhesive resin systems, curing adhesive process, type of components to be bonded, surface preparation and treatment and the large variety of joint geometry. It is noted that, *the value of the shear breaking stress considered in the present Rule Note is to be taken equal to the minimum value of the:*

- *initial shear yield stress, in N/mm², of the bonding resin specified by the manufacturer, corresponding to the initial yield stress on a substrate equivalent to the examined components, or*

- *theoretical breaking stress value τ_{IL}, in N/mm², of the first layer of the components bonded together.*

  Such breaking stress is to be established on a test set up that induce homogeneous shear stress along the bond line, without possibility for stress redistribution.

According to the Rule Note, the shear breaking stress may be determined on the basis of shear stress-strain curve as the intersection of a line tangent to the linear elastic region and a line tangent to the nonlinear plastic region of the curve as it is shown in Figure 2.2. This curve is to be defined taking into account the maximum air temperature provided in service. Other values of shear breaking stress deduced from mechanical tests representative of the gluing joint parameters, in accordance with ISO 527 or ASTM D638 for tensile properties and ISO 11003-2 or ASTM D3983.
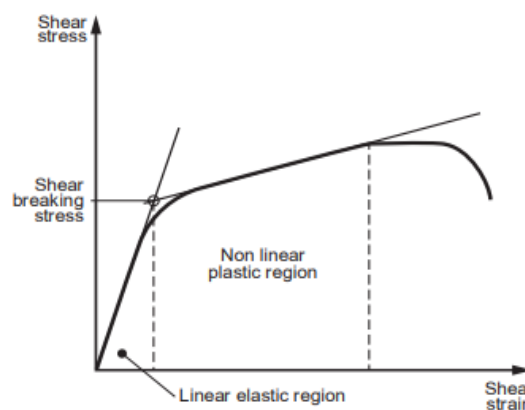
Figure 2.2 Initial yield stress of a typical adhesive (Bureau Veritas NR546)

Section 11 specifies the requirements regarding hull design assessment, construction, survey, mechanical tests, and homologation of raw materials within the scope of the classification and/or certification of ship hulls built in compliance with the applicable Society's Rules. Mechanical tests are done on test pieces taken from the panel in two perpendicular directions. The number of test pieces in each direction depends on the reference standard (usually five in each direction for each test). Each test piece is to be identified with the

Surveyor's agreement and is to specify: (a) the test piece direction in relation to the main longitudinal and transverse axes of the hull and (b) the arrangement of the layers. Table 2.5 gives the types of tests to be performed. In particular cases of structural adhesive joint, mechanical tests are to be conducted for structural gluing joints. The type of tests and the temperature range are to be defined at the satisfaction of the Society. The type and preparation of adherent, the application of adhesive and the curing process of test samples are to be representative of the construction process. The characteristics of the sample tests (geometry and thickness of the gluing joint, stiffness of the adherents) are to be as much as possible representative of the actual joint to be characterized.

Table 2.5 Mechanical type test

Panels	Test types - Standards	Quantity of test pieces	Size of test pieces, in mm **(1) (2)**
Monolithic	Tensile test: ISO 527	• 5 in lengthwise direction of panel • 5 in crosswise direction of panel • 2 test pieces for calibration **(7)**	Length: 400 Width: • 25 where e < 25 • 30 where 25 < e < 30 • 35 where 30 < e < 35, etc.
	3-point bending test: ISO 14125	• 5 in lengthwise direction of panel • 5 in crosswise direction of panel • 2 test pieces for calibration **(7)**	Length: 200 Width: • 25 where e < 25 • 30 where 25 < e < 30 • 35 where 30 < e < 35, etc.
	Measurement of density: ISO 1183 Reinforcement content in weight: ISO 1172 **(3)**	4 samples	30 x 30

(3) For laminate test panels reinforced with carbon and /or para-aramid fibers, the standard ASTMD3171 may be used.
(7) For orthotropic panel, test may be confined to one direction of the panel.

During the construction procedures, Non-Destructive Testing (NDT) is applied. The NDT and the result acceptance criteria are to be defined by the shipyard. The NDT processes may be: ultra-sonic testing, spectroscopy, differential scanning calorimetry (DSC) and radiography. Tank and weather-tight structure testing is also conducted.

2.2 Description of Case Study 1

2.2.1 Thesis project specifications

In the framework of this project, a composite pressure vessel adhesively bonded with metal end-caps is being developed. The pressure vessel is designed to be subjected to internal pressure of 1 bar and external pressure of 40 bar, in natural sea water conditions. The required external diameter equals to 200 mm, while the nominal internal diameter equals to 184 mm. As for the required length of the filament-wound cylinder it is equal to 800mm. The end-caps, made of aluminum, have flat shape and their external diameter is equal or less than the one of the cylinders, for hydrodynamic reasons. In other words, a continuity of form between the cylinder and the end-caps, with no external protrusions, is desired. A crucial functional parameter which influences the design is the possibility of regular accessibility in the interior of the pressure vessel. Therefore, a design concept which enables the assembly and disassembly

of the metal caps is necessary. Towards this aim, the existence of rings or flanges, adhesively bonded to the composite cylinder and bolted to the end-caps, seems an efficient solution. The key questions set out in the initial project specifications are:

- What would the configuration of a metal to composite joint be like to sustain the specified loading conditions?
- Which should be the parameters investigated in order to design a reliable and functional pressure vessel?
- Which component of the structure would be at risk of failing first?

2.2.2 Preliminary joint design concepts

The first step of the design is to define the geometry of the vessel based on the initial specifications and literature references of similar pressure vessel cases. The cross-sectional configuration of the adhesive joint and the dimensions of the components are examined in a preliminary stage.
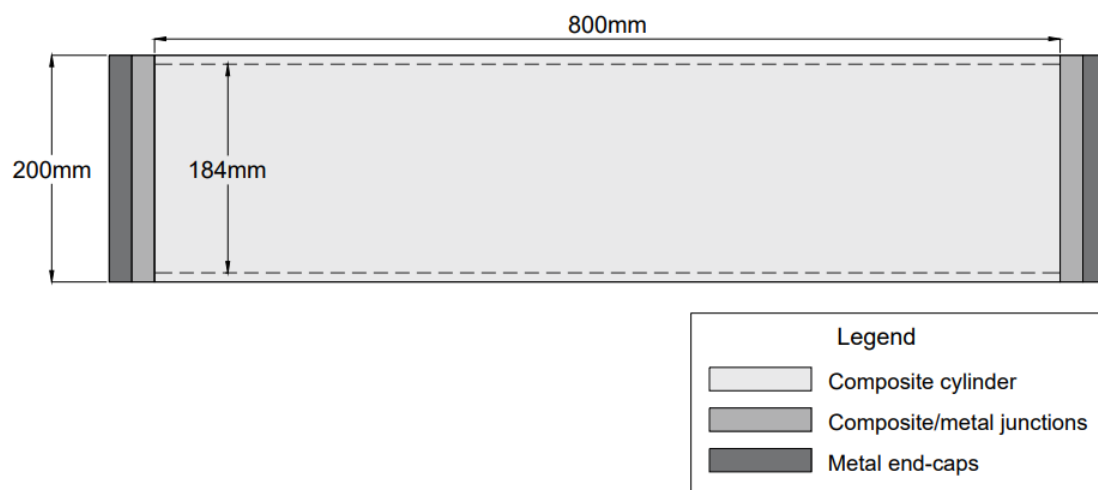
Figure 2.3 Sketch of the pressure vessel presenting the initial requirements

A recapitulation of the requirements (visualized in Figure 2.3) that should be fulfilled is necessary:

(a) application of required dimensions of the composite cylinder (external diameter of 200 mm, internal diameter 184 mm and length 800 mm),

(b) hydrodynamic design of the ring adhesively attached to the cylinder and the flat circular end-cap with external diameter of 200 mm,

(c) enough thickness of both flange and end-cap for drilling holes of the bolted connection and

(d) existence of an O-ring required for maintaining high sealing capacity of the flange end-cap connection.

After literature search for the design of the underwater pressure vessels, which has been already analyzed in Section 1.3, the most inspiring configurations between the end-cup and the cylinder are presented briefly in Table 2.6.

Table 2.6 Useful configurations of cylinder-end cap/cylinder-flange connection
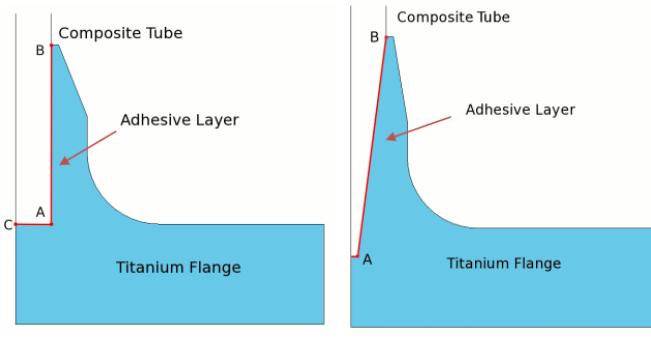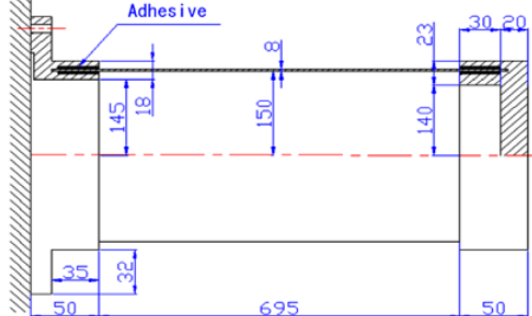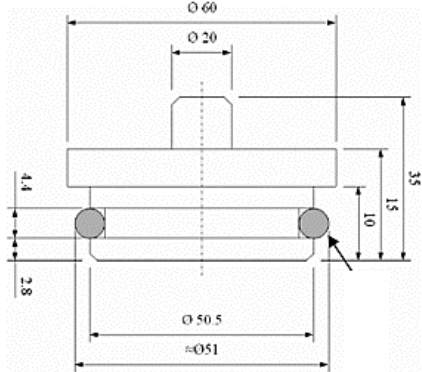
Fors (2010) investigates the design of a composite duct adhesively bonded with a titanium flange subjected to internal pressure.	
Moon et al. (2010) conducts a buckling study on a filament-wound cylinder adhesively bonded with metal flanges under hydrostatic pressure up to 10MPa.	
Ross et al. (2009) examines cylindrical composite tubes of different lengths under external hydrostatic pressure. For the experiments, two end steel bungs with 'O' rings are used without being adhesively bonded to the cylinder.	
Arhant et al. (2019) focused on designing, manufacturing, and testing thermoplastic composite pressure vessels. For implosion tests, aluminium end covers were bonded to the cylinder extremities.	

Figure 2.4 presents the sketches of the cross-sectional geometric concepts of six predesigns. It is clarified that these are conceptual, indicative and non-dimensioned drawings, aiming at the visualization of the first design concepts that came up from combining the required specifications with ideas from the literature review.

- Predesign No 0 depicts the simplest design that comes to mind. It includes a tubular butt joint between the metallic ring and the composite cylinder edge. The O-ring is placed in a

groove in the interface between the end-cap and the metal ring, located inside from the bolt, towards the axis of the cylinder. Its position secures the tightness from leakages that may come from either the ring-end-cap interface or the hole of the bolt. Under external pressure conditions, the stresses developed in the adhesive in the axial cylindrical direction are predicted to be mainly compressive, but the external circumference of the adhesive layer is prone to tensile stresses and, perhaps, cleavage loading. As it has been shown in Figure 1.12 (Adams & Comyn, 2000), structural adhesives perform worst in tension or cleavage. Moreover, the surface of adhesion, dependent on the thickness of the cylinder, does not seem sufficient.

- Predesign No 1 introduces a ring geometry with a protruding inner part, forming a tubular L-shape joint where the composite tube is placed in the outer circumference of the metal ring. This type of joint combines a tubular butt joint and a tubular SLJ, increasing significantly the adhesion surface due to the SLJ, compared to Predesign No 0. It is highlighted that, in this case, the loads aligned with the axial direction are received not only by the butt joint but also by the SLJ. The latter is loaded in shear and compression, which is the desired loading case for adhesives. The O-ring is placed in a groove in the interface between the end-cap and the metal ring, located inside from the bolt, towards the axis of the cylinder in order to secure the tightness from leakages that may come from either the ring-end-cap interface or the hole of the bolt. A drawback of this predesign is the finally reduced maximum effective internal diameter of the pressure vessel, due to the protruded ring. Hence, the accessibility and placement of equipment as wide as the maximum effective inner cylinder diameter is restricted.

- Predesign No 2 makes use of a minimally designed ring which is bonded on the tapered end of the composite cylinder. The O-ring is placed in a groove in the interface between the end-cap and the metal ring, located in a similar position as in the previous predesigns. The advantage of this concept is the existence of a compact ring which offers increased adhesion surface thanks to the scarf joint. In addition, the inclined configuration of the adhesive layer serves efficiently both peel and shear stresses simultaneously. Nevertheless, it is underlined that this tapered end of the cylinder requires milling process after the filament winding, causing possible local fiber damage or delamination. Attention should be paid, also, during the surface preparation and the adjustment of the cylinder with the ring as the cylinder will probably have surface imperfections caused by milling. This can lead to an adhesive layer of non-uniform thickness.

In the above mentioned end-cap predesign versions, the bolt is screwed in parallel with the cylindrical axial direction. Therefore, the application of the necessary fastening torque enables the application of the right value of the axial force for the tightness of the vessel. Another observation is the limited available area for the O-ring groove in the metal ring, especially in the cases of predesigns No 0 and No 2.
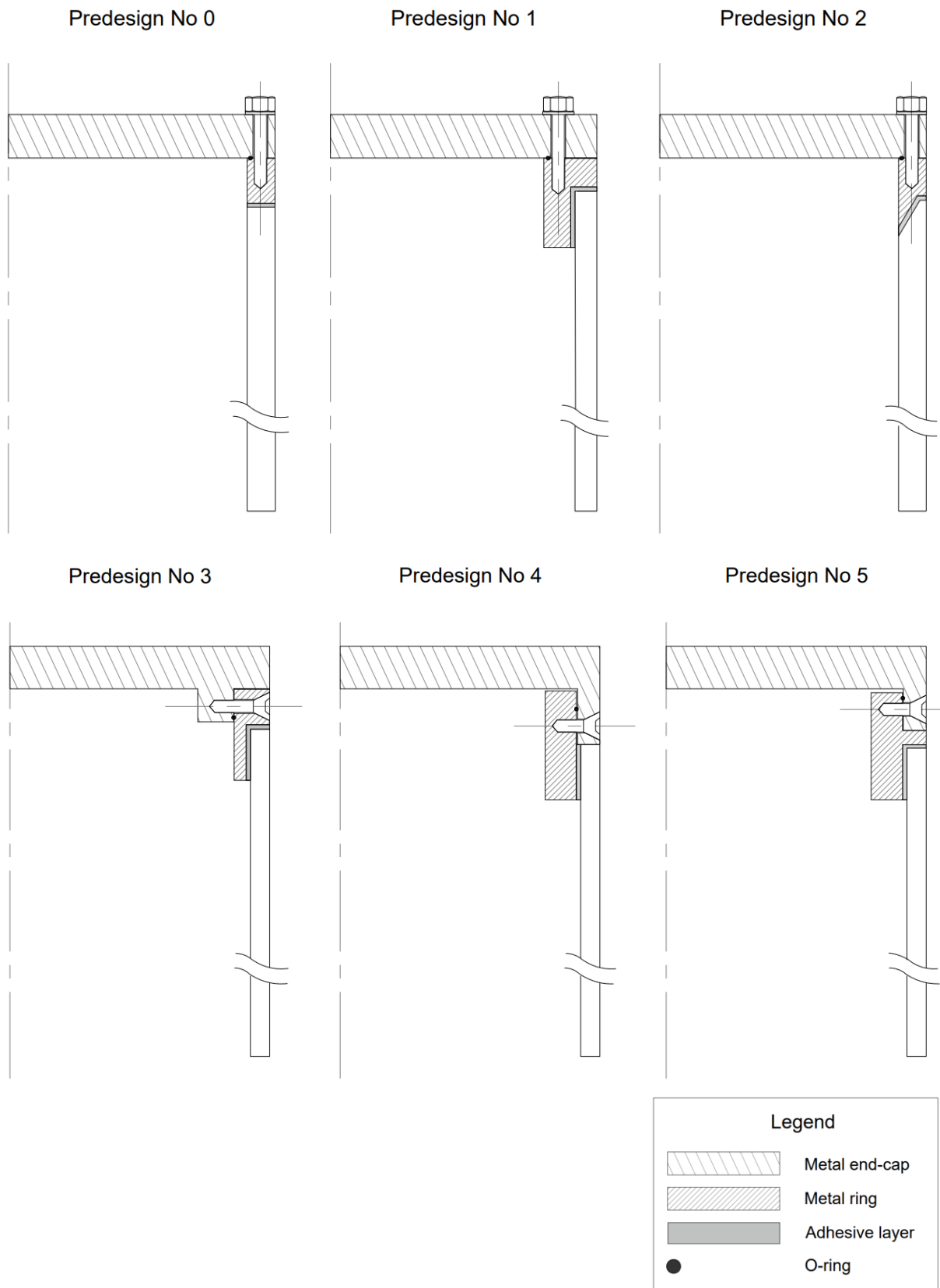
Figure 2.4 Sketches of preliminary design concepts

Another design concept that is examined is a bolted connection perpendicular to the cylindrical axial direction, presented in the last three predesign versions in Figure 2.4. In this case, fastening with bolts does not entail the tightness of the structure. A careful dimensioning and adjustment are required to avoid undesirable space between the end-cap and the ring. In order to meet the requirement for hydrodynamic shape of the vessel, countersunk bolts are the selected choice.

- Predesign No 3 uses the ring geometry with a protruding inner part and a tubular L-shape joint, like Predesign No 1. In this case, also the end-cap has also an internal circular protrusion, which serves in the bolted connection with the ring. As said before, this type of joint possesses a vertical (SLJ) and a horizontal (butt joint) part at the same time, offering larger adhesion surface and loading absorption in two planes. The O-ring is situated in a groove in the interface between the internal circular protrusion of the end-cap and the metal ring, located inside from the bolt, towards the transverse mid-plane of the cylinder. Its position secures the tightness from leakages that may come from either the ring-end-cap interface or the hole of the bolt. The protrusions of the two parts (end-cap and ring), this time, set more limits to the available space.

- Predesign No 4 has a simple metal ring adhesively connected to the cylinder through a tubular SLJ. This time, the protrusion of the end-cap is bolded externally to the metal ring. The O-ring is situated in a groove in the interface between the metal ring and the external circular protrusion of the end-cap, located outside from the bolt, towards the end-cap. Its position is selected to prevent the leakages that may come from ring-end-cap interface or the hole of the bolt. On one hand, an interesting point is that the adhesive is not directly exposed to deep sea conditions, being protected from seawater ageing effects. On the other hand, the ring should be designed thick enough to participate in the bolted connection effectively. Hence, the maximum effective internal diameter of the vessel would be reduced considerably.

- Predesign No 5 is another version of the previous predesign including the advantages of an L-shape joint. The thickness of the ring should meet the dimensional requirements for the bolted connection, reducing the maximum effective internal diameter of the cylinder as well. The O-ring is situated in a groove in the interface between the metal ring and the external circular protrusion of the end-cap, securing the leakages than may come from either the cylinder-end-cap interface or ring-end-cap interface or the hole of the bolt.

A common feature of all cases is the use of countersunk bolts in a blind hole. The restricted access in the pressure vessel after the application of the end-caps makes impossible the use of through-hole bolts with nuts. Another similarity between all the predesigns is the use of O-rings, playing a key role in the sealing of the structure. Its position must secure the tightness.

2.2.3 Selected joint geometries

Moving a step further in our study, it is decided to focus on Predesigns No 3, No 4 and No 5. The reason is that these types of arrangement of the bolted connection, having the bolts on the side surface of the vessel permit the connection of more than one vessel in a row. All joint geometry dimensions not dictated by the design concept (e.g. the external diameter) are initially defined in accordance with good engineering practice. Figure 2.5 presents Predesigns No 3a, No 4a, No 5a, together with two additional joint geometry versions, No 3.1a and No 3.1b, all with their initially defined dimensions. More specifically, the end-cap is designed having 20 mm thickness, the adhesive layer having 1 mm thickness, whereas the ring has various thickness values, dependent on the concept. Regarding, the metal rings, a corner chamfer is added to remove the stress concentrations arising in the sharp corner, leading to an updated version of initial predesigns. An indicative type of countersunk bolt is illustrated on the drawings. The proposed O-ring has a torus diameter of 3.53 mm.

Predesigns No 3a, No 3.1a and No 3.1b are chosen to be modelled in ABAQUS, hereinafter referred to as Design concept No 3a, No 3.1a and No 3.1b respectively.

The first of the three design concepts (3a) presents a number of advantages. Firstly, the chosen geometry offers two different planes of adhesion, offering higher joint strength. Secondly, the thickness of the ring can be smaller in comparison with Predesigns No 4a and No 5a. Consequently, more internal space is available for the accessibility and installation of equipment inside the vessel. Also, a thinner (less stiff) ring attached to the cylinder is more easily deformed by the external pressure and therefore can "follow" the deformation of the cylinder in a better way. As a result, lower stress concentrations are developed in the area where the inner protrusion edge of the ring is bonded to the composite cylinder inner surface (for example, see Point A in predesign 3a in Figure 2.5).

Design concepts 3.1a and 3.1b are similar and superior compared to Design concept No 3a in terms of free space in the interior. The only difference between these two designs is the flat part of the tapered edge of the ring and the cylinder, which is included in design concept No 3.1b. This flat part of the edge protects the tapered side of the composite cylinder from local damages at the sharp edge and contributes to its structural integrity.
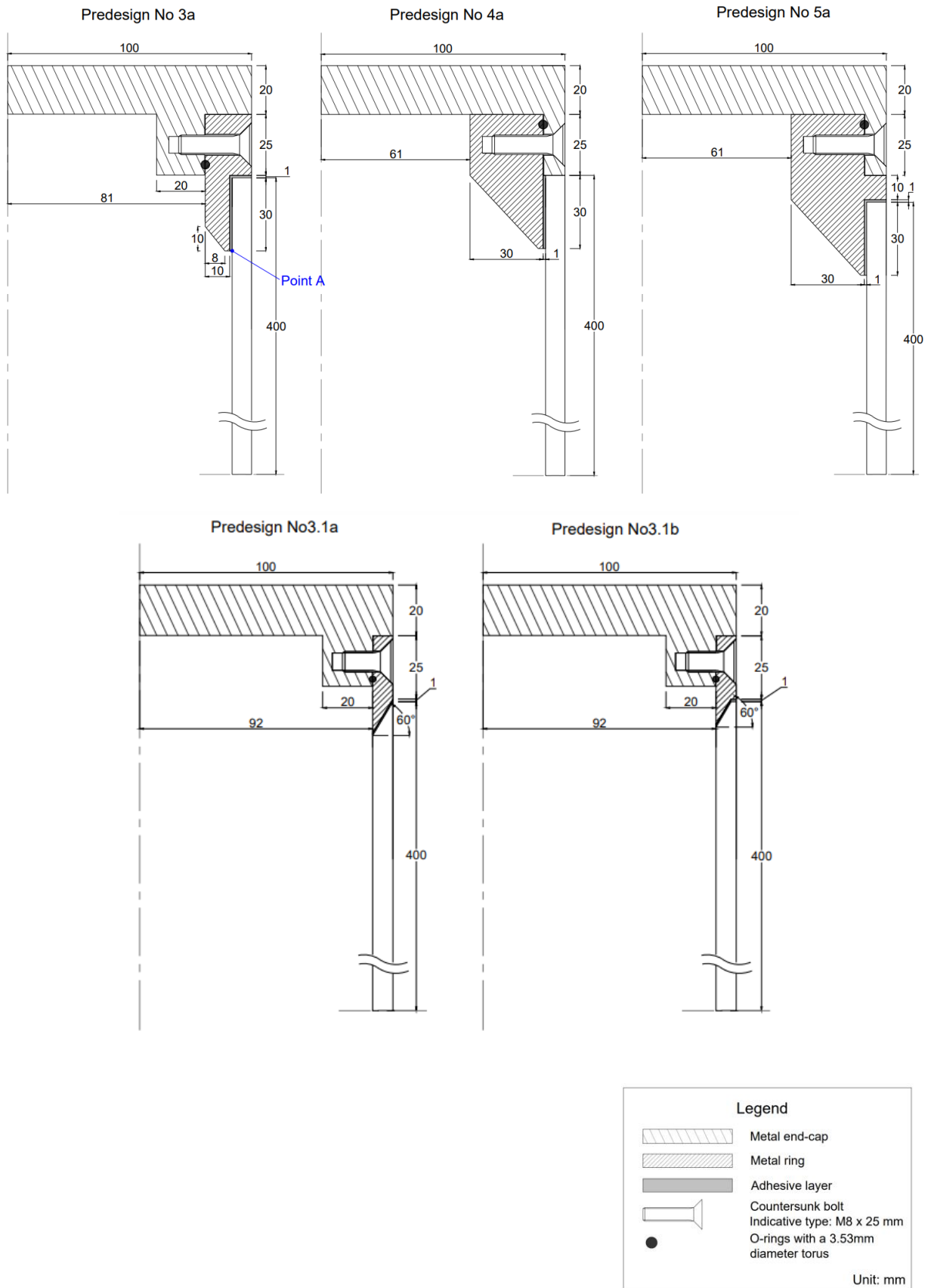
Figure 2.5 Updated and dimensioned version of the sketches of
Predesigns No 3a , No 4a , No 5a , No 3.1a and No 3.1b

2.2.4 Materials

A vital component of performing a successful structural FE analysis is to have an accurate description of the material used. This is achieved by using correct material properties, calculated by standardized experimental procedures. Since corresponding experiments were not part of this work, indicative material properties found in the literature are used.

The metal parts of the pressure vessel are initially specified to be constructed from aluminum and the filament-wound cylinder from fiber reinforced resin. In the study, 7075-T6 aluminum alloy is used for the ring and end-cap since it is a very high strength aluminum and finds use in aerospace, marine and defense applications (https://www.matweb.com/index.aspx). The Al material properties taken into account in the study are presented in Table 2.7.

Regarding the adhesive, two types are examined: a more brittle two-part epoxy adhesive (EA9394 from HYSOL) and a more ductile two-part epoxy adhesive Araldite 420 (Zhan et al., 2016; Al-Mosawe et al., 2016). The adhesive material properties used in the study are presented in Table 2.8.

As for the composite cylinder, two carbon/epoxy systems were considered, a CFRP consisting of 12K T700 carbon fibers in an epoxy resin system and a CFRP consisting of 24K T700 carbon fibers in a Bisphenol A epoxy resin system are used. The former set of material properties was derived from the study of Papadakis et al. (2018) and the latter set was taken from the research work of Moon et al. (2010). Since there is no information regarding the compressive strengths, therefore they were considered equal to the tensile ones. The filament wound composite material properties used in the study are presented in Table 2.9.

Table 2.7 Material properties of metal parts

Material	Elastic Modulus (GPa)	Yield Tensile Strength (MPa)	Poisson's ratio
	E	σ_Y	v
Al7075-T6	72	480	0.3

Table 2.8 Material properties of adhesive

Material	Elastic Modulus (GPa)	Yield Tensile Strength (MPa)	Shear strength (MPa)	Poisson's ratio
	E	σ_Y	S	v
EA9394	4.2	42	35	0.42
Araldite 420	1.5	29	25	0.35

Table 2.9 Material properties of CFRP cylinder

Material	Elastic Modulus (GPa)		Shear Modulus (GPa)		Tensile/ Compressive strength (MPa)			Shear strength (MPa)		Poisson's ratio	
	E_1	$E_2=E_3$	$G_{12}=G_{13}$	G_{23}	X_T	$Y_T=Z_T$	$S_{12}=S_{13}$	S_{23}	$v_{12}=v_{13}$	v_{23}
12K T700 Epoxy	131.17	10.86	4.61	2.305	1060.93	26.08	9.23	4.62	0.280	0.382
24K T700 Epoxy	121.00	8.60	3.35	2.680	2060.00	32.00	45.00	64.00	0.253	0.421

2.2.5 Failure criteria

A continuum mechanics approach is used in this study. A continuum model assumes that the substance of the object completely fills the space it occupies, and the components are modeled as a continuous mass rather than as discrete parts. In the context of this study, the whole pressure vessel is modeled as an entire part, while the different components vary according to their specific material properties. In this type of approach, the maximum values of stress, strain, or strain energy, predicted by the FE analyses, are used in the failure criterion and are compared to the corresponding material allowable values.

Metal parts

The mechanical behavior of the ring and the end-cap is investigated based on the von Mises yield-criterion. It is a criterion for yielding, widely used for metals and other ductile materials. It states that yielding will occur in a body if the components of stress acting on it satisfy the following criterion:

$$\sigma_{von\ mises} = \sqrt{\frac{(\sigma_{xx}-\sigma_{yy})^2 + (\sigma_{yy}-\sigma_{zz})^2 + (\sigma_{zz}-\sigma_{xx})^2 + 6\cdot(\tau_{xy}^2 + \tau_{yz}^2 + \tau_{xz}^2)}{2}} \geq \sigma_Y \rightarrow$$

$$\frac{\sigma_{von\ mises}}{\sigma_Y} \geq 1 \tag{2.3}$$

where σ_{xx}, σ_{yy}, σ_{zz} the stresses in x-axis, in y-axis and in z-axis directions respectively, τ_{xy}, τ_{yz}, τ_{xz} the corresponding shear stresses in a Cartesian coordinate system and σ_Y the yield tensile strength of the material.

ABAQUS software calculates the von Mises stress at all elements integration points and shows the maximum value and its location.

Composite cylinder

In failure analyses of composite structures several approaches have been developed which can be utilized to characterize the initiation and progression of failure. The use of a distinct failure criterion is appropriate to define the stress conditions under which the failure initiates. Failure criteria can be separated into two classes regarding their ability to distinguish among the different failure modes incorporated in the failure of composite materials: independent and interactive (Anyfantis, 2012). The former are easy to apply and give the mode of failure but neglect the effect of stress interactions in the failure mechanisms. The latter perform in the opposite way, as they consider stress interactions and give a more general failure mode. Hashin criterion belongs to interactive criteria, including the following stress components:

Sff, Spp, Snn the stress aligned with the fiber direction (f), perpendicular to the fiber direction (p) and normal to the plane of the ply (p) directions respectively in a local laminate coordinate system

Sfp, Spn, Sfn the shear stress in f-p plane, in p-n plane and in f-n plane respectively in a local laminate coordinate system

The failure criterion incorporated in this study is the Hashin criterion for the full 3D stress state (Hashin, 1980). According to this criterion, criticality of tensile stresses in the fiber direction $S_{ff} > 0$ is predicted with the expression:

$$\left(\frac{S_{ff}}{X_T}\right)^2 + \frac{1}{S_{12}^2}\left(S_{fp}^2 + S_{fn}^2\right) \geq 1 \tag{2.4}$$

Under compressive stresses in the fiber direction $S_{ff} < 0$, failure is predicted with an independent stress condition:

$$-\frac{S_{ff}}{X_C} \geq 1 \tag{2.5}$$

Hashin (1980) explains that matrix mode modelling is more complicated since the failure plane is not identified clearly. In the case of tensile transverse stress $S_{PP} + \sigma_{nn} > 0$ the expression for predicting matrix failure is:

$$\frac{1}{Y_T^2}\left(S_{pp} + S_{nn}\right)^2 + \frac{1}{S_{23}^2}\left(S_{pn}^2 - S_{pp}\cdot S_{nn}\right) + \frac{1}{S_{12}^2}\left(S_{fp}^2 + S_{fn}^2\right) \geq 1 \tag{2.6}$$

When transverse stresses are compressive $S_{pp} + S_{nn} > 0$, the following expression is used:

$$\frac{1}{Y_C}\left[\left(\frac{Y_C}{2\cdot S_{23}}\right)^2 - 1\right]\left(S_{pp} + S_{nn}\right) + \frac{1}{4\cdot S_{23}^2}\left(S_{pp} + S_{nn}\right)^2 + \frac{1}{S_{23}^2}\left(S_{pn}^2 - S_{pp}\cdot\right.$$
$$\left. S_{nn}\right) + \frac{1}{S_{12}^2}\left(S_{fp}^2 + S_{fn}^2\right) \geq 1 \tag{2.7}$$

In addition, the following expression is an out-of-plane version of Hashin that predicts delamination in the thickness direction:

$$\left(\frac{S_{nn}}{Z_i}\right)^2 + \left(\frac{S_{fn}}{S_{13}}\right)^2 + \left(\frac{S_{pn}}{S_{23}}\right)^2 \geq 1 \text{ i=C if } \sigma_{33} < 0 \text{ else i=T.} \tag{2.8}$$

Adhesive layer

In order to attain sufficient confidence in the design of bonded structures, several approaches have been proposed in the literature for adhesive materials failure criteria. These methods could be separated into three categories: stress-based criteria, energy-based criteria, and a combination of the two, the coupled criterion (CC). The principle of the CC is the simultaneous fulfillment of a stress and an energy condition for crack initiation prediction. Figure 2.6 is helpful for a better understanding of this principle. More specifically, the horizontal axis shows the crack length l and the vertical axis shows the energy release rate to fracture toughness ratio in the case of the energy criterion (shown in blue color) and the strength

ratio in the case of stress criterion (shown in red color). For a given imposed loading, if the energy failure criterion is satisfied for a crack length le, it is also satisfied for all crack lengths which are larger than le, as the blue curve shows. The energy condition thus allows determining a lower bound for all the admissible initiation crack lengths. For a too small imposed loading (lower than the initiation loading), the lower bound le for admissible initiation crack length provided by the energy criterion is higher than the upper bound ls provided by the stress condition hence crack initiation is not possible (Figure 2.6 (a)). With increasing loading, ls increases whereas le decreases and the initiation loading and crack length lc can be determined as the loading for which lc = le = ls which ensures that both the stress and the energy conditions are simultaneously fulfilled (Figure 2.6 (b)). In simple terms, coupling both conditions allows determining the initiation loading and crack initiation length.
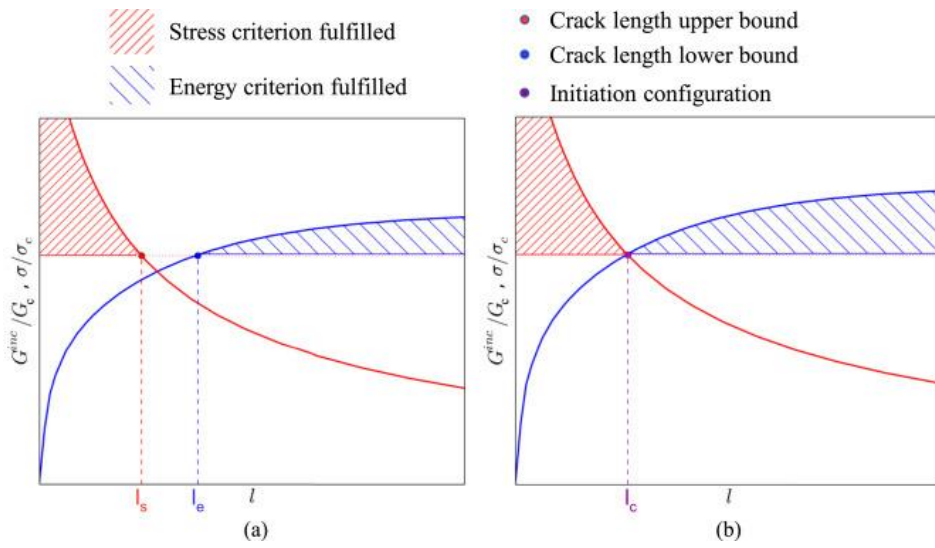

Figure 2.6 Applied stress to strength ratio σ/σ_c and incremental energy release rate to fracture toughness ratio G_{inc}/G_c as a function of the crack length l for a loading (a) lower than the initiation loading, (b) equal to the initiation loading

In this study, the stress criterion condition of the CC is used for the adhesive layer, taking into account a specific value of crack initiation length which is assumed to be equal to 9.5mm. Consequently, wherever stress singularities occur, the stress criterion is calculated at 9.5mm from the singular point of stress concentrations.

In linear static analysis, the criterion applied in the adhesive-metal and the adhesive-composite interfaces is the following quadratic stress criterion, described by Carrere et al. (2015):

$$\sqrt{(\frac{S33(x)}{X_{Ty}})^2 + (\frac{S13(x)}{S})^2} \geq 1 \tag{2.9}$$

where X_{Ty} and S are respectively the peel and out-of-plane shear strengths of the adhesive, respectively, and S33 and S13 are the peel and the out of-plane shear stresses, respectively. The failure criterion applied in the mid-plane of the adhesive is the von Mises yield stress criterion.

In the nonlinear static and nonlinear buckling analysis, the Drucker-Prager pressure-dependent criterion is selected to be applied to the adhesive layer. The reason is that the von Mises yield criterion (initially applied to the adhesive layer under the assumption of elastic,

homogeneous and isotropic behavior) predicts that failure is independent of the hydrostatic stress state (pressure), which means that tensile and compressive stress-strain behaviors are considered equal and are equally treated. Polymers, though, commonly present larger compressive strength. This is a direct result of chains arrangement and deformation micro mechanisms during polymerization, which are dependent on the hydrostatic stress level.

2.2.6 Assumptions

A series of assumptions were made during the numerical analysis of the structural behavior of the components of the pressure vessel.

The material assumptions play a significant role in the whole set-up of the study. The aluminum and the adhesive, used in the linear static analysis, are considered as homogeneous, isotropic, linear elastic materials. In simple terms, it is assumed that they have the same properties at all points and in all directions and the induced response is directly proportional to the applied loads, which do not cause any permanent deformation. The CFRP is considered also as linear elastic but orthotropic material.

The safety factors (SFs) are related with some assumptions also. Since the pressure vessel is subjected to uniform internal and external pressure, the stresses developed in the laminates are considered combined. As it has already been mentioned in Section 2.1, the SF for the composite material is taken equal to 2.24. The same SF value is used for the structural analysis of the aluminum parts and adhesive joint as well. In result, the criteria stated in the previous section predict yielding or failure when the first part of the inequalities becomes equal or higher than $\frac{1}{2.25} = 0.446$. In all figures of this study, the corresponding criterion value will be presented in the y-axis as a function of another magnitude and the maximum permissible criterion limit (0.446) will be represented by a red dotted horizontal line.

Another series of assumptions in terms of manufacturing processes were also made. The manufacture of composite tubes by filament winding generates process-induced stresses. When curing is completed, the tubes are then subjected to ambient conditions which may generate hygrothermal internal stresses which add to the residual manufacturing stresses. When polymer matrix composites are exposed to elevated temperatures and wet environments, they undergo dimensional and stress state changes due to moisture induced swelling and thermal expansion. Such stresses can have a significant effect on the mechanical performance of composite structures by inducing warpage and initiating matrix cracks and delaminations. In the framework of the linear static analysis, all these stresses and flaws are not taken into consideration and the cylinder is considered perfect and stress free before the load application. The joining process is also assumed to be completed under perfect conditions. In particular, the surface preparation is thoroughly completed, leading to prefect quality of adhesion. Moreover, the thickness of adhesive layer is uniform in every point of the adhesion surface without presenting voids and the substrates are joined co-axially.

CHAPTER 3

Numerical modeling: Slice model

The principal aim of this chapter is to develop a Finite Element Model (FEM) of the pressure vessel using ABAQUS that will predict its structural behavior. Problems in which the geometry, loading, boundary conditions and materials are axisymmetric can be solved with an axisymmetric FE model instead of a three dimensional one, economizing computational time. Common tubular structures are usually included in this category. However, the tubular structure under study uses orthotropic composite material, which is axisymmetric only for the winding angles of 0° or 90°. As it has been previously mentioned, these are not feasible options in terms of manufacturing process and the winding angles range from 10-15° to 85°. ABAQUS does not permit these winding patters to be axisymmetrically modeled. Therefore, a 10° slice 3D solid model is created enabling a preliminary structural analysis of the adhesive joint between the ring and the composite cylinder with low computational cost.

3.1 Development of a 10° slice model

The set-up of a proper ABAQUS model constitutes one of the first issues of the study. The dimensions of the whole structure are pretty larger than the ones of the adhesive layer. As a result, the mesh refinement in the area of adhesive joint leads to high number of elements and, hence, a large model. Kim et al., 2001 and Fors, 2010 examined a composite tube adhesively bonded with metal flange. Both of them decided to "cut out" and "submodel" the area of interest as a separate FE model with a much finer mesh, modeling a 50° and a 2° sliced sectors. Based on these references, the FE analysis of Case Study 1 is initially conducted using a 10° slice of the tubular vessel, a model that combines a fine mesh in the location of the adhesive bonding with limited running time. Due to transverse symmetrical geometry, only half of the slice is modeled in this case study, as indicated in Figure 3.1.
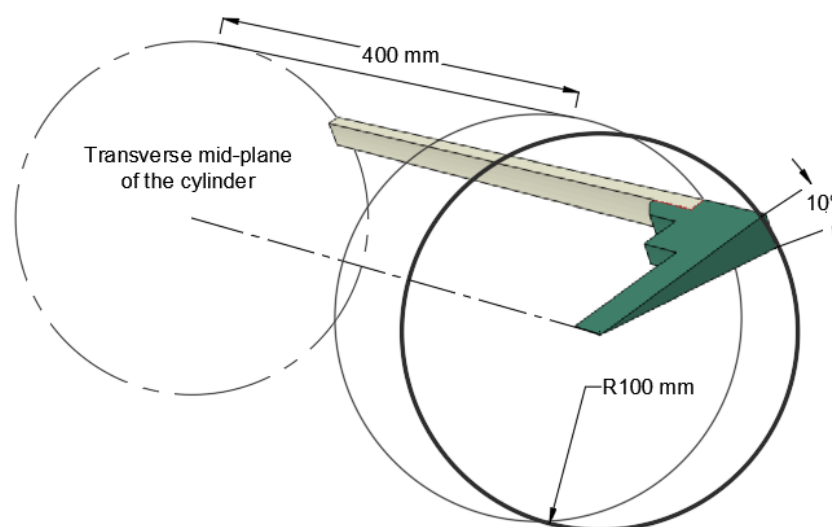

Figure 3.1 10° slice model as a part of the full cylindrical pressure vessel

3.1.1 Geometry, mesh and type of elements

The design concepts (DCs) No 3a, No 3.1a and No 3.1b are modeled as three different sliced models (shown in Figure 3.2). Specifically for each case, the corresponding planar drawing is introduced in ABAQUS model and, afterwards, it is revolved by 10°. The next step is the creation of partitions corresponding to different components. It is noted that continuum modeling is used and the bolt is chosen not to be modeled for the time being. The two metal parts are modelled in contact with each other using the same material (Al 6065-T6), illustrated in Figure 3.2. The cylinder of DC No3a is modeled with 12K T700 epoxy CFRP and the cylinders of DCs No 3.1a and No 3.1b are modeled with 24K T700 epoxy CFRP. The adhesive is modeled with the same properties in all models. The properties used have already been stated in Tables 2.7, 2.8 and 2.9.
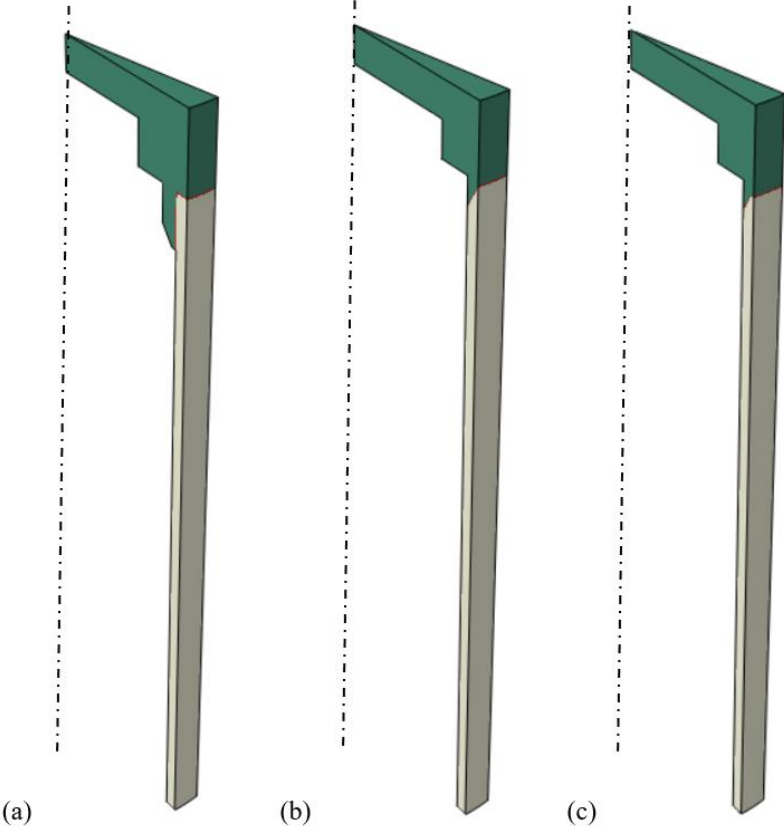

Figure 3.2 Isometric view of the 10° sliced model (Aluminum in green, adhesive in red, CFRP in white) (a) DC No 3a (b) DC No 3.1a (c) DC No 3.1b

The initial stacking sequence is decided to be $[\pm 55]_n$ based on multiple studies concluding that it is the optimum winding angle for filament wound composite tubes under external pressure (Tsouvalis et al., 2000; Arhant et al., 2019). Additionally, it is underlined that a parallel study in the framework of this project investigating the number of layers and the stacking sequence of the composite cylinder in an eigenvalue buckling analysis was conducted. This study indicated a winding pattern of 10 pairs of $[\pm 55]$, 20 layers in total. On one hand, DC No3a is modeled this way. On the other hand, DCs No3.1a and 3.1b are modeled with $[\pm 15/(\pm 55)_9]$ due to the parametric study, analyzed in Section 3.2.3. ABAQUS software offers two methods for the definition of a composite lay-up: the Composite Lay-up and the Composite

Section. The former is an enhanced interface tool for creating ply patterns (making layups symmetric, manipulating the thickness and the number of plies etc.). The latter is created by defining a new section and assigning the corresponding orientation. The main difference of the two methods is that Composite Lay-up applies the defined stacking sequence pattern in one element, contrary to the Composite Section which enables to have at least one element per ply. In the continuum model of this study, using one element across the cylinder thickness could cause difficulties in the mesh refinement of the adhesive layer which is in contact with the cylinder. Therefore, the Composite Section is chosen to model the stacking sequence and assigning the proper material orientation in every ply with reference to the axial direction of the cylinder.

After the creation of the geometry, the material properties and the stacking sequence assignment, the element type has to be defined. Given that the cylinder is relatively thin, as its thickness to diameter ratio is 4%, a reasonable choice is the use of shell elements. However, there are two reasons which make the option of solid elements appropriate. Firstly, the adhesive and the metal parts, which are in contact with the cylinder, are modeled with solid elements. Secondly, using solid elements, the model takes into consideration the stresses developed normally to the plies, important indexes of the delamination effect. Contrary to solid elements, shell elements do not offer a stress and strain profile through thickness. The element type choice poses a dilemma between 20-node and 8-node elements, which is solved given that a model consisted of 8-node elements needs significantly less computational time than a model using 20-node elements. Finally, the element type used in all models of this chapter is the 8-node structural 3D solid element C3D8.
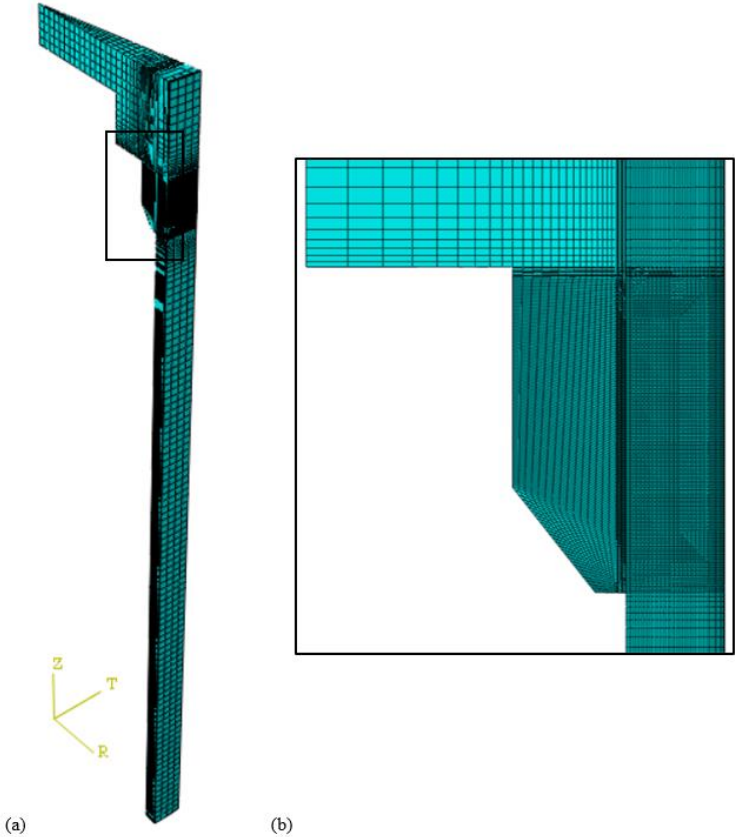

Figure 3.3 (a) Isometric view of the model of DC No 3a (b) Detailed side view of the adhesive joint
(10 elements per adhesive thickness and 2 elements per ply)

The mesh definition and creation is a demanding part of the study due to the complex geometry of the structure. Aiming at the study of the stress distribution in the area of the adhesive joint, a fine mesh is necessary. As it is presented in Figure 3.3, a gradual mesh has been applied in the area around the joint starting from the mesh size of the elements of adhesive layer and ending in larger elements. A mesh convergence study (MCS) regarding the DC No3a, was conducted. The results are presented in Section 3.2.1. It focuses in the area of the adhesive joint, resulting in selecting 10 elements across the thickness of the adhesive layer and 2 elements per cylinder' s ply. This leads to a model of 64148 elements. The elements of the adhesive layer have dimensions equal to 0.10 mm and 0.20 mm in the axial and the circumferential dire. It is underlined that the creation of cubic elements was not possible. The great size differences between the components in combination with the mesh consistency from one component to the other lead to elements with high aspect ratio. The rest of the models mentioned in this chapter are designed after taking into account and adapting the conclusions of this MCS in the corresponding geometry.

3.1.2 Loading conditions

The pressure vessel is subjected to external hydrostatic pressure of 40 bar or 4 MPa while the internal pressure is equal to 1 bar or 0.1 MPa. In the ABAQUS model, the internal pressure is applied to the internal surface and the external pressure to the external surface, respectively as shown in Figure 3.4. The same loading conditions are applied in all models.
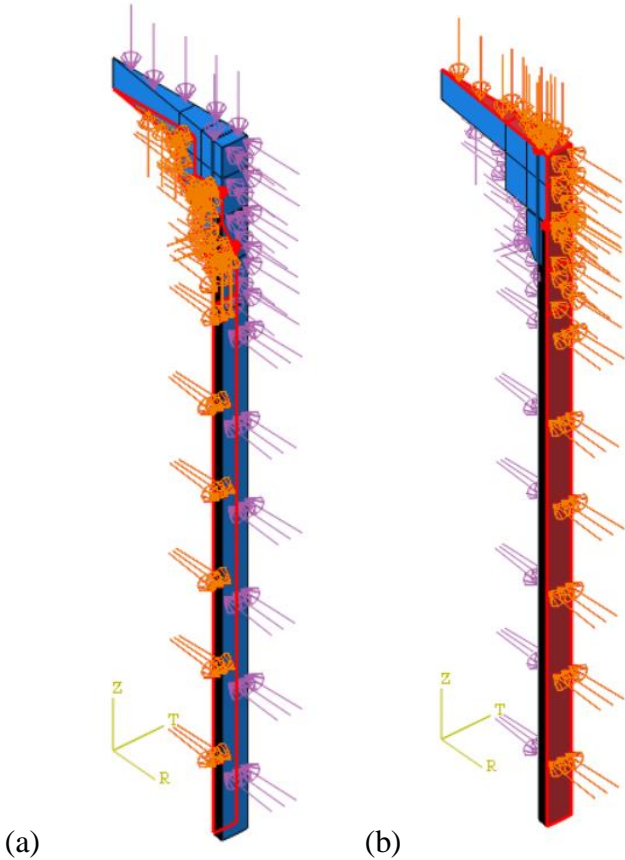

(a)   (b)

Figure 3.4 Application of the loading conditions on slice model
(a)0.1 MPa internal pressure, (b) 4 MPa external pressure

3.1.3 Boundary conditions

The next task is the definition of the boundary conditions (BC). In real-life, the structure will be free to flow underwater without boundary conditions thanks to uniform external pressure, buoyancy and gravity. In FE modelling, though, the boundary conditions are necessary even when the loading applied to the body seems symmetric and equilibrated. In fact, setting the proper BC, rigid body motion, caused by numerical singularities, is constrained. The chosen BC should define the problem sufficiently and be as minimal as possible in order to represent the realistic conditions. They are applied using a cylindrical coordinate system, where the radial (r), the circumferential (θ) and the axial (z) directions are illustrated in Figure 3.5 (a). A symmetric boundary is employed on the surface where the transverse symmetric plane of the cylinder is. This means that fixed axial direction (U3=0) and fixed rotations around the radial and circumferential axes (UR1=UR2=0) are applied. In addition, the circumferential direction of the two side surfaces of the slice is fixed (U2=0), representing the rest of the cylinder that would be the extension of these two sides, as illustrated in Figure 3.5 (b). The same BC are applied in all models mentioned in this chapter.
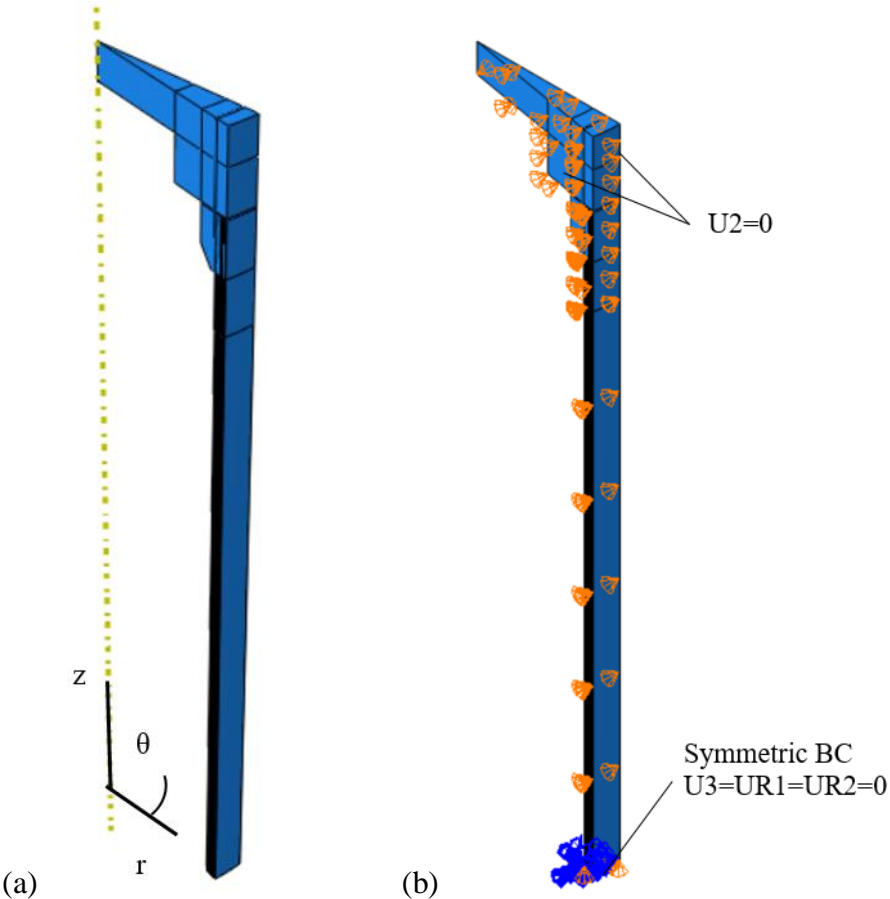

Figure 3.5 Application of the boundary conditions on slice model using cylindrical coordinates

(a)cylindrical coordinate system, (b) BC

3.1.4 Type of analysis

Linear static and nonlinear static analyses are performed in order to examine the structural behavior of the models, especially, in the area of the joint. The difference between these two types of analysis is visualized in Figure 3.6.

On one hand, a linear static analysis is an analysis where a linear relation holds between applied forces and displacements. In practice, this is applicable to structural problems where stresses remain in the linear elastic range. In a linear static analysis the model's stiffness matrix is constant, and the solving process is relatively short compared to a nonlinear analysis of the same model. Therefore, for a first estimate, the linear static analysis often precedes a full nonlinear analysis.

On the other hand, the nonlinear static analysis is an analysis where a nonlinear relation holds between applied forces and displacements. Nonlinear effects can originate from geometrical nonlinearities (i.e. large deformations), material nonlinearities (i.e. elasto-plastic material), boundary conditions nonlinearities and contact. The performance of nonlinear static analysis for this case study is chosen in order to examine whether the deformations of the adhesive layer become larger by applying the load incrementally. During the non-linear analysis, the adhesive layer is modeled as elastic-plastic material with strain hardening behavior. ABAQUS software offers a built-in linear Drucker-Prager criterion which determines whether the material undergoes plastic deformation, taking into account the pressure effect as well as nonlinearities. In order to define this criterion, the stress–strain behavior of the adhesive in tension, in compression or in shear, the angle of friction and the dilation angle of the adhesive are required. The stress-strain curve of EA9394 adhesive in tension taken into account in the present modelling, is provided by tensile tests, carried out on dog bone shaped bulk adhesive specimens by Zhan et al., 2016. The angle of friction, which connects with a linear relation the pressure with the von Mises equivalent stress, for adhesives with the same properties as EA9394 equals to 45° (de Morais et al., 2007). Additionally, the dilation angle which is related to the volume change of the material, is set equal to zero assuming that there is no volume change during plastic deformation.
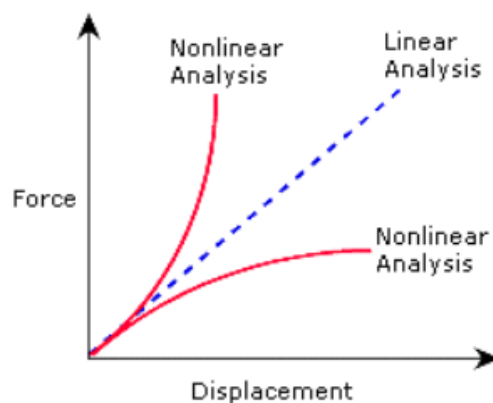

Figure 3.6 Qualitative diagram of linear and nonlinear analysis

3.2 Results of the slice model

This section presents the relevant results that were the outcome of the analysis methods described in the previous sections considering the design concepts (DCs) No 3a, No 3.1a and No 3.1b slice models.

3.2.1 Mesh Convergence Study

The mesh convergence study (MCS) of DC No3a was one of the first steps of the work in order to determine the appropriate mesh refinement, taking into consideration two parameters: the number of elements across the thickness of the adhesive and the number of elements per cylinder's ply. It is reminded that the thickness of the adhesive layer equal to 1mm whereas the composite cylinder has 20 plies (every ply is 0.4 mm thick).

Four different mesh patterns are checked. The first mesh consists of 6 elements across the adhesive thickness and 1 element per cylinder ply, with adhesive elements dimensions being 0.16 x 0.40 mm. The second mesh consists of 10 elements across the adhesive thickness and 1 element per cylinder ply, with adhesive elements dimensions being 0.10 x 0.40 mm. The third mesh consists of 14 elements across the adhesive thickness and 1 element per cylinder ply, with adhesive elements dimensions being 0.07 x 0.40 mm. The fourth mesh consists of 10 elements across the adhesive thickness and 2 elements per cylinder ply, with adhesive elements dimensions being 0.10 x 0.20 mm. All the mesh patterns present a gradual mesh starting from 0.8 mm element length (regarding elements located in the end of adhesive joint) and ending in 4 mm element length (regarding elements located 30mm away from the end of adhesive joint, towards the transverse mid-plane of the cylinder). The rest of the cylinder is modeled with elements of 4 mm length.

The comparison of the results considers four representative nodes of the vessel, which are visualized in Figure 3.7. Node 1 is situated at the mid-length of the half cylinder. Node 2 is situated at the central point of the end-cap. Node 3 is situated in the adhesive-composite interface at the end of the joint. Because of the mismatch of properties between substrate and adhesive, a singular stress field especially near the edge of the adhesive layer is expected. Node 4 is situated at the internal corner of the end-cap where high Von-Mises stresses are developed.
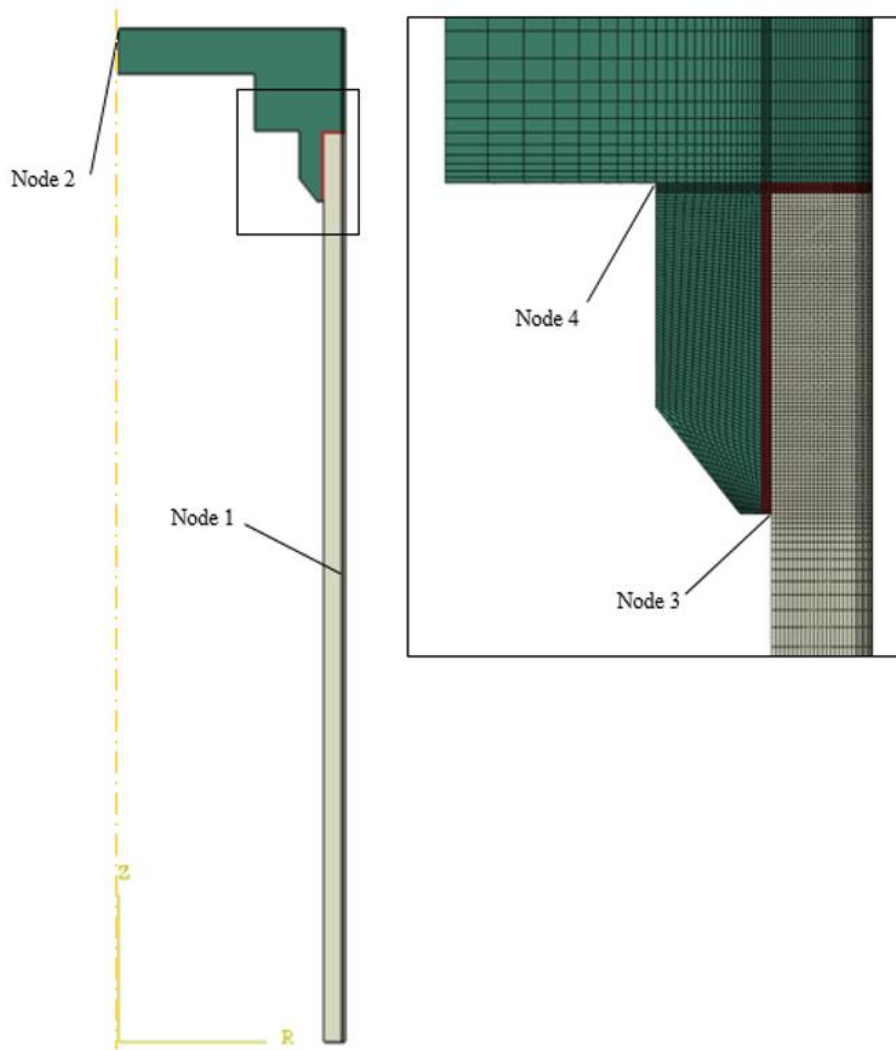
Figure 3.7 Location of the nodes used in MCS

Keeping in mind that the stress singularities and stress concentrations are intensified using finer mesh, the first results (enlisted in Table 3.1) concern radial (U1) and axial (U3) displacements. The difference between the finer (10/adh-2/ply) and the coarser (6/adh-1/ply) mesh is 0.73% concerning the radial displacement of Node 1, 0.45% concerning the axial and negligible concerning the radial displacement of Node 3 and 0.34% concerning the axial displacement of Node 4.

Table 3.1 Mesh convergence study –displacements comparison [in mm]

	Node 1 (Composite cylinder)	Node 3 (Adhesive)		Node 2 (End-cap)
Mesh description	U1	U1	U3	U3
6/adh-1/ply	-0.05716	-0.005047	-0.12000	-0.180423
10/adh-1/ply	-0.05716	-0.005051	-0.11999	-0.180425
14/adh-1/ply	-0.05716	-0.005052	-0.11999	-0.180425
10/adh-2/ply	-0.05758	-0.005051	-0.12054	-0.181037

Apart from displacements, the stresses developed in representative points of the vessel are compared in Table 3.2. The stresses chosen to be compared are:

- in the composite cylinder: stress aligned with the fiber direction (Sff), perpendicular to fiber direction (Spp), normal to the ply (Snn) and the in-ply shear stress (Sfp)

- in the adhesive the stress in radial direction (S11)

- in the metal end-cap the von Mises stress (Svm).

The maximum difference between the finer and the coarser mesh is up to 6% concerning the stresses developed in Node 1, approximately 30% concerning the peel stress developed in Node 3 and 5% concerning the Von Mises stress developed in Node 2. The percentage of difference regarding the adhesive is relatively high and, at a first glance, the convergence is not reached.

Table 3.2 Mesh convergence study- stresses comparison [in MPa]

Mesh description	Node 1 (Composite cylinder)				Node 3 (Adhesive)	Node 4 (End-cap)
	Sff	Spp	Snn	Sfp	S11	Svm
6/adh-1/ply	-51.89	-8.00	-3.89	1.40	-32.80	88.79
10/adh-1/ply	-51.89	-8.00	-3.89	1.40	-36.87	93.24
14/adh-1/ply	-51.89	-8.00	-3.89	1.40	-38.91	95.39
10/adh-2/ply	-52.26	-8.08	-3.98	1.31	-46.98	93.35

However, it is advised not to jump into conclusions based on a single node, located in a stress concentration zone. Therefore, the stress distribution along the vertical adhesive layer interface with the composite cylinder is also examined in order to check whether the stress concentration is localized and affects only the stress results near the edge. Figure 3.8 shows the path which is used for plotting the stress distribution for the different mesh patterns. It is situated in the axial adhesive-composite interface and starts from the edge where the higher stresses are developed. Figure 3.9 illustrates the percentage of difference between the finer (10/adh-2/ply) and the coarser (6/adh-1/ply) mesh along the path. It is clear that the mesh patterns converge everywhere but in the stress concentration area at the end of the adhesive joint. Considering the results, the aspect ratio of elements and the duration of the solution, it is decided to continue the study using the mesh 10/adh-2/ply.
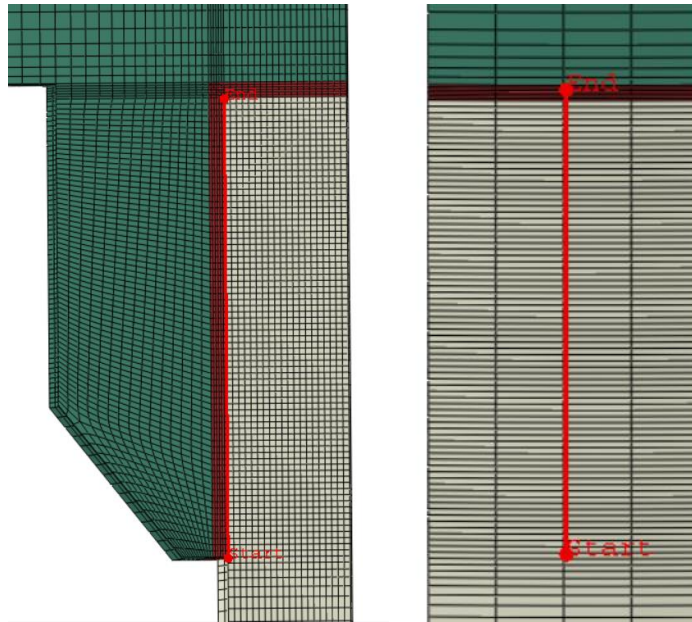
Figure 3.8 Path in the adhesive-composite interface of the vertical part from side and back view
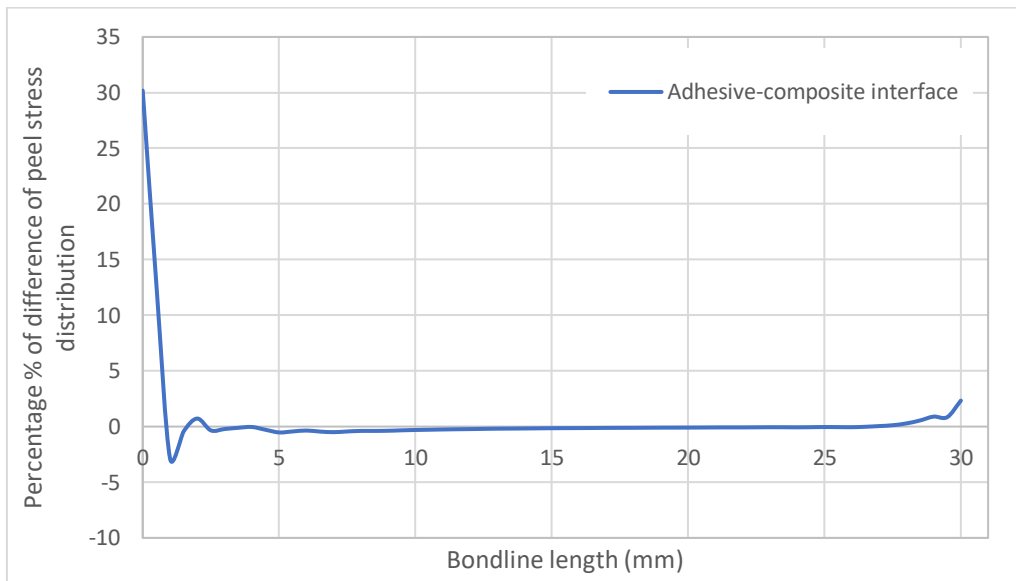

Figure 3.9 Percentage % of difference of peel stress distribution between the finer and the coarser mesh along Path

3.2.2 Analysis of results

The post-processing of the model which consists in obtaining all the results can lead to useful conclusions. The results of DC No3a model are discussed starting from the linear static analysis and moving on to the nonlinear static analysis. Afterwards, the results of DC No 3.1a and No 3.1b in linear static analysis are described. The objective is to examine if the components yield or fail under the given loading and boundary conditions and if, yes, which is the first one to exceed its strength limit.

3.2.2.1 Results of linear static analysis of design concept No3a

The validity of the solution can firstly be checked by plotting the deformed shape of the model during the procedure along with the displacements field that is created. Figure 3.10 visualizes the radial (U1) and axial (U3) displacement results. The maximum radial displacement (inwards) is observed on the cylinder below the joint area, since at this point, the cylinder presents lower bending stiffness compared to the metal end-cap as well as the components in the joint area. The maximum axial displacement is expected to be in the central area of the end-cap as the larger unsupported length in the radial direction is presented at this area. Indeed, Figure 3.10 (a) proves that the center of the end-cap is displaced more than every other point of the structure. As for the rotations, it is highlighted that they are negligible due to the symmetric boundary conditions.
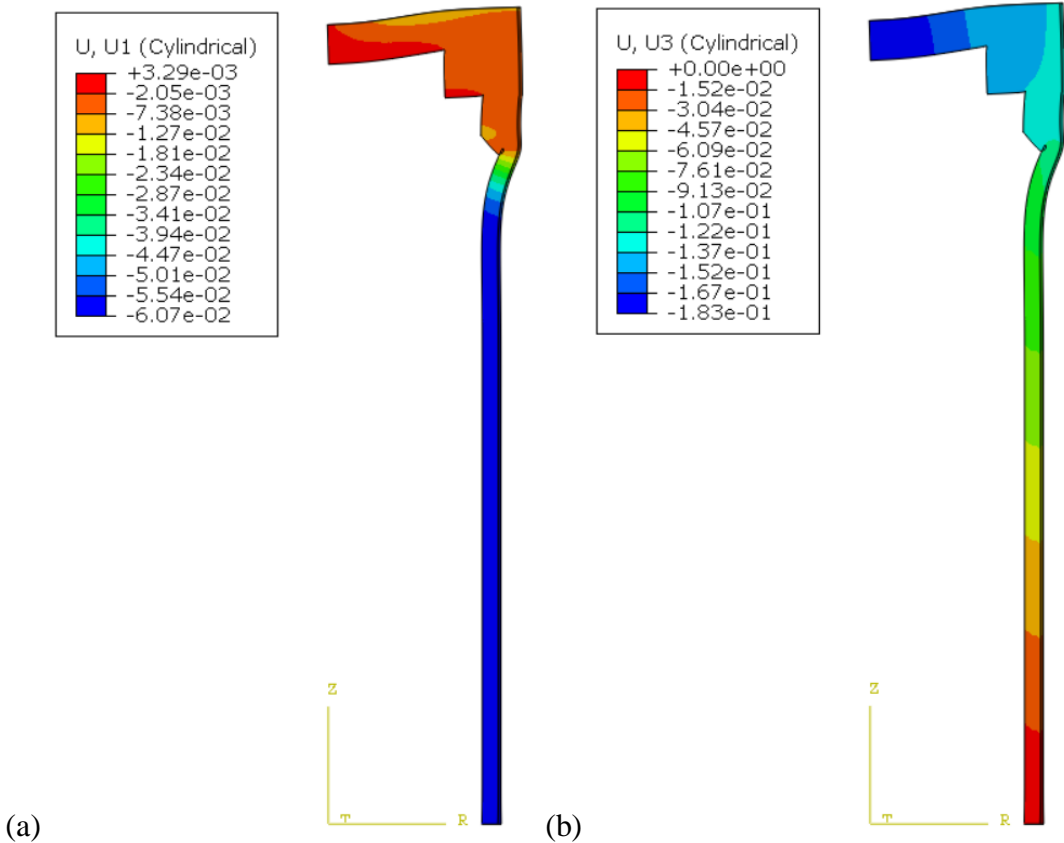

(a)   (b)

Figure 3.10 Contour plot of (a) radial displacement and (b) axial displacement distribution
Deformed shape (deformation scale factor: 200)

The next step of the study is the stress field of the different parts in order to verify whether the yield or failure criteria are satisfied.

Metal part

The metal part of the model, including the end-cap and the ring, presents stress concentrations at the internal corners, where abrupt geometric changes occur. The maximum von Mises stress value is 93.4 MPa at the corner pointed out in red in Figure 3.11. This stress value is probably overestimated since in real-life the edges are constructed with fillet radius in order for the stress concentrations to be avoided. Applying the von Mises criterion considering σ_Y=480 MPa as indicated in Table 2.7, the criterion limit is calculated equal to 0.19, which is safely lower than maximum permissible criterion value of 0.45.
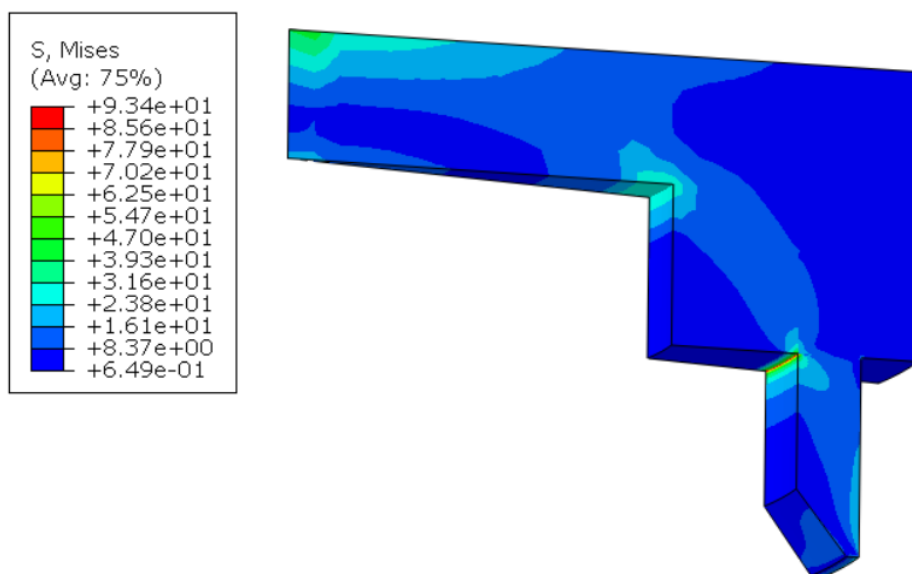

Figure 3.11 Contour plot of Von Mises stress distribution of the metal part
Undeformed shape

Adhesive layer

The adhesive layer of the pressure vessel, as it has repeatedly been mentioned, has L-shape. This means that it does not form neither a pure SLJ nor a pure butt joint but a combination of them two. The part which is parallel to the axial direction will be hereafter mentioned to as axial part of the adhesive, whereas the part which extends in the radial direction will be hereafter mentioned to as radial part of the adhesive. Using a cylindrical coordinate system, the radial stress (S11) developed in the axial part correspond to the peel stress of this part whereas the axial stress (S33) developed in the radial part correspond to the peel stress of this part. The shear stress in both parts of the adhesive correspond to shear stress S13. Figure 3.12 shows that the stress field is more intense at the end of the adhesive joint, where the compressive stresses reach their maximum. However, it is reminded that according to Section 2.2.5, the point of interest is at a distance of 9.5 mm from the lower edge where the criterion is applied.
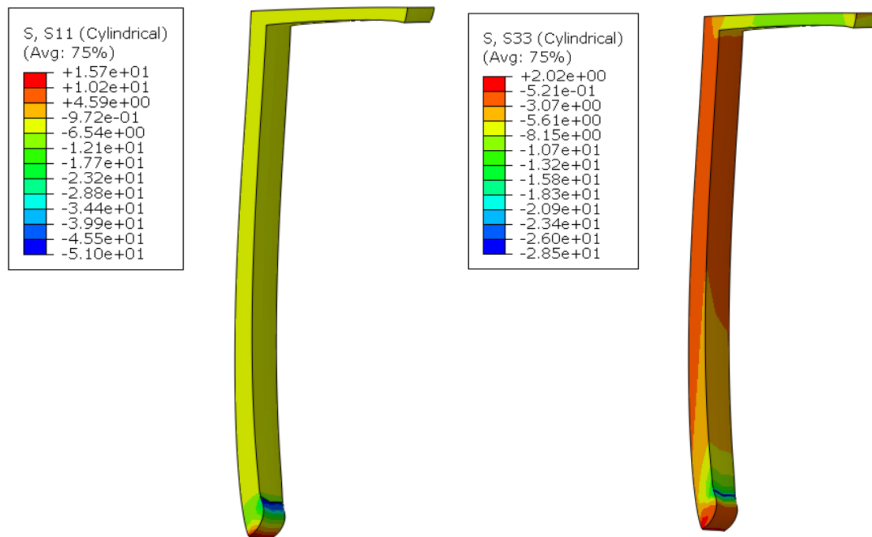
Figure 3.12 Contour plot of (a) radial stress and (b) axial stress distribution

Deformed shape (deformation scale factor: 200)

The quadratic criterion along the interfaces of the adhesive is plotted using four paths (Figure 3.13). The paths are located in the mid-width of the slice (as it is shown in the back view) and, more specifically in: axial metal-adhesive interface (continuous orange line), axial adhesive-composite interface (continuous yellow line), radial metal-adhesive interface (dashed orange line), and radial adhesive-composite interface (dashed yellow line). In addition, the Von Mises criterion is plotted using two paths which are also located in the mid-width of the slice in the axial and radial adhesive mid-planes. Figures 3.14 shows the quadratic criterion values in the metal-adhesive interface and in the adhesive composite interface as well as the von Mises criterion values along the mid-plane of the axial part of the adhesive. The initiation length is taken into consideration and the criterion values at that point are calculated lower than the required upper limit (0.45). Figure 3.15 illustrates the quadratic criterion values in the metal-adhesive interface and in the adhesive composite interface as well as the von Mises criterion values along the mid-plane of the radial part of the adhesive. The criteria values are lower than the required upper limit (0.45) along the whole radial part.
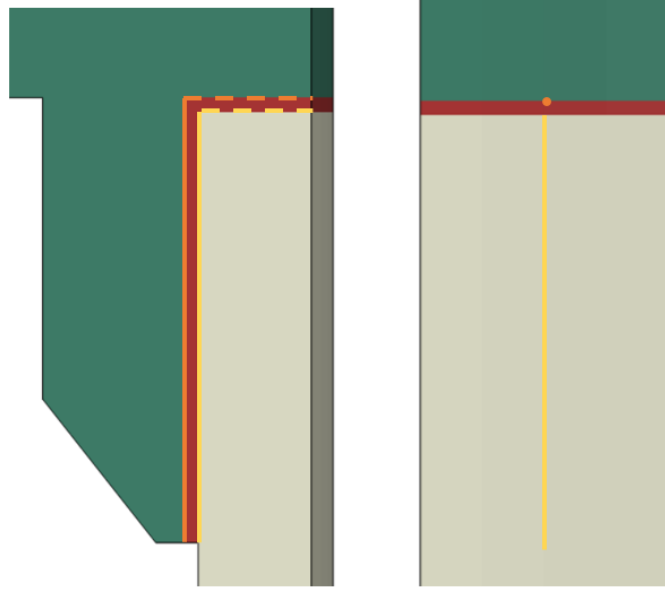
Figure 3.13 Paths in the interfaces of the adhesive layer from side and back view (Metal-adhesive Int.: Orange, Adhesive-composite Int.: Yellow, Axial part: Continuous line, Radial part: Dashed line)
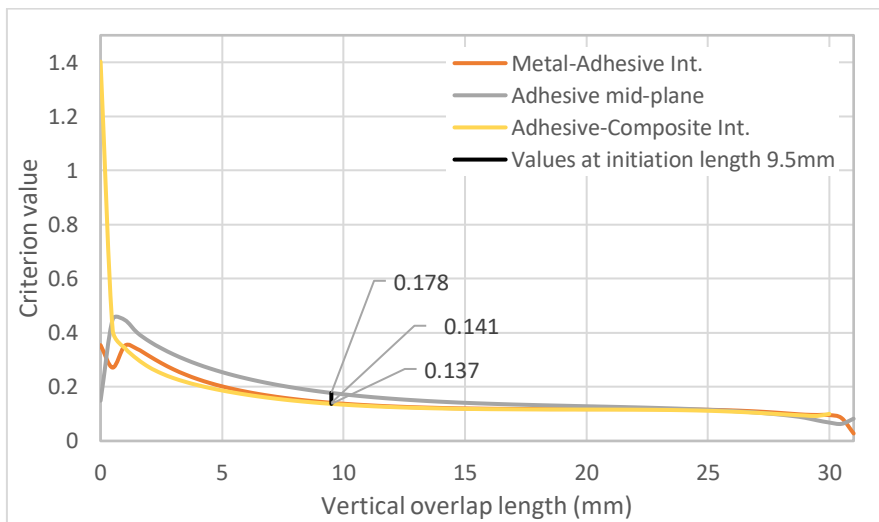

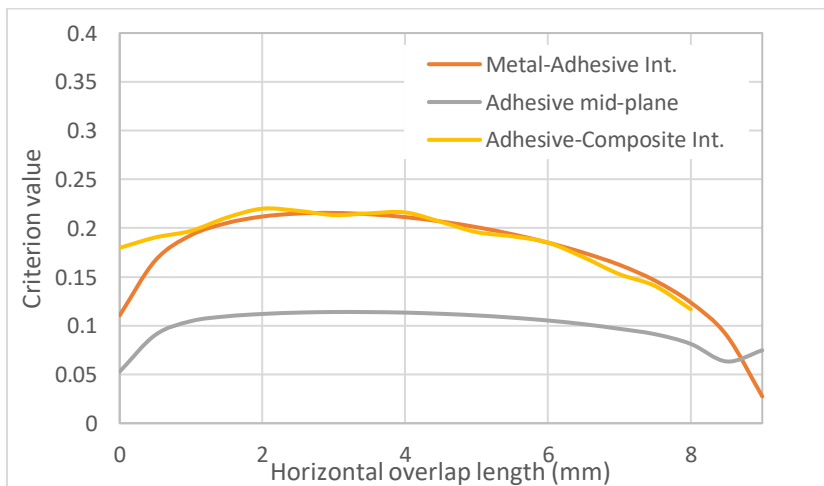**Figure 3.14** Quadratic and von Mises criterion values along the axial part of adhesive

Figure 3.15 Quadratic and von Mises criterion values along the radial part of adhesive

Composite cylinder

Hashin criterion is applied in order to assess the structural behavior of the cylinder. It is underlined that ABAQUS software offers a built-in Hashin criterion applicable only to 2D plane stress, shell, continuum shell and membrane elements according to ABAQUS User Manual. Given that the model of the study is created by 3D solid elements, the manual introduction of the criterion is necessary. ABAQUS software offers a tool called "Create from Field Output" enabling the user to introduce stress or displacement results in mathematical relations and, therefore, to create their "own" field output. Taking advantage of this tool, the stresses developed in the fiber direction (Sff), perpendicular to the fiber direction (Spp), normal to the ply (Snn) and the corresponding shear stresses (Sfp, Sfn, Spn) and the equations stated in Section 2.2.5 are introduced in order to calculate the 3D Hashin criteria values. The results shown in Figure 3.16, 3.17 and 3.18 come from the criterion regarding the compressive stresses. It is observed that the higher values of Fiber, Matrix and Out of plane Hashin are reached in Ply 1, which is in contact with the adhesive layer. The values of Matrix and Out of plane Hashin criteria exceed by far the maximum permissible criterion value (0.45). Specifically, the prone to failure area is situated at the end of joint and a few millimeters below. An interesting and important observation is the asymmetric field of Hashin criterion values in Figures 3.16, 3.17 and 3.18. This asymmetry with respect to the longitudinal mid-plane of the sliced model stems from a corresponding asymmetric stress field, fact that is alarming.
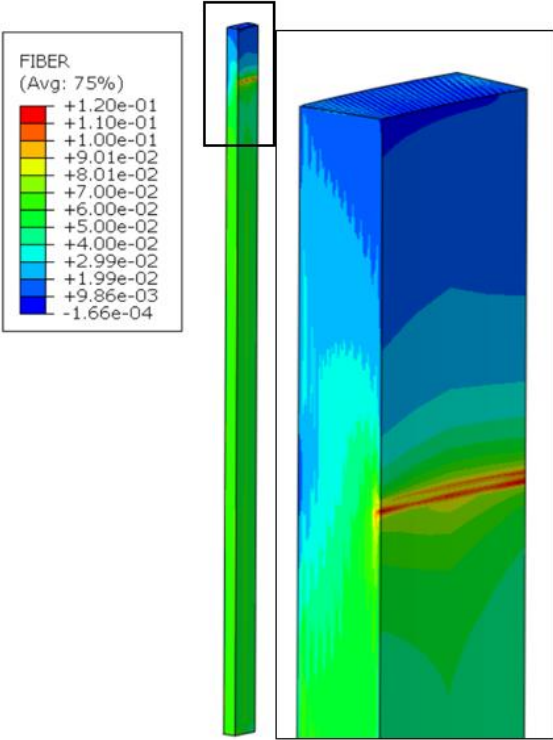

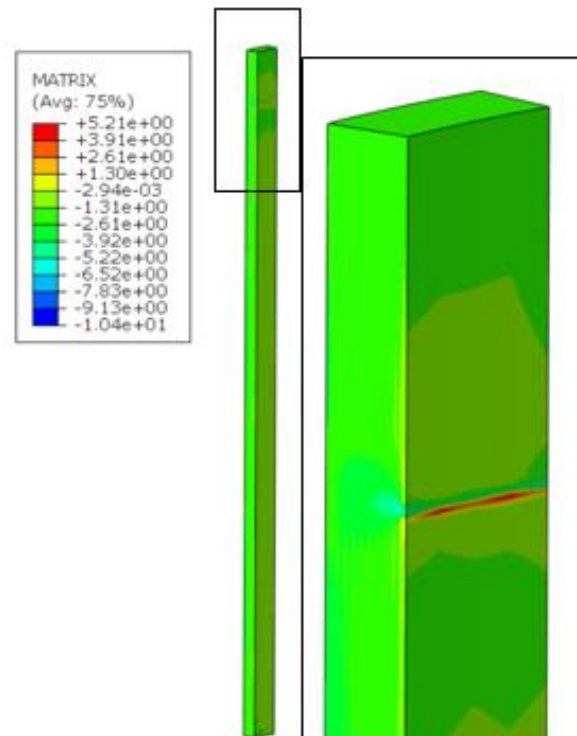**Figure 3.16** Contour plot of Fiber Hashin distribution
Undeformed shape

Figure 3.17 Contour plot of Matrix Hashin distribution
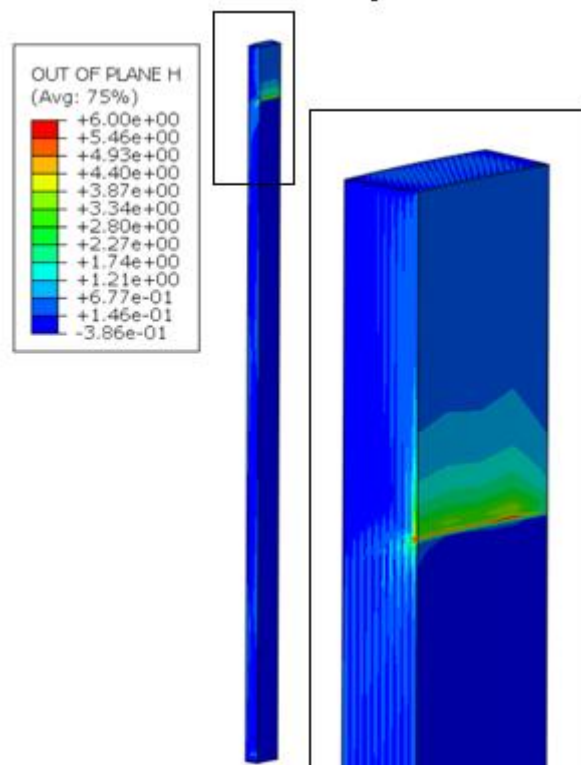Undeformed shape

Figure 3.18 Contour plot of Out of plane Hashin distribution
Undeformed shape

3.2.2.2 Results of nonlinear static analysis of design concept No 3a

Geometrically linear analyses were previously performed assuming linear elastic isotropic behaviour for adhesive. In a second stage, the adhesive layer is modeled as elastic-plastic material, as described in section 2.2.5. A nonlinear analysis is conducted with the parameters presented in Table 3.3. The results regarding the composite cylinder and the metal part have no difference with the results of the linear analysis. As for the adhesive, the AC yield output (it stands for "actively yielding") is used which provides a yes/no flag telling if the material is currently yielding or not, given that the adhesive has been modeled as elastic-plastic material. The AC yield output shows that it remains in the elastic region under the given loading conditions.

Table 3.3 Nonlinear buckling analysis parameters

Nonlinear geometry option: activated			
Max No of increments	Size of increments		
	Initial	Min	Max
10	0.01	0.001	0.01

3.2.2.3 Parametric study of design concept No 3a

In this section, the effect of geometry, overlap length, adhesive thickness, material properties as well as stacking sequence variation of Design concept 3a are investigated. The objective is the reduction of the high stresses developed in the cylinder, at the location of the edge of adhesive joint.

Geometry of the metal part

The parametric study starts with different geometric versions of the metal part. Having observed the "weak" point of the cylinder in terms of stresses, the idea is the reduction of the radial stiffness of the metal part near the area of this weak point. This way it resists less to the inwards displacement of the composite cylinder at this point. The first version (i) includes the thickness of protrusion of the end-cap reduced by half. The second version (ii) includes the thickness of the metal ring reduced by half. The third version (iii) includes both -previously mentioned- thicknesses reduced by half. The fourth version (iv) includes a sharper chamfer of the metal ring. Figure 3.19 shows an overview of the different metal parts geometric versions.
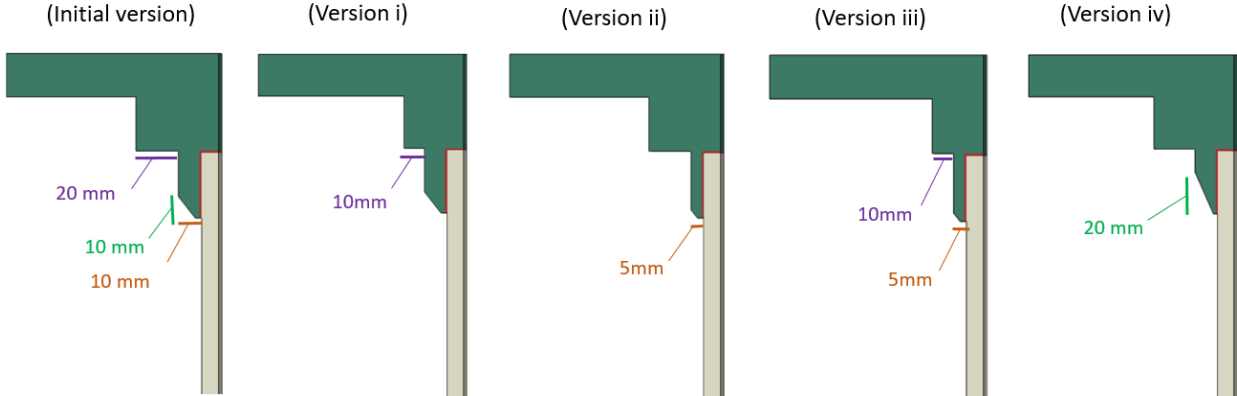

Figure 3.19 Geometric versions of the metal parts

The two following figures offer the opportunity to compare the maximum values of the applied criteria for the different geometric configurations of the metal parts. The von Mises criterion is applied in the metal part and in the mid-plane of the adhesive layer, the quadratic criterion is applied in the interfaces of the adhesive layer with its neighboring components and the Hashin criterion is applied in the composite cylinder. Figure 3.20 concerns the metal parts and the adhesive layer taking into consideration the initiation length in the axial part. It is noted that the governing criterion in the interfaces is the one applied in the axial part contrary to the governing criterion in the mid-plane which is the one applied in the radial part. It is observed that the adhesive layer is on the safe side without significant differences among the presented versions. The stresses on the metal part, however, vary from version to version. The thicker the protrusion and the thinner the ring are, the higher the stress concentrations at the edge become, remaining lower than the required criterion limit though. Figure 3.21 concerns the composite cylinder, showing the values of Matrix and Out of plane Hashin exceeding considerably the required criterion limit, fact that predicts high possibility of matrix failure or delamination. Finally, the geometric versions (iii) and (ii) provide the best results.

	Initial	i	ii	iii	iv
von Mises metal	0.19	0.15	0.33	0.28	0.20
Quadratic met-adh int.	0.22	0.23	0.21	0.23	0.21
von Mises adh. mid-plane	0.19	0.19	0.19	0.17	0.20
Quadratic adh-comp int.	0.22	0.24	0.22	0.24	0.22
Criterion upper limit	0.45	0.45	0.45	0.45	0.45
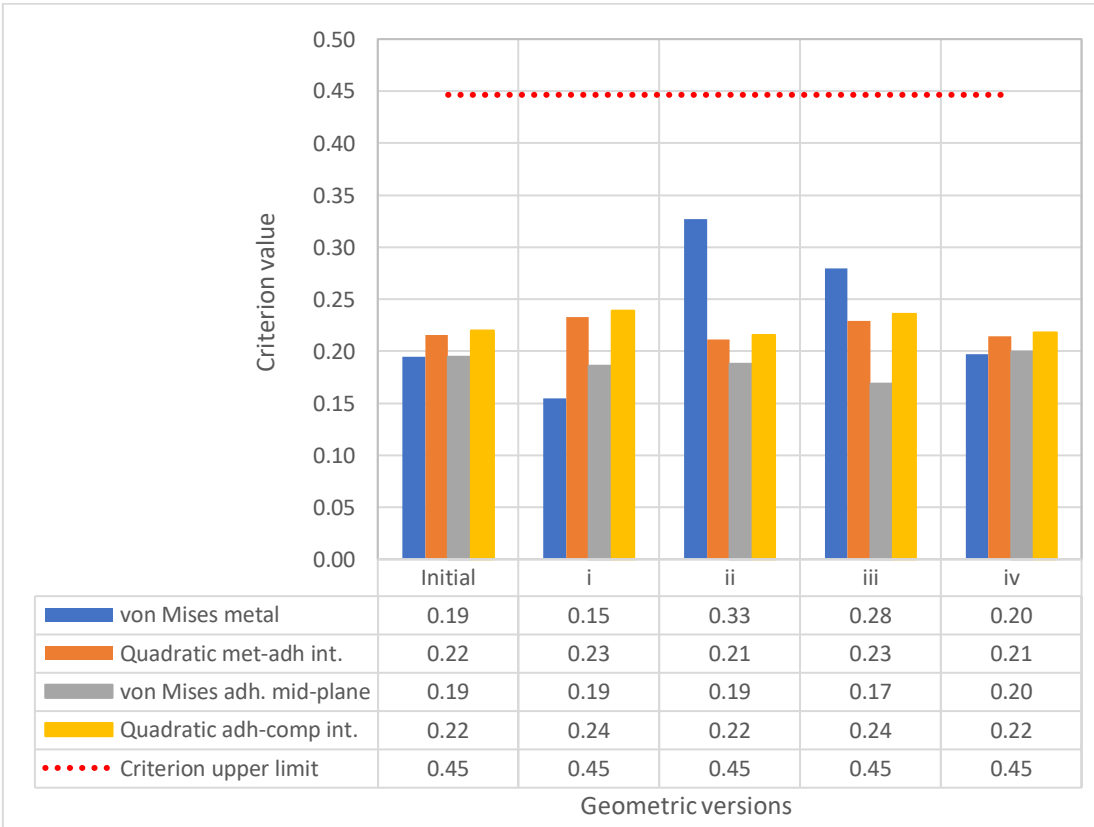
Figure 3.20 Criteria values of different geometric versions (Metal part & adhesive layer)

	Initial	i	ii	iii	iv
Fiber Hashin	0.12	0.12	0.11	0.11	0.12
Matrix Hashin	5.21	4.75	2.31	1.99	4.88
Out of plane Hashin	6.00	5.74	4.43	4.26	5.92
Criterion upper limit	0.45	0.45	0.45	0.45	0.45
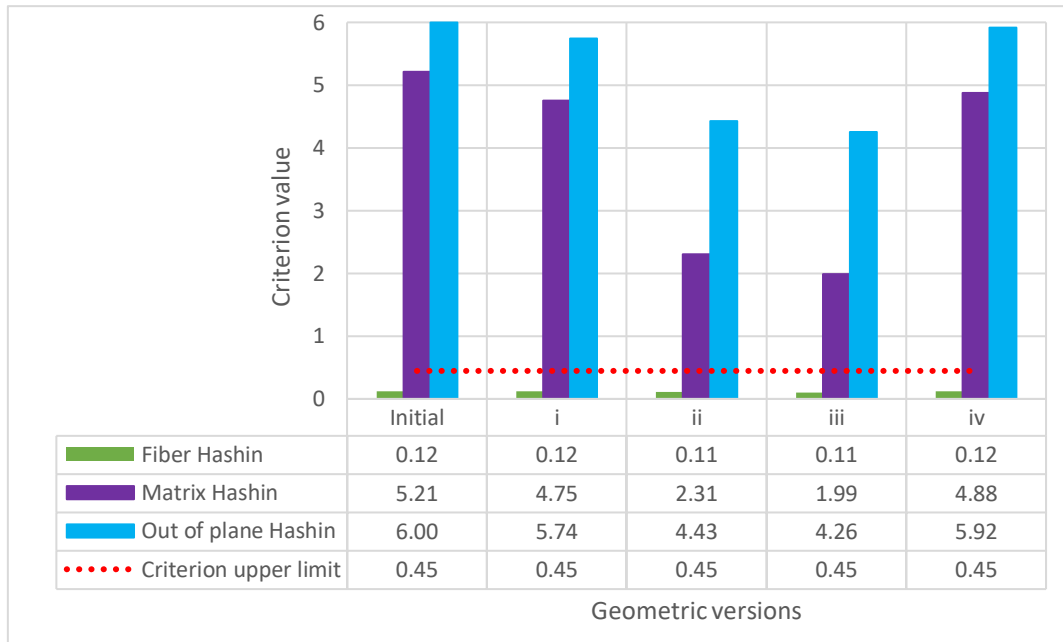
Figure 3.21 Criteria values of different geometric versions (Composite cylinder)

Ring protrusion length

The parametric study continues with ring protrusion length variation. It is noted that the ring protrusion length equals to axial adhesion bondline length. The effect of 33.3% more and 33.3% less length than the initial axial part length (30mm) is examined (Figure 3.22). The radial part length is necessarily constant and equal to cylinder thickness. As a rule, the larger the surface of adhesion is, the stronger the joint becomes.
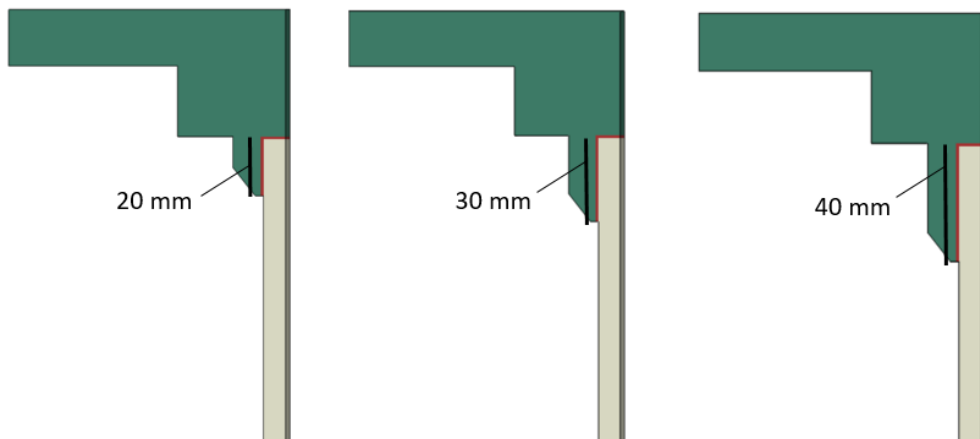
Figure 3.22 Ring protrusion length variation

	20	30	40
von Mises metal	0.15	0.19	0.22
Quadratic met-adh int.	0.29	0.22	0.17
von Mises adh. mid-plane	0.20	0.19	0.17
Quadratic adh-comp int.	0.30	0.22	0.17
Criterion upper limit	0.45	0.45	0.45

Ring protrusion length (mm)
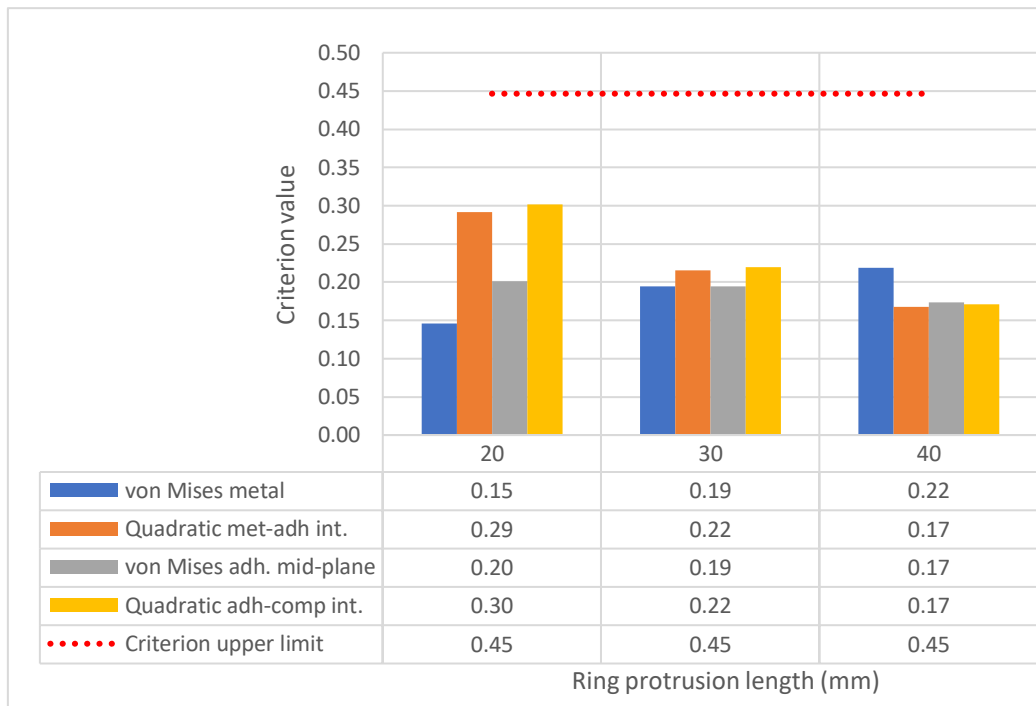
Figure 3.23 Criteria values of different ring protrusion lengths (Metal part & adhesive layer)

	20	30	40
Fiber Hashin	0.12	0.12	0.11
Matrix Hashin	5.79	5.21	3.75
Out of plane Hashin	7.06	6.00	5.26
Criterion upper limit	0.45	0.45	0.45

Ring protrusion length (mm)

Figure 3.24 Criteria values of different ring protrusion lengths (Composite cylinder)

Figure 3.23 and Figure 3.24 show a gradual reduction of the criterion values not only in the adhesive but also in the composite as the ring protrusion gets longer. However, Matrix and Out of plane Hashin criteria values still exceed the maximum permissible criterion value, leading to high possibilities of matrix failure or delamination.

Adhesive thickness

The next parameter of the study is the adhesive thickness. Three different values of adhesive thickness, apart from the initial (1mm), are investigated: 1.25, 0.75 and 0.50mm.

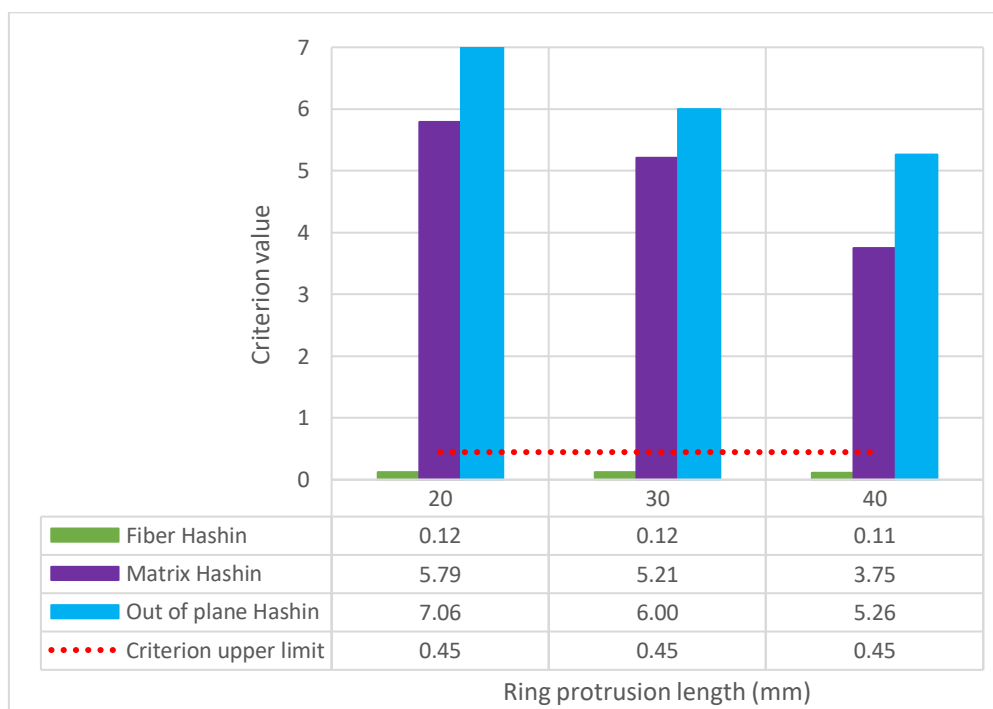|	1.25	1	0.75	0.5
von Mises metal	0.18	0.18	0.20	0.20
Quadratic met-adh int.	0.22	0.22	0.21	0.21
von Mises adh. mid-plane	0.18	0.19	0.18	0.19
Quadratic adh-comp int.	0.22	0.22	0.21	0.21
Criterion upper limit	0.45	0.45	0.45	0.45
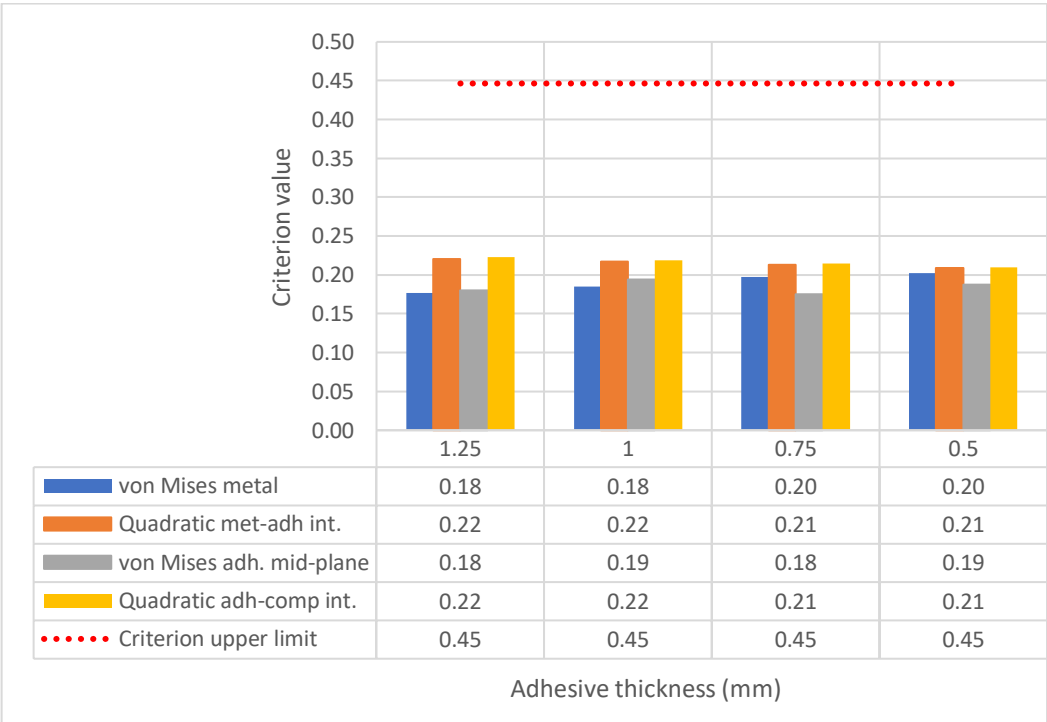
Figure 3.25 Criteria values of different adhesive thicknesses (Metal part & adhesive layer)

	1.25	1	0.75	0.5
Fiber Hashin	0.11	0.12	0.13	0.13
Matrix Hashin	5.10	5.21	5.68	6.15
Out of plane Hashin	5.95	6.10	6.34	6.81
Criterion upper limit	0.45	0.45	0.45	0.45

Figure 3.26 Criteria values of different adhesive thicknesses (Composite cylinder)

The obtained results regarding the metal part and the adhesive layer are stated in Figure 3.25. It is observed there is a slight reduction in stresses developed in the adhesive layer and a slight increase in stresses developed in the metal part as the adhesive thickness reduces. As for

the composite cylinder, the results are stated in Figure 3.26. The differences are not significant also in the Hashin criterion, while thinner adhesives cause lower stresses in the cylinder compared to thicker ones.

Stacking sequence

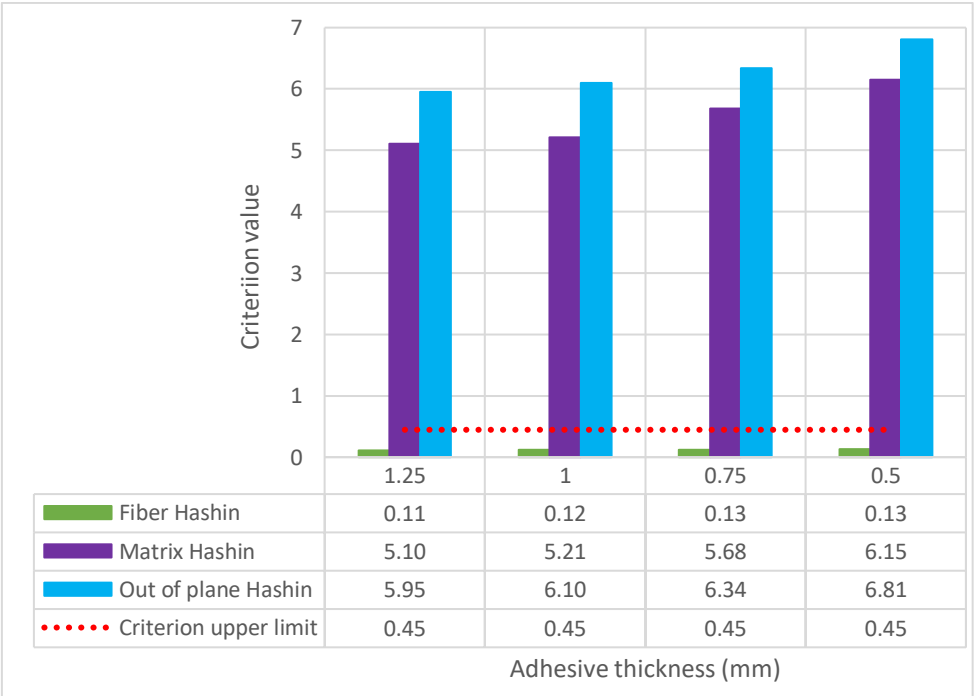An important factor worth to be investigated is the stacking sequence, which has a large impact on adhesive joint strength according to literature. Already mentioned in Section 3.1.1, the pattern of stacking sequence that was used so far is $[\pm 55°]_{10}$. The analysis is run for six more different stacking sequences. The first two, $[\pm 45°]_{10}$ and $[\pm 60°]_{10}$, are chosen so that the effect of both higher and lower winding angle values are examined. Based on the fact that the stacking sequence $[\pm 55°]_{10}$ is recommended by literature, it is decided to stay close to this value.

	[±45°]10	[±55°]10	[±60°]10
von Mises metal	0.25	0.19	0.18
Quadratic met-adh int.	0.16	0.22	0.22
von Mises adh. mid-plane	0.23	0.19	0.20
Quadratic adh-comp int.	0.17	0.22	0.22
Criterion upper limit	0.45	0.45	0.45
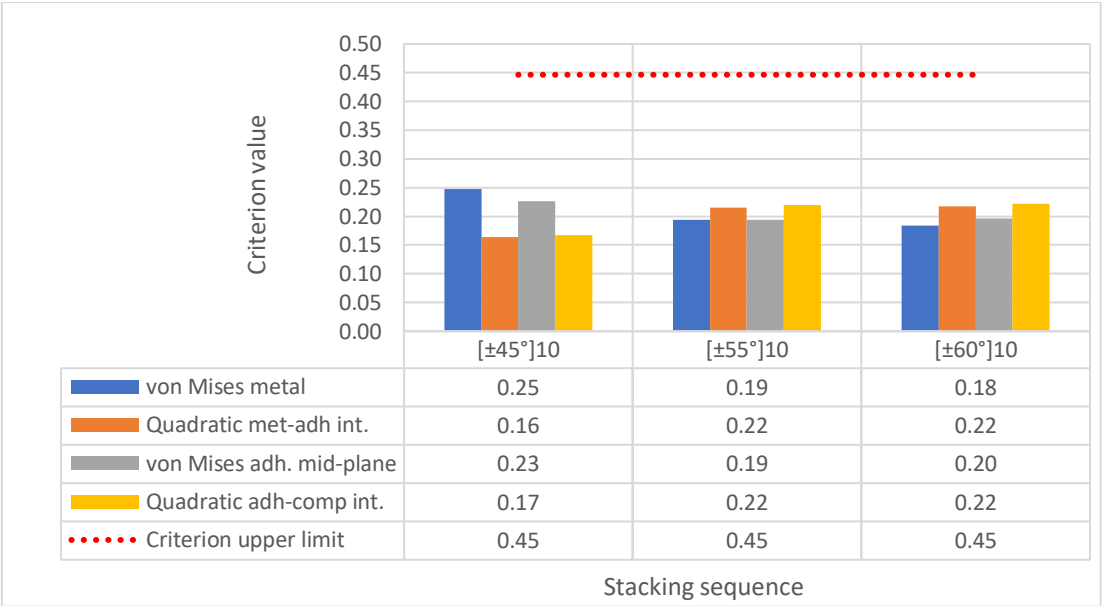
Figure 3.27 Criteria values of different $[\pm\theta°]$ stacking sequences (Metal part & adhesive layer)

	[±45°]10	[±55°]10	[±60°]10
Fiber Hashin	0.16	0.12	0.11
Matrix Hashin	2.86	5.21	9.38
Out of plane Hashin	11.26	6.00	6.41
Criterion upper limit	0.45	0.45	0.45

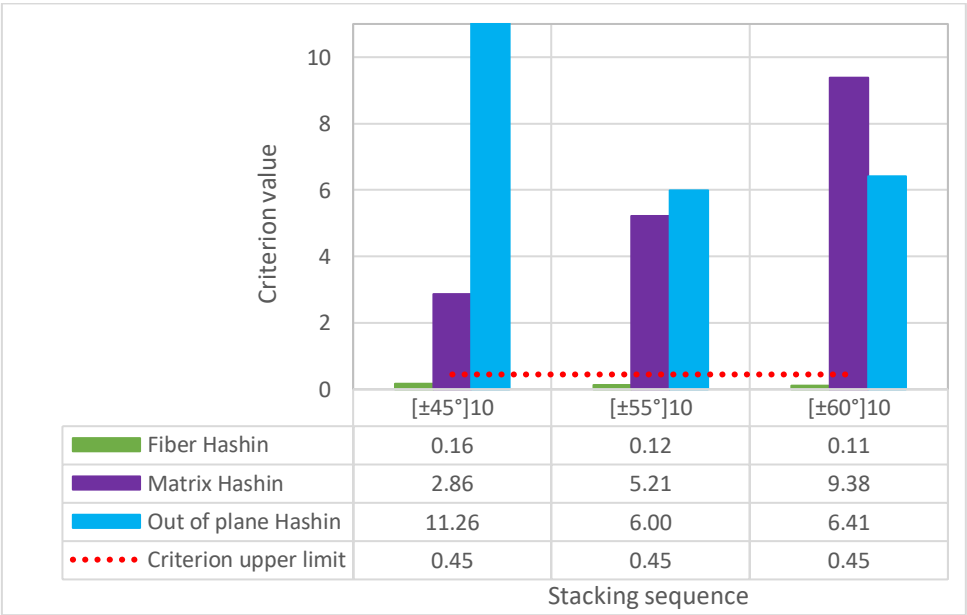**Figure 3.28** Criteria values of different $[\pm\theta°]$ stacking sequences (Composite cylinder)

From Figure 3.27 and 3.28, it can be seen that the criterion values regarding the metal part and the adhesive mid-plane increase as the angle of the fiber direction approaches lower values. It is observed, though, that the fiber direction closer to 0° seems profitable for the stresses developed in the adhesive-composite interface and the Hashin matrix criterion.

At this stage, it is noted that the asymmetric stress field presented in the composite cylinder with stacking sequence $[\pm 55°]_{10}$ is also observed in the composite cylinders with $[\pm 45°]_{10}$ and $[\pm 60°]_{10}$. These three patterns are not axisymmetric so the axisymmetric stacking sequence $[0°]_{20}$ was tested in order to check if this asymmetry was due to the stacking sequence or another reason. Indeed, the stress field of stacking sequence $[0°]_{20}$ was symmetric, leading to the conclusion that the results are slightly affected by the combination of a non axisymmetric stacking sequence with symmetric boundary conditions.

It must be underlined that the adhesive joint requires an increased stiffness in the axial direction of the material, so that the contact between the adhesive layer and the composite material is enhanced and able to avoid high stress concentrations right at the end of the 30 mm ring protrusion length. This fact leads to the decision of adding layers on the internal side of the stacking sequence, with fibers as close to the axial direction as possible. Therefore, it is decided to use a number of internal pairs $[\pm \varphi°]$ where φ angle is close to 0°. What seems also interesting is the effect of an external pair $[\pm \varphi°]$, leading to the examination of a 'symmetric pattern' $[\pm \varphi°/(\pm \theta°)_8/\pm \varphi°]$. The angle φ is chosen to be equal to 15° for manufacturing feasibility, keeping as main stacking sequence the $[\pm 55°]$. Therefore, the final four stacking sequence patterns examined are: $[\pm 15°/(\pm 55°)_9]$, $[(\pm 15°)_2/(\pm 55°)_8]$, $[(\pm 15°)_3/(\pm 55°)_7]$ and $[\pm 15°/(\pm 55°)_8/\pm 15°]$.

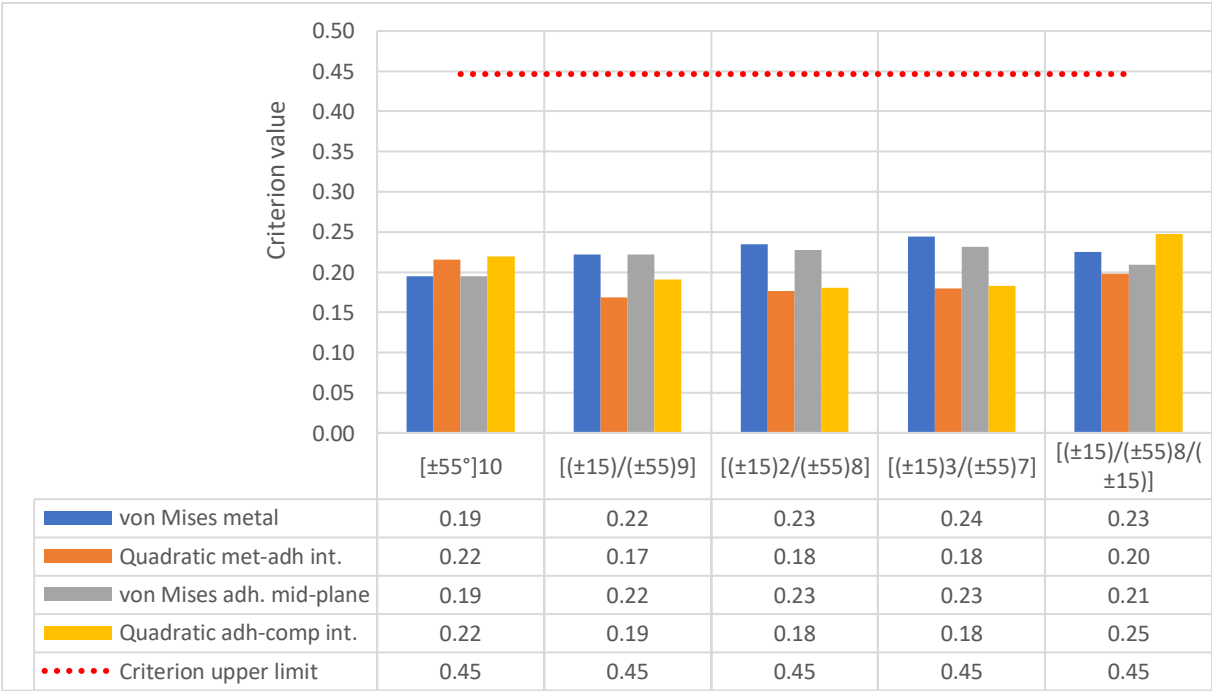|	$[\pm 55°]10$	$[(\pm 15)/(\pm 55)9]$	$[(\pm 15)2/(\pm 55)8]$	$[(\pm 15)3/(\pm 55)7]$	$[(\pm 15)/(\pm 55)8/(\pm 15)]$
von Mises metal	0.19	0.22	0.23	0.24	0.23
Quadratic met-adh int.	0.22	0.17	0.18	0.18	0.20
von Mises adh. mid-plane	0.19	0.22	0.23	0.23	0.21
Quadratic adh-comp int.	0.22	0.19	0.18	0.18	0.25
Criterion upper limit	0.45	0.45	0.45	0.45	0.45

Figure 3.29 Criteria values of different $[(\pm \varphi°)_i /(\pm \theta°)_{10-i}]$ stacking sequence patterns
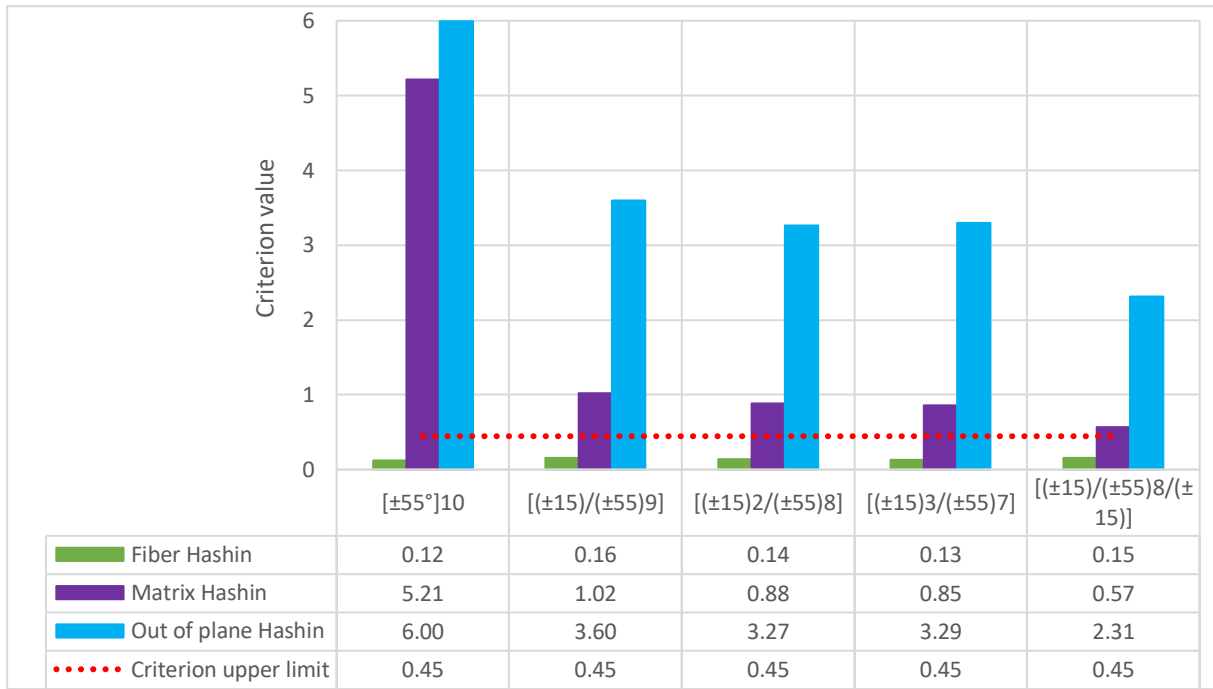
(Metal part & adhesive layer)

	[±55°]10	[(±15)/(±55)9]	[(±15)2/(±55)8]	[(±15)3/(±55)7]	[(±15)/(±55)8/(± 15)]
■ Fiber Hashin	0.12	0.16	0.14	0.13	0.15
■ Matrix Hashin	5.21	1.02	0.88	0.85	0.57
■ Out of plane Hashin	6.00	3.60	3.27	3.29	2.31
••••• Criterion upper limit	0.45	0.45	0.45	0.45	0.45

Figure 3.30 Criteria values of different $[(\pm\varphi°)_i /(\pm\theta°)_{10\text{-}i}]$ stacking sequence patterns
(Composite cylinder)

Figure 3.29 and figure 3.30 show the results of the analysis. The replacement of the internal plies [±55°] with [±15°] has no significant effect on the metal part and the adhesive layer. Nevertheless, the composite cylinder seems to present a huge reduction of the values of the Matrix Hashin criterion. The main reason is that in ±15° pattern the loading creates higher stresses Sff aligned to the fibers but lower stress Spp perpendicular to the fibers and lower in-ply shear stress Sfp in comparison with the ±55° pattern. The fact that Hashin Matrix is strongly dependent, among others, on Spp and Sfp, justify the difference. Note that the parallel study which examined the effect of these stacking sequences on eigenvalue buckling concluded that more than one pairs of [±15°] layers end up in a more prone to buckling structure. Therefore, the compromise reached between the results of this eigenvalue buckling analysis and the results of the linear static analysis of the present study is stacking sequence $[\pm15°/(\pm55°)_9]$.

Cylinder thickness

Observing that the Matrix and Out of plane Hashin are the criteria exceeding the limit, the drastic increase of cylinder thickness by 50% is the next attempt, while the outer diameter of the cylinder remains constant.
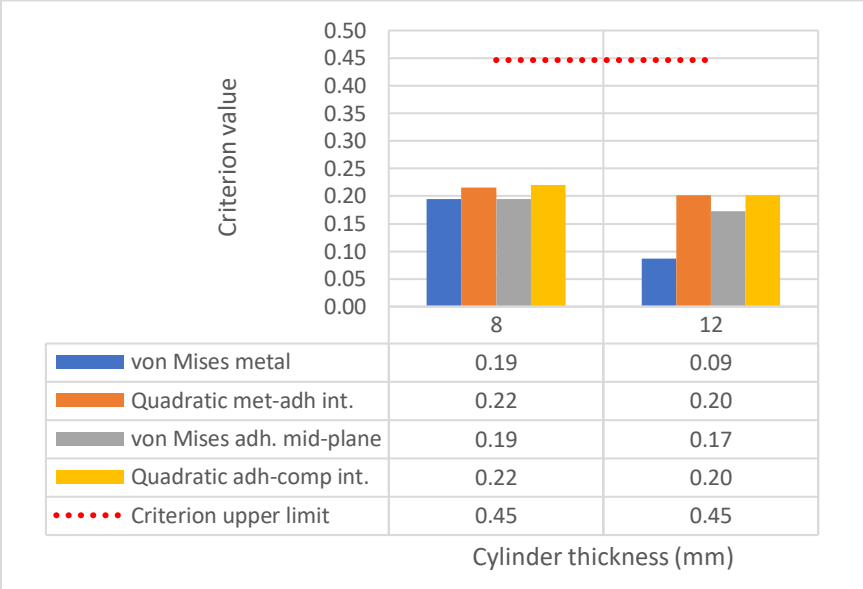

	8	12
von Mises metal	0.19	0.09
Quadratic met-adh int.	0.22	0.20
von Mises adh. mid-plane	0.19	0.17
Quadratic adh-comp int.	0.22	0.20
Criterion upper limit	0.45	0.45

Cylinder thickness (mm)

Figure 3.31 Criteria values of different cylinder thickness (Metal part & adhesive layer)

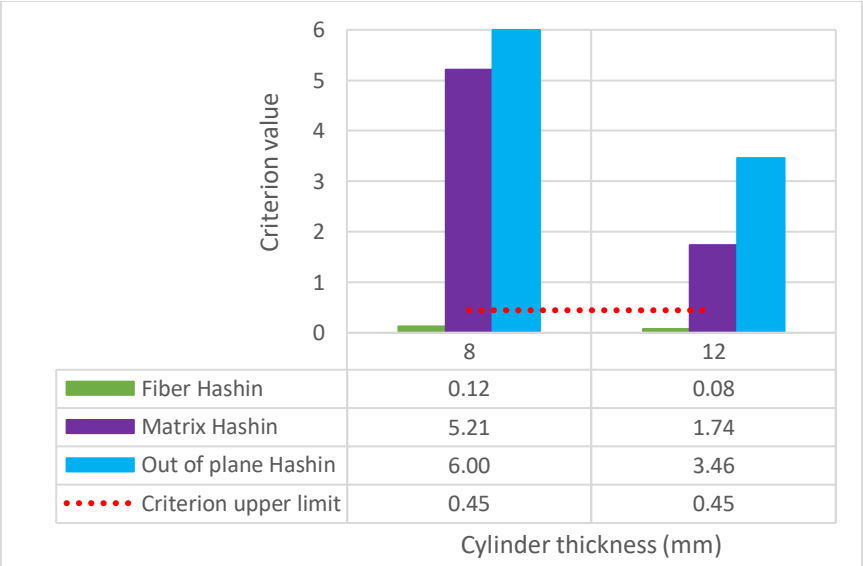|	8	12
Fiber Hashin	0.12	0.08
Matrix Hashin	5.21	1.74
Out of plane Hashin	6.00	3.46
Criterion upper limit	0.45	0.45

Cylinder thickness (mm)

Figure 3.32 Criteria values of different cylinder thickness (Composite cylinder)

Figures 3.31 and 3.32 indicate that the stresses developed in every component of the thicker cylinder are significantly lower especially in Matrix and Out of plane Hashin criteria. Although 50% increase of thickness contributed to more than 50% decrease of Matrix Hashin value and more than 40% decrease of Out of plane Hashin criterion, the values still exceed the limit.

77

Material properties

The parametric study ends with a material properties investigation. Firstly, the effect of a CFRP consisting of 24K fibers with higher strength limits and secondly, the effect of a more ductile adhesive are examined. The names and the properties of the materials have already been stated in Tables 2.8 and 2.9.
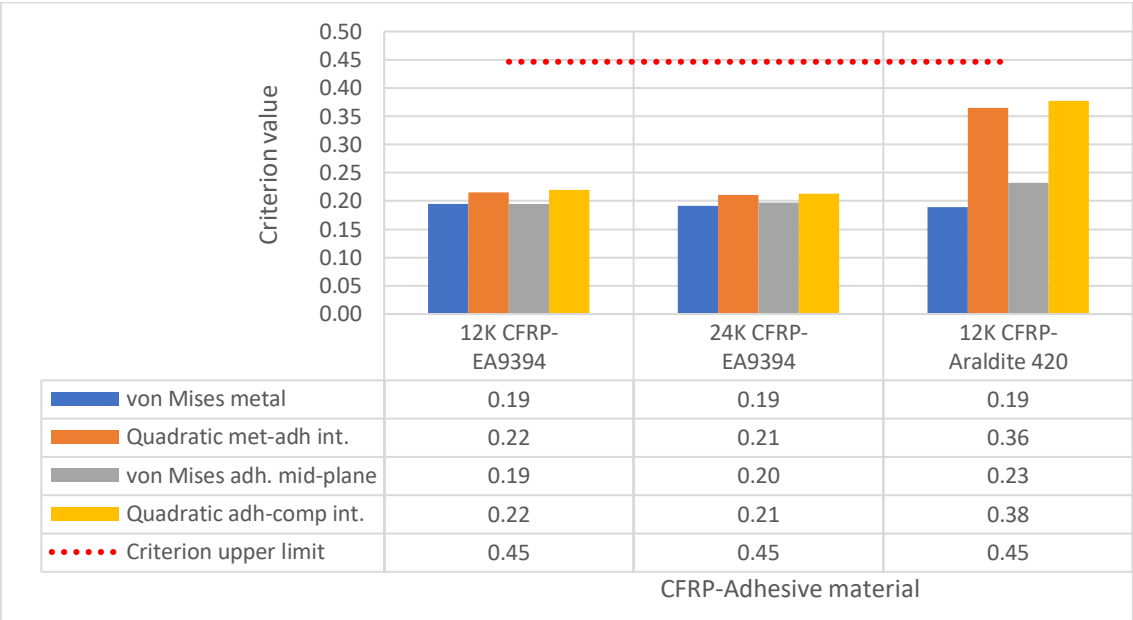

	12K CFRP-EA9394	24K CFRP-EA9394	12K CFRP-Araldite 420
von Mises metal	0.19	0.19	0.19
Quadratic met-adh int.	0.22	0.21	0.36
von Mises adh. mid-plane	0.19	0.20	0.23
Quadratic adh-comp int.	0.22	0.21	0.38
Criterion upper limit	0.45	0.45	0.45

CFRP-Adhesive material

Figure 3.33 Criteria values of different material properties (Metal part & adhesive layer)

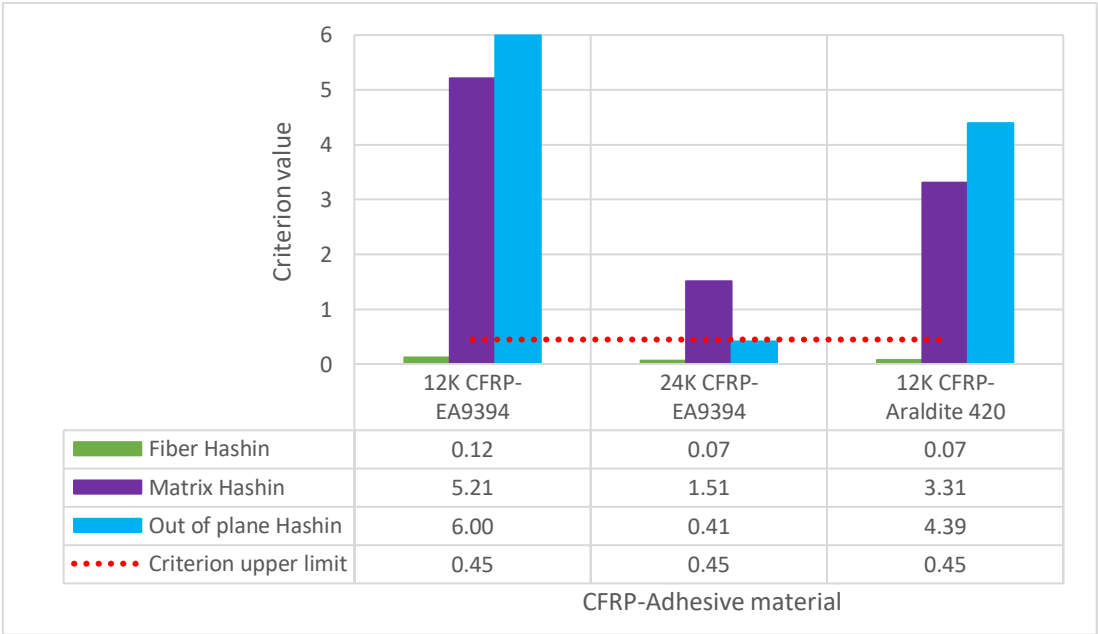|	12K CFRP-EA9394	24K CFRP-EA9394	12K CFRP-Araldite 420
Fiber Hashin	0.12	0.07	0.07
Matrix Hashin	5.21	1.51	3.31
Out of plane Hashin	6.00	0.41	4.39
Criterion upper limit	0.45	0.45	0.45

CFRP-Adhesive material

Figure 3.34 Criteria values of different material properties (Composite cylinder)

Figures 3.33 and 3.34 enable the comparison between the results obtained from the materials used in the study so far and the results from the alternative material options. From Figure 3.33 it can be seen that the values for the ductile adhesive Araldite 420 are higher, which is explained by its lower strength limits. From Figure 3.34, the impact of the higher strength

limits of CFRP is obvious, contributing to approximately 3.5 times lower Matrix Hashin value and 14 times lower Out of plane Hashin value.

Conclusions and comments on the parametric study

Some interesting conclusions have been reached from the FE analysis of DC No 3a. The first conclusion is that in every case examined matrix and delamination failure are highly predicted according to the corresponding Hashin criterion value. In fact, the maximum values are localized in the area of adhesive joint end which is a stress concentration area. In similar applications, local reinforcements are usually applied in order to avoid possible damage. The second conclusion has to do with the most influencing factors. The effect of the different parameters is evaluated, focusing on the 'weak component' which is the cylinder and especially, its matrix part. The larger impact comes from the stacking sequence and the CFRP material. The internal pair [±15] reduces the Matrix criterion to a great extent while 24K T700 epoxy CFRP offers extremely better results of Matrix and Out of plane Hashin criteria. Other factors, such as the cylinder thickness and the design geometric versions of metal part, contribute to the reduction of the stresses but to a lesser extent. Bearing in mind these conclusions, a combination of the 24K T700 epoxy CFRP and the stacking sequence pattern $[\pm15/(\pm55)_9]$ is the recommended next step of the project. Indeed, a run of the model of DC No3a is conducted after applying these two changes. The obtained results are presented and compared with the corresponding ones of a full cylindrical model in Section 4.2.3.2.

3.2.2.4 Results of linear static analysis of design concepts No 3.1a and No 3.1b

The presentation of the results of the two design concepts is conducted in parallel, in an attempt to present a concise study and compare the response of the two configurations. The analysis starts by plotting the deformed shape of the models along with the displacements field that is created. Apart from DC No 3.1a and No 3.1b, DC No 3a is presented and used for comparison in Figure 3.35. From the first look, the difference in radial displacement (U1) between the DCs No3.1a, No3.1b and DC No3a is remarkable. The adhesive joint area presents way less bending stiffness, leading to an intense S-shape deformation of the cylinder in that area and a larger axial displacement of the central part of metal end-cap.
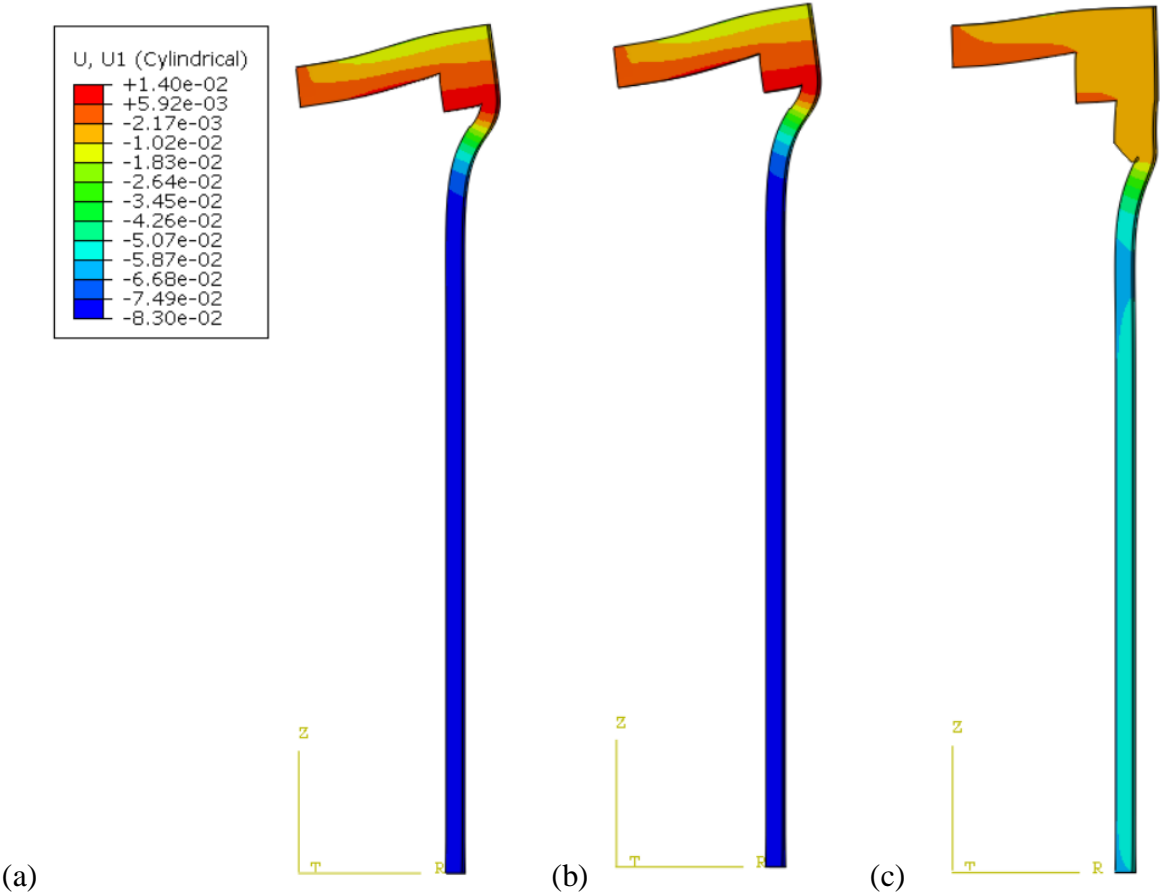

(a)   (b)   (c)

Figure 3.35 Contour plot of radial displacement distribution of (a) DC No 3.1a (b) DC No 3.1b (c) DC No 3a
Deformed shape (deformation scale factor: 200)

The next step is the investigation of the stress field of the structure.

Metal part

The metal part of the models, including the end-cap and the ring, presents stress concentrations at the internal corners, where abrupt geometric changes occur (Figure 3.36). The maximum von Mises stress value, developed in DCs No 3.1a and No 3.1b, is 152 MPa and 143 MPa, respectively. Applying the von Mises criterion considering σ_Y=480 MPa as indicated in Table 2.7, the criterion values equals to 0.32 and 0.30 which are lower than the maximum permissible criterion value of 0.45.
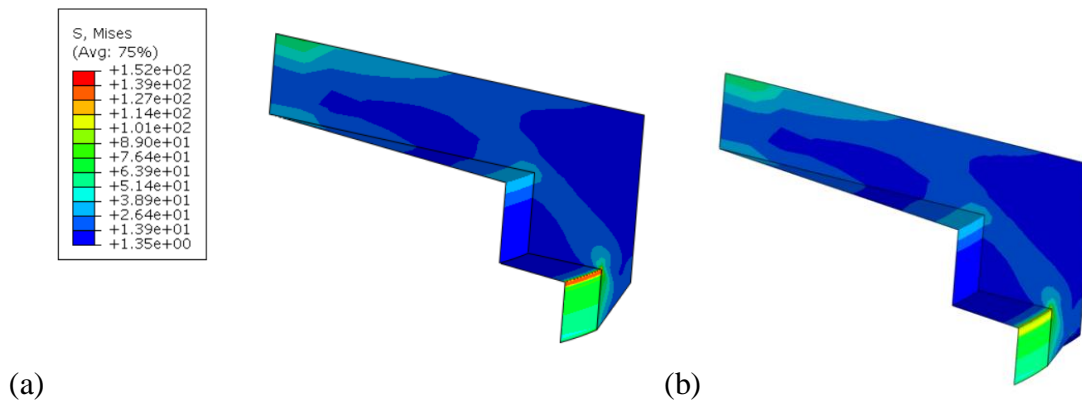
Figure 3.36 Contour plot of Von Mises stress distribution of metal part (a) DC No 3.1a (b) DC No 3.1b Undeformed shape

Adhesive layer

The adhesive joint of this configuration has a skew angle. In DC No 3.1a, it is a pure scarf joint while in DC No3.1b, it combines a scarf and a butt joint. The contour plots of peel stress (in z-axis direction) S33 distribution (using a Cartesian coordinate system with a x-y plane on the adhesive surface and z normal to it) are shown in Figure 3.37. It is underlined that only in this Section (3.2.2.4) the symbol S33 is used for demonstrating the peel stresses in the inclined part of the adhesive layer. The differences in peel stresses between the two models are negligible. It is apparent that the side of adhesive situated in the internal part of the cylinder develops the higher compressive stresses.
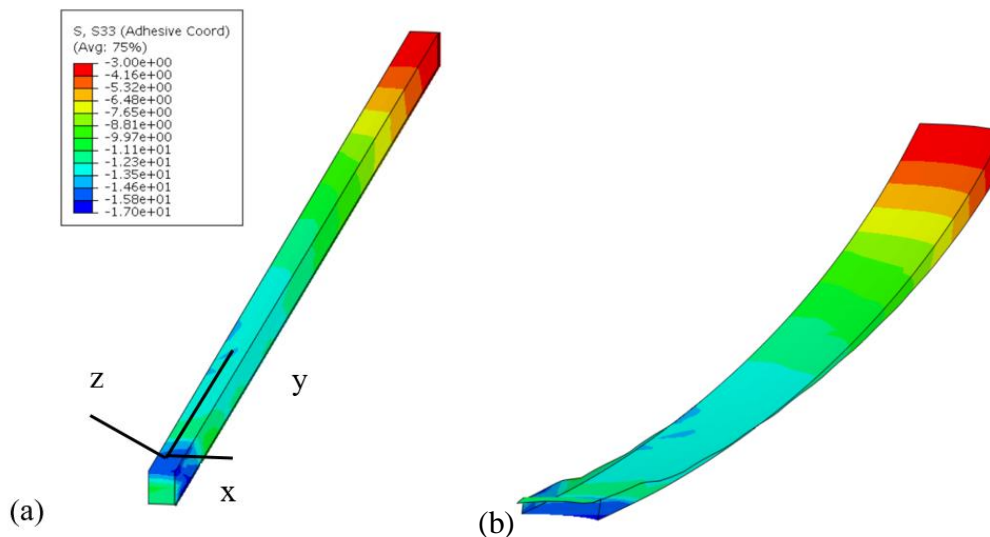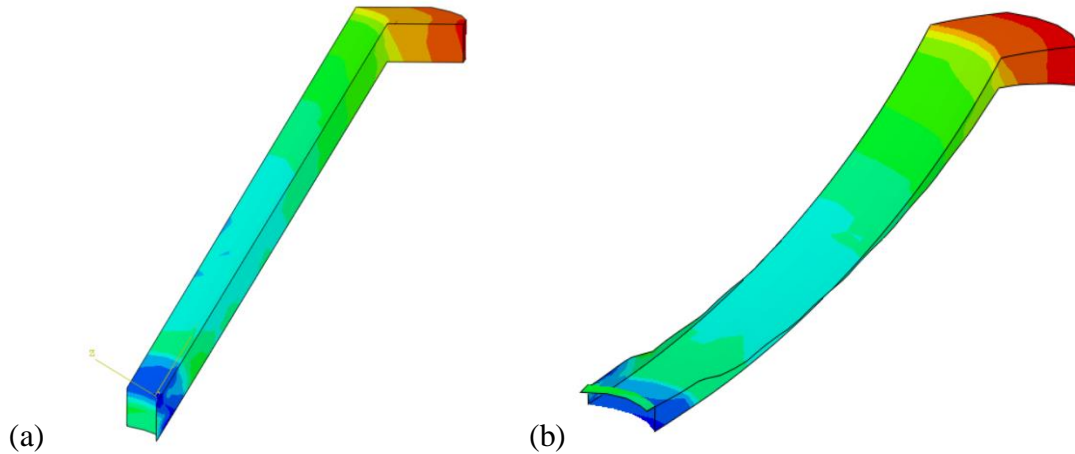
Figure 3.37 Contour plot of peel stress distribution of adhesive layer (a) DC No 3.1a (b) DC No 3.1b
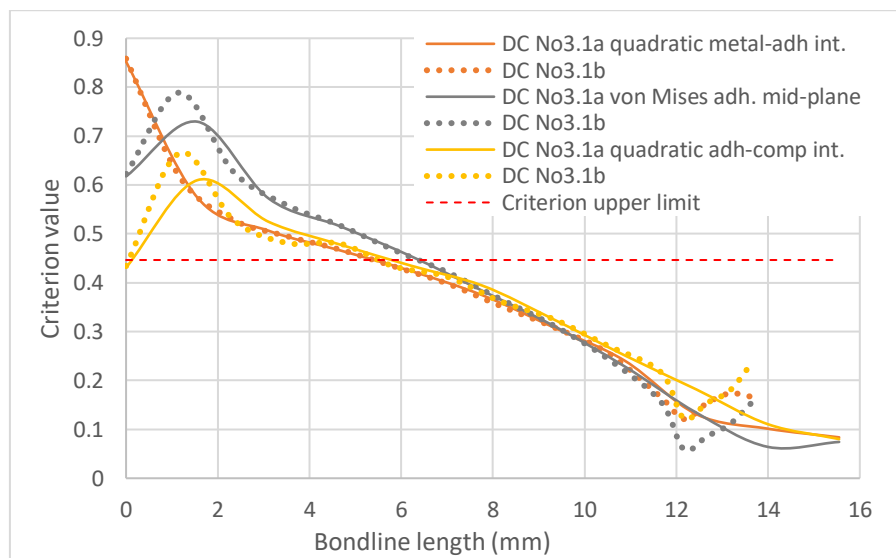Undeformed-Deformed shape (deformation scale factor: 200)

Figure 3.38 Criterion value along the bondline length of adhesive layer
(Continuous line: DC No 3.1a, Dotted line: DC No 3.1b)

Figure 3.38 shows that, taking into consideration the initiation length (9.5mm) from the edge, the adhesive layer criteria values in the interfaces as well as in the mid-plane. What seems interesting is the crest formed in the first millimeters. It is explained given that the angle changes from -15° to 55° in the stacking sequence pattern. As it can be seen, it affects the stresses in the adhesive-composite interface and in the mid-plane. As for the crest formed in the last millimetres in the case of No3.1b it comes from the different inclination of two planes of adhesive layer.

Composite cylinder

The results shown in Figure 3.39 come from the governing mode of the Hashin criterion, the Compressive Matrix Hashin, since the Fiber and Out of plane Hashin criteria values satisfy the limit. It is observed that the higher values are reached in Ply 3 (the first ply with angle of fiber direction 55°) in the area which is in contact with the adhesive layer. Both maximum

values exceed the required upper limit (0.45) predicting possible matrix failure. The damaged area is depicted in grey color.
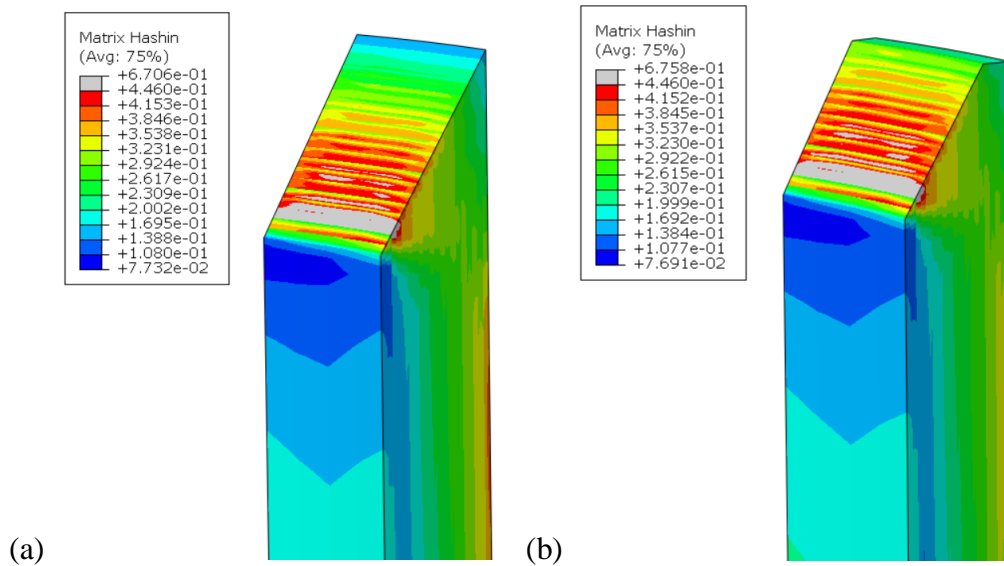

(a)   (b)

Figure 3.39 Contour plot of Matrix Hashin criterion distribution
(a) DC No 3.1a (b) DC No 3.1b

3.2.2.5 Parametric study of design concepts No 3.1a and No 3.1b

In this section, the effect of two parameters on the design concepts with the tapered cylinder is examined (Figure 3.40). A larger skew angle as well as a longer flat part of DC No 3.1b are analyzed and compared with the initial designs.
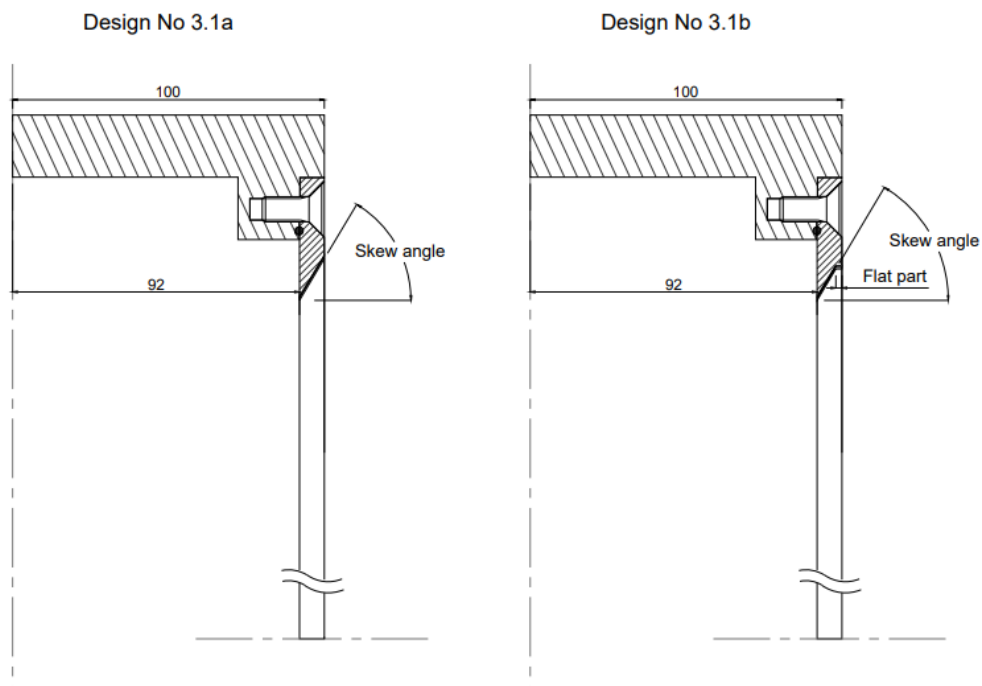

Figure 3.40 Visualization of the parameters examined in the parametric study

Skew angle

An increase of the initial value of 60° by 25% is the first stage of the parametric study. The first four groups of columns in Figures 3.41 and 3.42 show the results. As it is illustrated, the results of DC No 3.1a and No 3.1b are almost the same. What causes an extreme improvement in structural behavior is the 70° skew angle.

Length of the flat part

An increase of the initial value of 2mm by 100% is the second stage, keeping the skew angle equal to 60°. The results, visualized in the fifth group of columns in Figures 3.41 and 3.42, show the important increase in stresses and therefore in criteria values compared to the third group of columns. The only component which benefits from longer flat part is the metal part because of the increased bending stiffness.
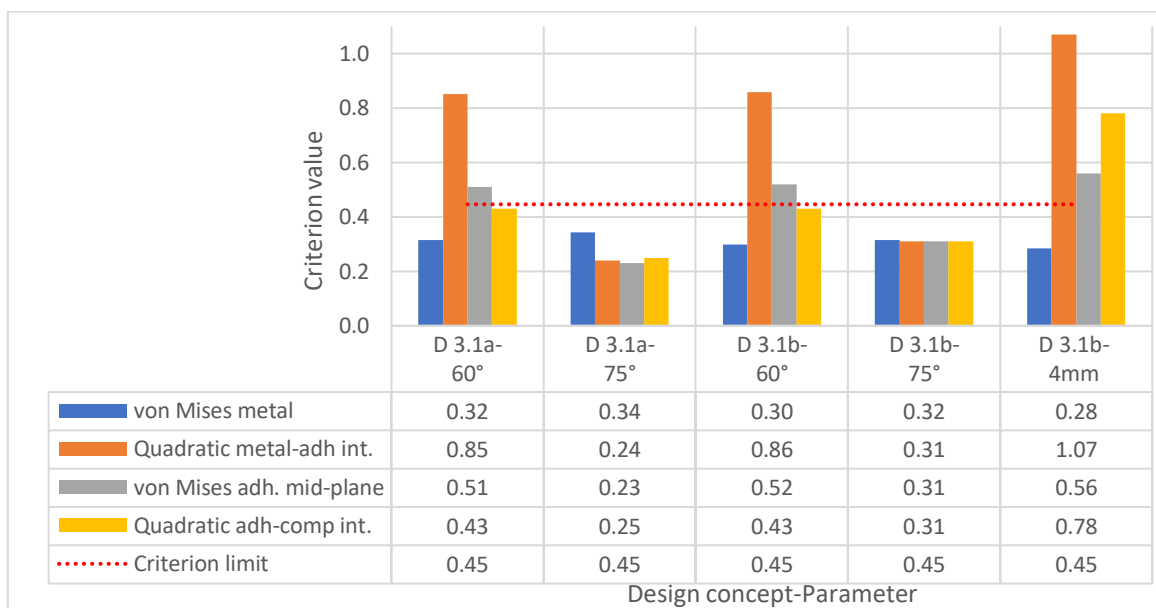

	D 3.1a-60°	D 3.1a-75°	D 3.1b-60°	D 3.1b-75°	D 3.1b-4mm
von Mises metal	0.32	0.34	0.30	0.32	0.28
Quadratic metal-adh int.	0.85	0.24	0.86	0.31	1.07
von Mises adh. mid-plane	0.51	0.23	0.52	0.31	0.56
Quadratic adh-comp int.	0.43	0.25	0.43	0.31	0.78
Criterion limit	0.45	0.45	0.45	0.45	0.45

Figure 3.41 Criteria values of different parameters (Metal part & adhesive layer)

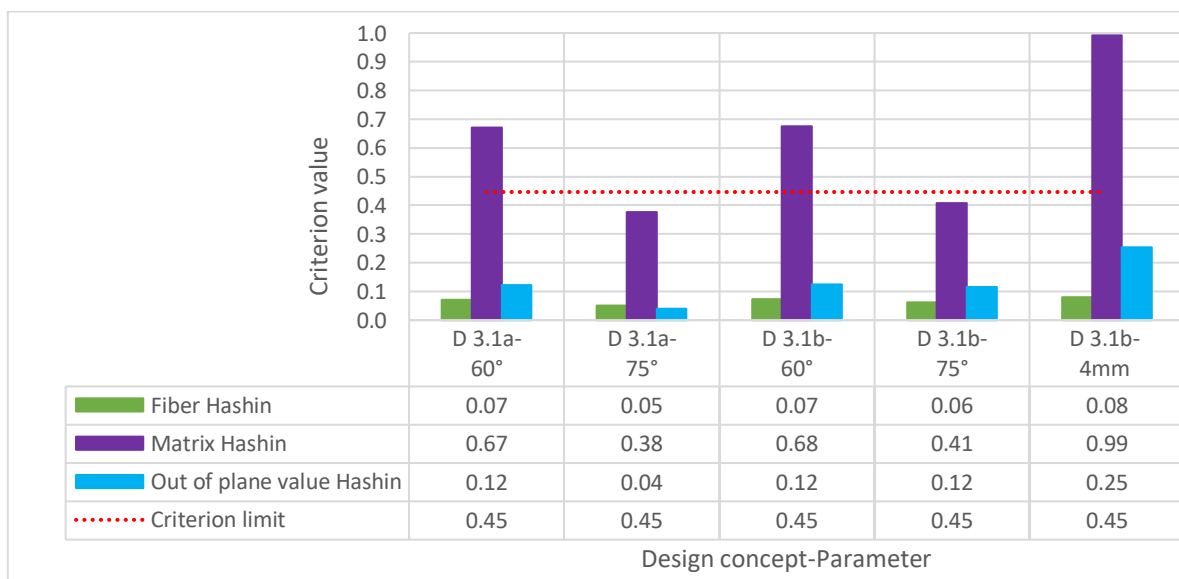|	D 3.1a-60°	D 3.1a-75°	D 3.1b-60°	D 3.1b-75°	D 3.1b-4mm
Fiber Hashin	0.07	0.05	0.07	0.06	0.08
Matrix Hashin	0.67	0.38	0.68	0.41	0.99
Out of plane value Hashin	0.12	0.04	0.12	0.12	0.25
Criterion limit	0.45	0.45	0.45	0.45	0.45

Figure 3.42 Criteria values of different parameters (Composite cylinder)

Conclusions and comments on the parametric study

Some interesting conclusions have been reached from the FE analysis of DC No 3.1a and No 3.1b. Firstly, the differences between the values of Design No 3.1a and No 3.1b are negligible. The reason is that the maximum stresses are developed in corresponding areas of the two models which have the same or similar geometry. The recommended option is the DC No3.1b as the flat radial part make its construction feasible and less prone to local damages. Secondly, the strong positive effect of skew angle increase cannot be ignored. The larger the angle is, the larger the surface of the adhesion and the smoother the stress transitions from layer to layer of the composite cylinder become. Thirdly, the negative effect of flat part length increase should not be ignored especially in the 3rd ply in the interface with the 2nd ply. The fact is explained by the increase of bending stiffness in the joint area which causes reduction of displacements and increase of stresses. A compromise should be reached for a relatively short flat part but long enough to protect the cylinder edge from local damages.

3.2.3 Conclusions and comments

The initial design, the ABAQUS model set-up and a preliminary optimization of three alternative models of the pressure vessel was completed in this chapter. The DCs No3a, No3.1a and No3.1b were chosen and introduced in the software using a 10° sliced FE model. What was observed in the results was an asymmetry in the stress field with respect to the plane of symmetry of the slice owing to a non axisymmetric stacking sequence, constrained by symmetric BC. The stresses developed in the two sides of the model present a difference up to 5%.

The parametric study considering the design No3a showed that the stacking sequence and the CFRP properties and strength limits play a significant role in the structural behavior of the whole vessel. On one hand, the use of internal layers with fibers almost parallel to the cylinder axis is beneficial to the adhesive joint area and the composite-adhesive interface, especially in the case of a single lap joint. On the other hand, opting for a CFRP consisting of 24K fibers with higher strength limits contributes to lower Hashin values and reduces the risk of matrix failure.

The parametric study regarding the designs No 3.1a and 3.1b showed that the latter combining a large skew angle and a short flat part is the preferred option. The reason is the structural reliability that presents and the more internal space for the equipment that it offers. However, it is underlined that the milling processes should be avoided in cases of prone to local damage materials, such as CFRP, if there are other alternatives. Another solution to the construction of a cylinder with tapered edge is the use of a dissoluble mandrel with protrusions at the edges.

Finally, it is decided to proceed to the next step of the study with DC No3a as it is more feasible and simpler in terms of manufacturing and adjustment process. Moreover, the adhesion surface is larger contributing to the adhesive joint strength and the higher stresses in composite cylinder are developed in ply 1 which is the internal ply. This means that if need be, some local reinforcements can be applied. Another advantage of DC No3a compared to DC No3.1b is that the former offers the possibility to adjust the thickness of the ring in order to be effective also in the bolted connection.

CHAPTER 4

Numerical modeling: Full cylindrical model

In this chapter, the full cylindrical model of the pressure vessel is developed and analyzed. Firstly, the results of the linear static analysis are discussed in order to assess the previously obtained results. Secondly, an eigenvalue and nonlinear buckling analysis of the pressure vessel are performed in order to reach more realistic conclusions regarding the structural behavior and design optimization of the pressure vessel.

4.1 Development of a full cylindrical model

The set-up of a full cylindrical model constitutes a time-consuming and demanding task. The main reason is that the continuum model approach requires modelling of a uniform structure and its division into partitions, afterwards. The proper material assignment to every partition and the proper orientation assignment in CFRP are mandatory. Another difficulty that was faced also in the mesh definition of the slice half cylinder model is the large difference between the thickness of the adhesive layer and the dimensions of the other components.

Following the parametric study of design concept (DC) No 3a, it is decided to investigate also the geometric version (ii) of DC No 3a, illustrated in Figure 3.19, using a full cylindrical model. It will be hereinafter referred to as DC No 3b. The geometry of DCs No 3a and No 3b are reminded in Figure 4.1. Since they are modeled in the same way in terms of material properties, stacking sequence, loading and boundary conditions, the information stated in the following sections for DC No 3a refer to both models.
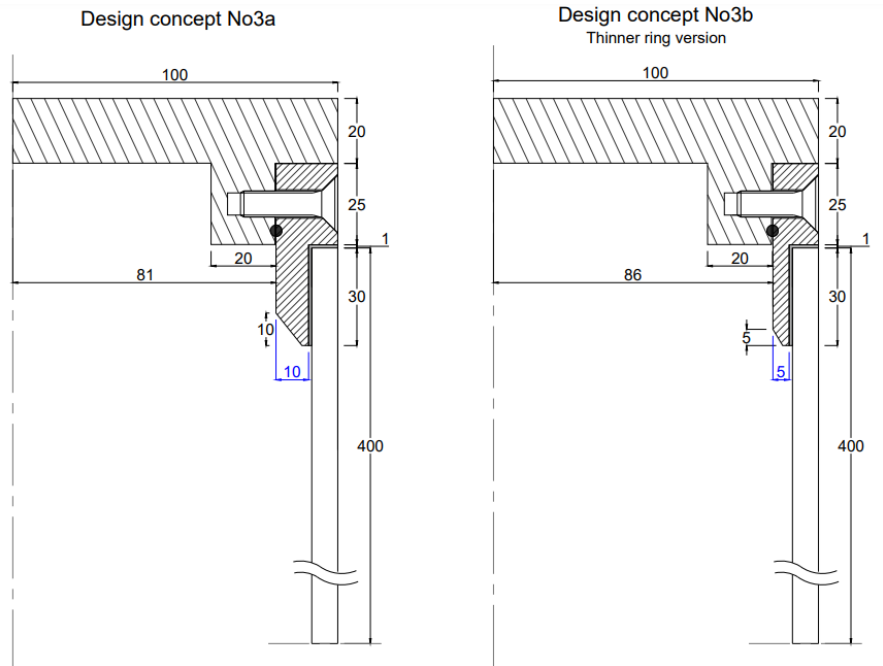

Figure 4.1 Sketches of DC No3a and No3b

4.1.1 Geometry, mesh and type of elements

The full cylindrical FE model of DC No 3a is developed with as many as possible similarities with the corresponding slice model. This is necessary for a reasonable comparison of the results. Similarly to the slice model set-up, the longitudinal cross section of DC No 3a is introduced in ABAQUS. In this case, however, it is decided to design the axisymmetric outline of the whole cylinder and revolve it by 360° (Figure 4.2), in an attempt to avoid mirror or symmetry BC tools that could affect the stacking sequence pattern. The next step is the creation of partitions corresponding to the different components. It is noted that the bolt is chosen not to be modeled neither in this case as it necessitates another study. The two metal parts are modelled in contact with each other using the same material, Al 6065-T6, while the adhesive is modeled with EA9394. The cylinder is modeled with 24K T700 epoxy CFRP and stacking sequence pattern $[\pm15/(\pm55)_9]$ as indicated by the results of the parametric study of DC No3a, having 20 plies in total. The properties of the materials have already been stated in Tables 2.7, 2.8 and 2.9. Regarding the way chosen to assign winding pattern, the Composite Section is preferred again for the reasons that have been already explained in Section 3.1.1.
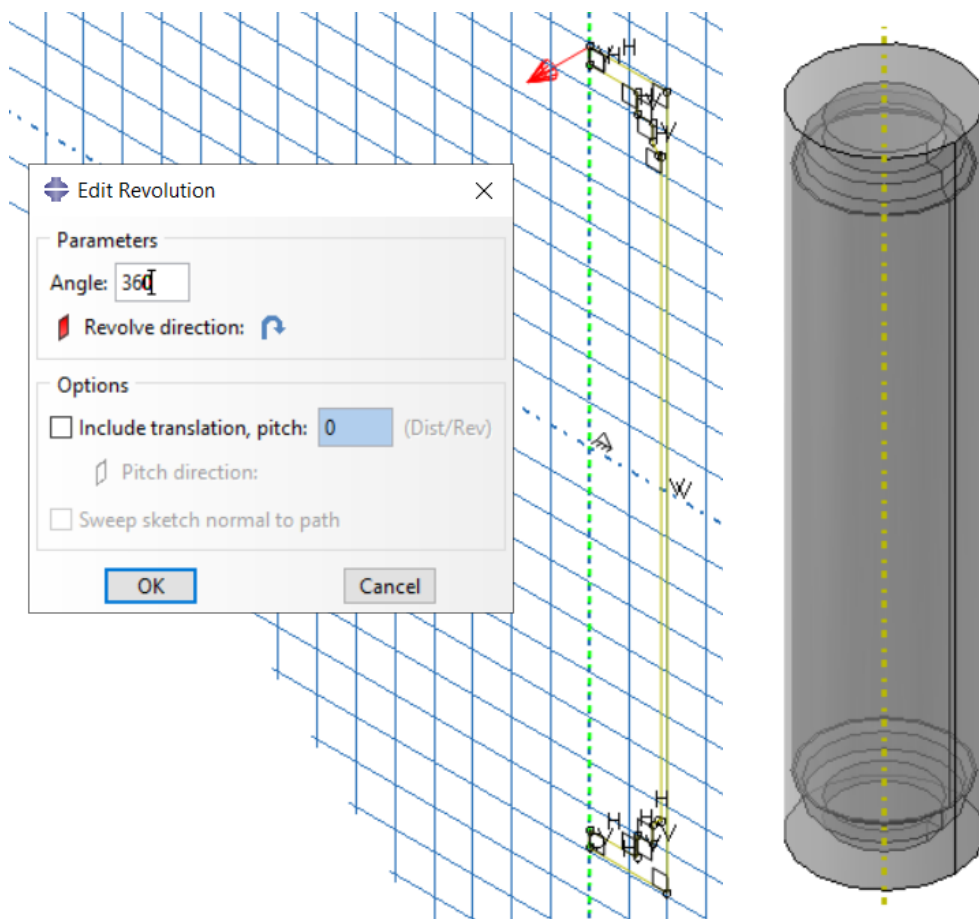

Figure 4.2 Longiditudinal cross section and 360° revolution during the set-up of the model DC No 3a

After the creation of the geometry, the material properties and the stacking sequence assignment, the element type has to be defined. Solid elements are used because of their advantages over the shell elements in the current case, which have been stated in Section 3.1.1. The large number of elements is alarming for the computational time, so the fast 8-node linear

3D solid element with reduced integration C3D8R sounds an appealing option. Although reduced integrated elements, such as C3D8R, are more time efficient, they give less accurate stress results than fully-integrated elements, such as C3D8, since the stresses are calculated on integration points. Therefore, the use of the fully integrated 8-node linear 3D solid element C3D8 is decided which are the same with the sliced model.

A mesh convergence study (MCS) was conducted in order to choose the proper mesh pattern that converges. The study is presented in detail in Section 4.2.1. As it is illustrated in Figure 4.3, a gradual mesh has been applied in the area around the joint starting from the finer mesh size of the elements of adhesive layer and ending in larger elements. More specifically, the adhesive layer is meshed with 6 elements across the thickness and 60 elements along the axial adhesive part. As for the cylinder, it is meshed with 1 element per cylinder's ply. The area of 30mm below the end of adhesive joint is meshed gradually, starting from 0.8mm and ending in 6mm element length. This mesh definition lead to a model of 175232 elements. The rest of the models mentioned in this chapter are designed after taking into account and adapting the conclusions of this MCS in the corresponding geometry.
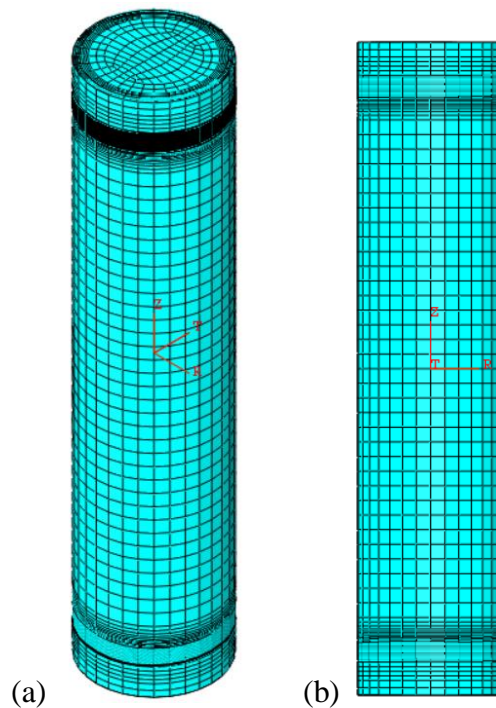

(a)   (b)

Figure 4.3 (a) Isometric view and (b) Side view of the meshed whole model of DC No3a
(6 elements per adhesive thickness, 60 elements along the axial part of the adhesive layer and 1 element per ply)

4.1.2 Loading conditions

The pressure vessel is subjected to a nominal external hydrostatic pressure of 40 bar or 4 MPa while the nominal internal pressure is equal to 1 bar or 0.1 MPa as shown in Figure 4.4. It is noted that, in an attempt to investigate the failure pressure of the structure with a nonlinear buckling analysis, a higher than the nominal maximum value of external pressure (4 MPa) is applied, equal to 16 MPa.
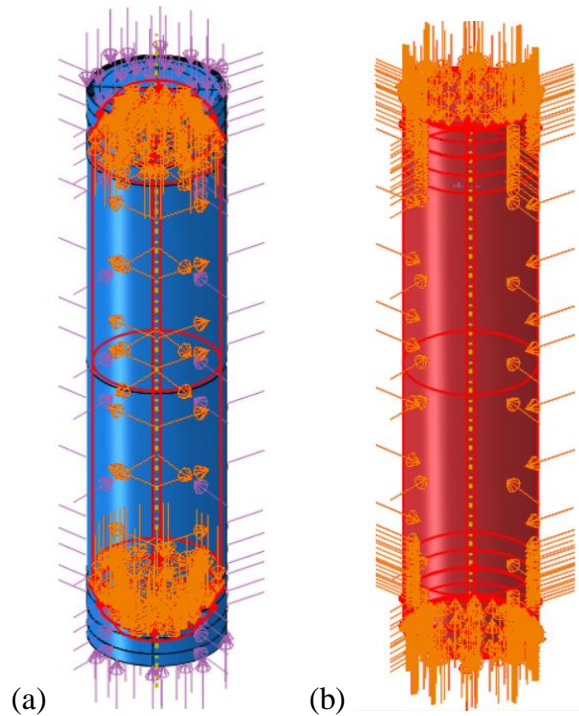
(a)   (b)

Figure 4.4 Application of the loading conditions on whole cylinder model

(a)   0.1 MPa internal pressure, (b) 4 MPa external pressure

4.1.3 Boundary conditions

The next task is the definition of the BCs. Modeling with finite elements an axisymmetric body (i.e. a cylinder) submerged in the deep sea and consequently loaded by the symmetric action of the external hydrostatic pressure presents problems related to its boundary conditions. The total absence of a real support of the structure makes inevitable the need for imposing artificial boundary conditions to avoid the rigid body motions of the structure. Three different sets of BCs are presented in this Section.

In the following sets of BCs, a cylindrical coordinate system using an axial direction aligned with this axis of the cylinder is used. In linear static analysis, the simplest BC is chosen. The central point, located in the external side, of the End-cap 1, is pinned as shown in Figure 4.5 (a). This means that the radial (U1), the circumferential (U2) and the axial (U3) displacements are fixed. In eigenvalue and nonlinear buckling analysis, the application of more restrictive BCs is obligatory. Therefore, two sets are examined shown in Figure 4.5 (b) and (c). In the first one, all translations are constrained (U1=U2=U3=0) at the circumference of End-cap 1 and all but axial translation are constrained (U1=U2=0) at the central point of End-cap 2. In the second one, all translations are constrained (U1=U2=U3=0) at the central point of End-cap 1 and all but axial translation are constrained (U1=U2=0) at the central point of End-cap 2.
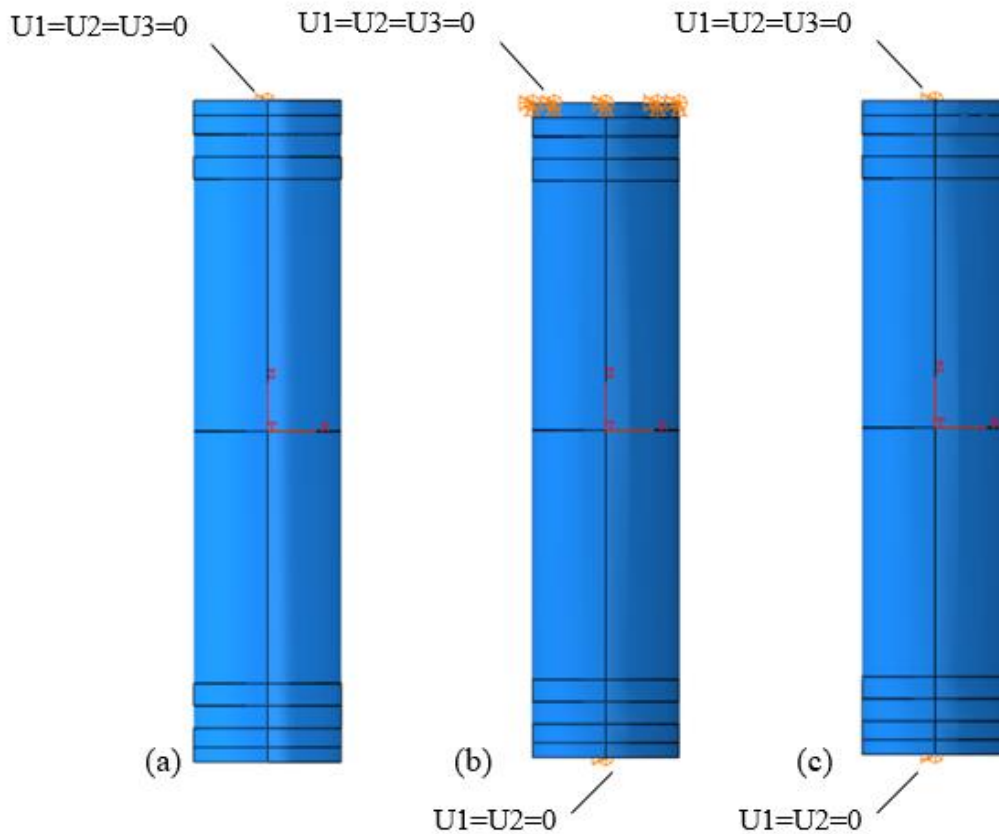
Figure 4.5 Application of the BCs on whole cylinder model
(a) Linear static analysis (b),(c) Eigenvalue and Nonlinear bucking analysis

4.1.4 Type of analysis

Linear static, eigenvalue buckling and nonlinear buckling analyses are performed in the whole cylinder model.

The linear static analysis aims at the verification of the results given by the slice model and the investigation of the effect of gravity.

Eigenvalue buckling analysis is used to estimate the theoretical strength of the structure which is idealized as elastic. Eigenvalue buckling factors are computed from constraints and loading conditions. The buckling factors of the first six modeshapes are requested in this study. The lowest of the calculated ones and the corresponding modeshape is the critical. Buckling loads are then derived, each associated with a buckled mode shape which represents the shape a structure takes under buckling. In a real structure, imperfections and nonlinear behavior keep the system from achieving this theoretical buckling strength, leading eigenvalue analysis to usually over-predict buckling load.

Nonlinear buckling analysis provides greater accuracy than elastic formulation. It consists of two phases. The first is the generation of the geometric imperfections and the second is the nonlinear run. In order to generate the initial imperfections, the eigenvalue buckling analysis previous run is utilized. Then, the eigenvalue buckling analysis modeshapes are

90

expanded and output to the results file. The deformed shape of the buckled cylinder that corresponds to the minimum eigenvalue buckling load, scaled by a specific magnitude, is then used as the cylinder with the initial geometric imperfections, safely assuming that the cylinder is going to buckle following this predicted mode shape. Although the graphical user interface (GUI) of ABAQUS software is used in this study, the introduction of initial imperfection can only be performed through the code of the nonlinear buckling analysis. In detail, the following lines are added in the code introducing the displacement from the eigenvalue buckling analysis and updating the geometry of the finite element model to the deformed configuration.

```
…
*IMPERFECTION, FILE=results_file, STEP=step
Data lines specifying the mode number and its associated scale factor
…
```

It is also possible to combine the deformed shapes (eigenmodes) of several eigenvalues to generate the initial imperfections pattern. The size of the geometric imperfections depends on the application and is expressed in this study as a ratio to the cylinder's diameter. The effect of the size of the initial imperfections has been investigated and will be discussed in section 4.2.3.4. In this study, the chosen size of the maximum imperfection is 1% of the external diameter (D_{ext}) of the cylinder, i.e. 2mm. ABAQUS software defines as scale factor the desired maximum imperfection divided by the maximum displacement magnitude of the desired eigenvalue modeshape, both expressed in the same unit. All displacements of the critical mode-shape of the eigenvalue buckling analysis are multiplied by the parameter scale factor, generating this way the desired geometric imperfections.

After the generation of the geometric imperfections, the nonlinear static analysis is run. It is clarified that the internal pressure is already applied in a linear static step before the incremental application of the external pressure for a better representation of real-life conditions. The final Time is set equal to 1 and every increment is the same percentage of the maximum applied external pressure. Automatic time stepping is used because it reduces the size of increments in case of lack of convergence and thus increases the accuracy of the results. The chosen parameters of the analysis are stated in Table 4.1.

Table 4.1 Nonlinear buckling analysis parameters

Nonlinear geometry option: activated			
Max No of increments	Size of increments		
	Initial	Min	Max
50	0.025	0.001	0.025

4.2 Results of the full cylindrical model

This section of the report presents the results obtained from the different type of analysis using the full cylindrical model.

4.2.1 Mesh Convergence Study

The mesh definition of the models focuses on adhesive joint area and is created as similar as possible with the corresponding mesh of the slice model. The mesh convergence study (MCS) is performed regarding three factors: the number of elements across the thickness of the adhesive, the number of elements along the axial part of the adhesive and the number of elements along 30mm below end of the adhesive joint, which are illustrated in Figure 4.6.
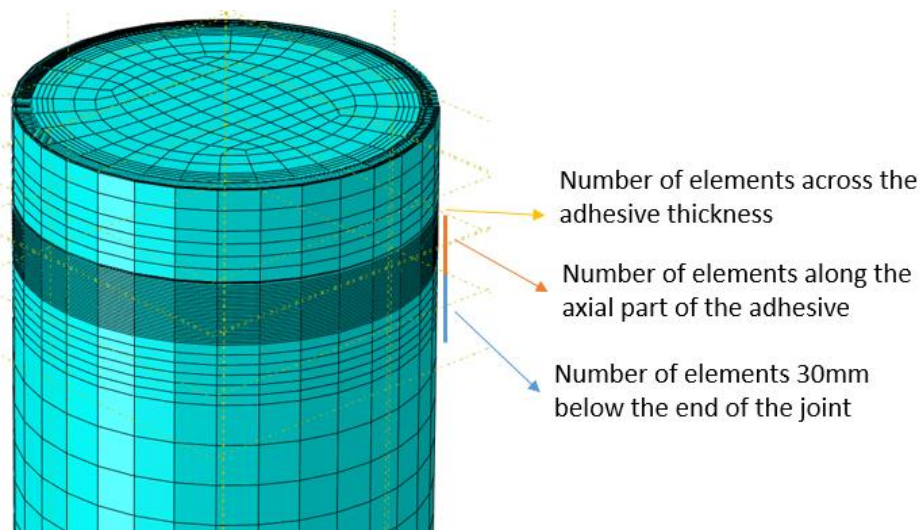

Figure 4.6 Visualization of the three factors considered in MCS

Seven different mesh patterns are checked. The first mesh consists of 6 elements across the adhesive thickness, 30 elements along the axial part of the adhesive and 6 elements along 30mm below the end of the joint. The second mesh consists of 10 elements across the adhesive thickness, 30 elements along the axial part of the adhesive and 6 elements along 30mm below the end of the joint. The third mesh consists of 6 elements across the adhesive thickness, 45 elements along the axial part of the adhesive and 6 elements along 30mm below the end of the joint. The fourth mesh consists of 6 elements across the adhesive thickness, 60 elements along the axial part of the adhesive and 6 elements along 30mm below the end of the joint. The fifth mesh consists of 6 elements across the adhesive thickness, 30 elements along the axial part of the adhesive and 12 elements along 30mm below the end of the joint. The sixth mesh consists of 6 elements across the adhesive thickness, 30 elements along the axial part of the adhesive and 18 elements along 30mm below the end of the joint. The seventh mesh consists of 6 elements across the adhesive thickness, 30 elements along the axial part of the adhesive and gradual mesh size (starting from 0.8mm length of elements in contact with the joint) along 30mm below the end of the joint. All the above mentioned mesh patterns have 1 element per cylinder's ply whereas the cylinder has 20 plies in total.

The comparison of the results considers four representative nodes of the vessel, which are visualized in Figure 4.7. Node 1 is situated at the mid-length of the cylinder. Node 2 is situated at the central point of the End-cap 2. Node 3 is situated in the adhesive-composite interface at the end of the joint. Because of the mismatch of properties between substrate and adhesive, a singular stress field especially near the edge of the adhesive layer is expected. Node 4 is situated at the internal corner of the end-cap where high Von-Mises stresses are developed.
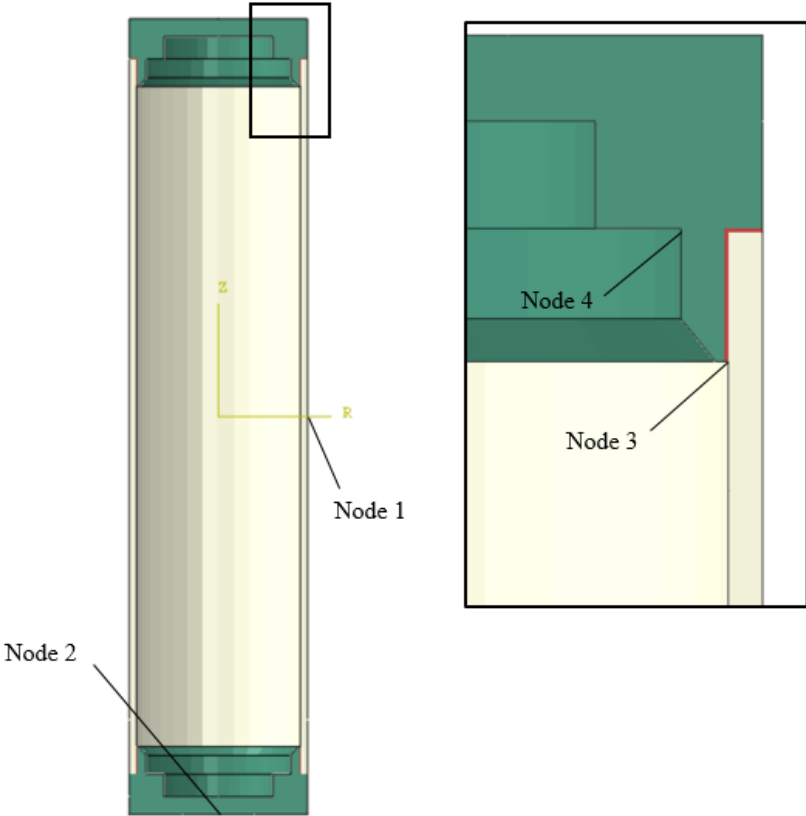

Figure 4.7 Location of the nodes used in MCS shown in the longitudinal cross section of vessel

Keeping in mind that the stress singularities and stress concentrations are intensified using finer mesh, the first results enlisted in Table 4.2 concern the axial (U1) and radial (U3) displacements. The difference between the finer (6/adh-30/overlap-gradual/cyl) and the coarser (6/adh-30/overlap-6/cyl) mesh is 1.25% concerning the radial displacement of Node 1, 5% concerning the radial and 2% concerning the radial displacement of Node 3 and negligible concerning the axial displacement of Node 2.

Table 4.2 Mesh convergence study- displacements comparison (in mm)

Mesh description	Node 1 (Composite cylinder) U1	Node 3 (Adhesive) U1	Node 3 (Adhesive) U3	Node 2 (End-cap) U3
6/adh-30/overlap-6/cyl	-0.080	-0.020	-0.048	-0.214
10/adh-30/overalp-6/cyl	-0.079	-0.020	-0.048	-0.214
6/adh-45/overalp-6/cyl	-0.080	-0.020	-0.048	-0.212
6/adh-60/overlap-6/cyl	-0.078	-0.020	-0.047	-0.212
6/adh-30/overlap-12/cyl	-0.080	-0.019	-0.048	-0.214
6/adh-30/overlap-18/cyl	-0.078	-0.019	-0.048	-0.214
6/adh-30/overlap-gradual/cyl	-0.079	-0.019	-0.047	-0.214

Apart from the displacements, the stresses developed in representative points of the vessel are compared in Table 4.3. The stresses chosen to be compared are:
- in the composite cylinder: stress aligned with the fiber direction (Sff), perpendicular to fiber direction (Spp), normal to the ply (Snn) and the in-ply shear stress (Sfp)
- in the adhesive the stress in radial direction (S11)
- in the metal end-cap the von Mises stress (Svm).

The difference between the finer and the coarser mesh is negligible concerning the stresses developed in Node 1, approximately 0.75% concerning the peel stress developed in Node 3 and 7% concerning the Von Mises stress in Node 2. The percentage of difference regarding the all the stress values of adhesive is relatively high, which is explained from the stress concentration area around Node 3.

Table 4.3 Mesh convergence study- stresses comparison (in mm)

Mesh description	Node 1 (Composite cylinder) Sff	Spp	Snn	Sfp	Node 3 (Adhesive) S11	Node 4 (End-cap) Svm
6/adh-30/overlap-6/cyl	-70.69	-5.93	-4.78	1.74	-30.06	78.39
10/adh-30/overalp-6/cyl	-70.69	-5.93	-4.78	1.74	-31.76	79.98
6/adh-45/overalp-6/cyl	-70.69	-5.93	-4.78	1.74	-35.31	84.65
6/adh-60/overlap-6/cyl	-70.69	-5.93	-4.78	1.74	-39.48	84.7
6/adh-30/overlap-12/cyl	-70.69	-5.93	-4.78	1.74	-28.35	78.26
6/adh-30/overlap-18/cyl	-70.69	-5.93	-4.78	1.74	-27.6	78.21
6/adh-30/overlap-gradual/cyl	-70.69	-5.93	-4.78	1.74	-30.29	84.51

As it was proved in the previous MCS, when the stresses in a stress concentration zone do not converge it is better to judge based on the displacement results. It is decided to continue the study using the mesh consisting of 6 elements across the adhesive thickness, 30 elements along the axial part of adhesive and gradual mesh size starting from 0.8mm length of elements along 30mm below the end of the joint because it is the closer pattern to the mesh applied in the slice model.

4.2.2 Investigation of the effect of gravity

This part of the study investigates the effect of gravity on the pressure vessel, assuming that the End-cap 1 is clamped as shown in Figure 4.8. Gravity is applied introducing the value of gravitational acceleration perpendicularly to the axial direction as loading conditions. ABAQUS requires also density values for the components. The ones used in the model are found in the literature and presented in the Table 4.4.
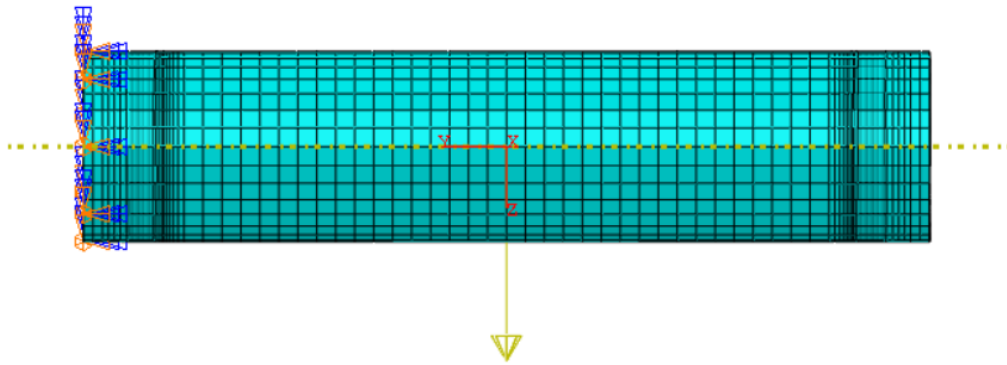

Figure 4.8 Loading and boundary conditions

Table 4.4 Density values

Density [kg/cm³]		
Aluminum 7075-T6	24K T700 Epoxy CFRP [±15/(±55)9]	Hysol epoxy EA9394
2710	1500	1380

The results of the gravity analysis show that the Von Mises criterion applied on the metal part equals to 0.0008 and on the mid-plane of the adhesive layer equals to 0.006. As for the interfaces, the maximum quadratic criterion value is 0.007. The governing Hashin criterion on the composite cylinder reaches the value of 0.003. All the criteria values are extremely lower than the required upper limit (0.45) and it is concluded that the gravity does not threaten the structure. The locations of the maximum stress values are shown in Figure 4.9.
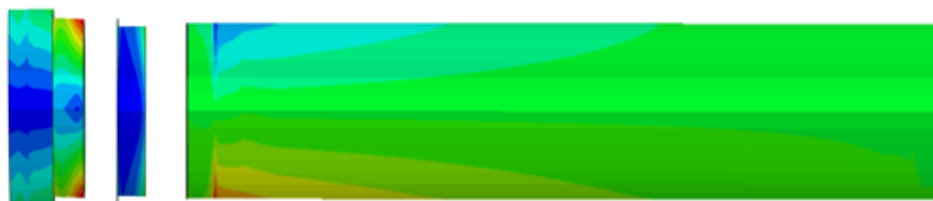

Figure 4.9 Stress distribution on every component of the structure

4.2.3 Analysis of results

The results of the whole cylinder model are discussed starting from the linear static analysis and moving on to eigenvalue and nonlinear buckling analysis, in order to reach conclusions for the final design.

4.2.3.1 Results of linear static analysis

Both DC No 3a and No 3b are examined in linear static analysis and compared in order to choose the better one in terms of strength and functionality. Figure 4.10 visualizes the radial displacement results of the longitudinal cross sections of the two models. The chromatic difference in the circumferential area of the adhesive joint is visible, the radial displacements (U1) of DC No 3a are lower than DC No 3b, fact explained by the higher bending stiffness of the thicker ring of the former. The maximum radial displacement is expected to be in the mid-length of the cylinder in both cases and so it is.
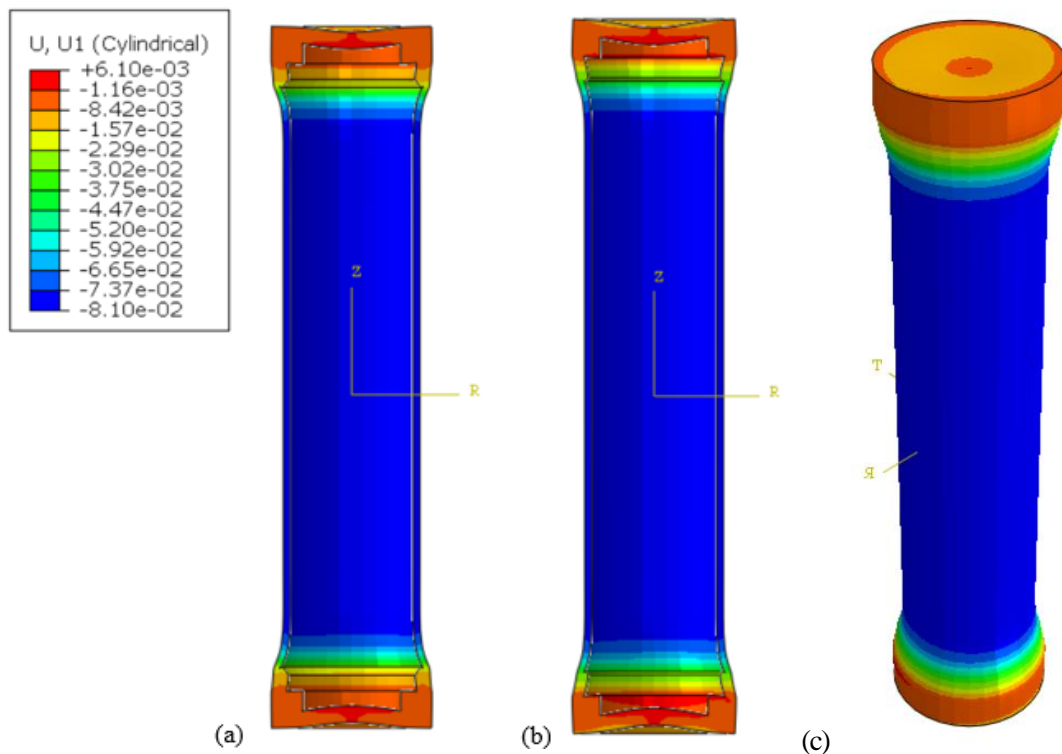

Figure 4.10 Contour plot of radial displacement distribution of (a) cross section of DC No3a (b) cross section of DC No3b (c) isometric view of DC No3b
Deformed shape (deformation scale factor: 200)

Metal part

The metal part of the models present stress concentrations at the edges, where abrupt geometric changes occur, exactly in the same locations as the corresponding slice model (Figure 4.11). The maximum Von Mises stress value, developed in DCs No 3a and No 3b, is 84.5 MPa and 142.5 MPa, respectively. Applying the von Mises criterion considering $\sigma_Y = 480$ MPa as indicated in Table 2.7, the values equal to 0.176 and 0.297 which are lower than the required upper bound (0.45).
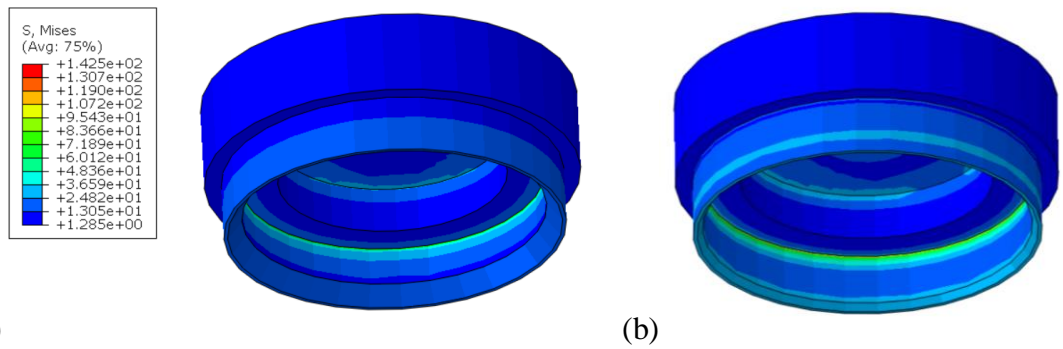
Figure 4.11 Contour plot of von Mises stress distribution on the end-cap of (a) DC No3a (b) DC No3b

Adhesive layer

Figure 4.12 shows that the radial stress field is more intense at the end of the adhesive joint where the compressive stresses reach their maximum in both design concepts. The axial part of the adhesive develops higher stress values compared to the radial one, so it is interesting to check the criterion value distribution along the axial adhesive part in corresponding paths of the two models. Three paths for each model are examined, in the metal-adhesive interface, in the adhesive mid-plane and in the adhesive-composite interface. Their position is pointed out with a red line in Figure 4.12 (b). Figure 4.13 displays the quadratic criterion results in the interfaces and the von Mises criterion result in the mid-plane of the adhesive. The results obtained from DC No 3a are illustrated with a continuous line whereas the results obtained from DC No 3b are illustrated with a dashed line enabling the comparison between the two models. It seems interesting that the stresses developed in DC No 3a near the end of the joint (0mm on x-axis of Figure 4.13) are higher but while moving towards the end of the path (30mm on x-axis of Figure 4.13) become lower than the stresses developed in DC No 3b.
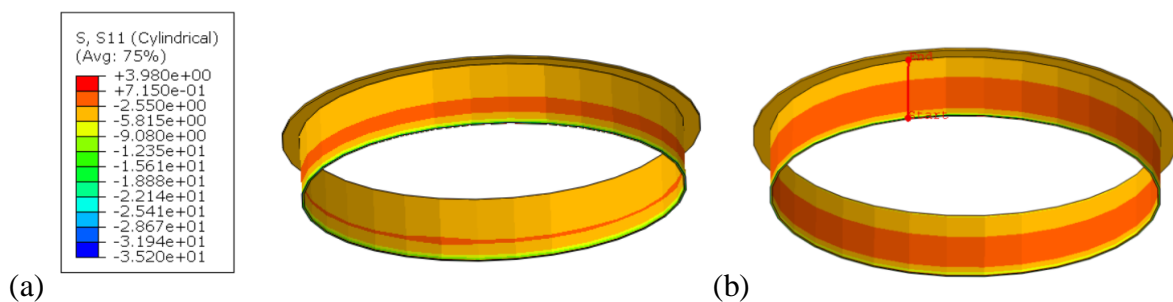

Figure 4.12 Contour plot of radial stress distribution of adhesive layer (a) DC No 3a (b) DC No 3b
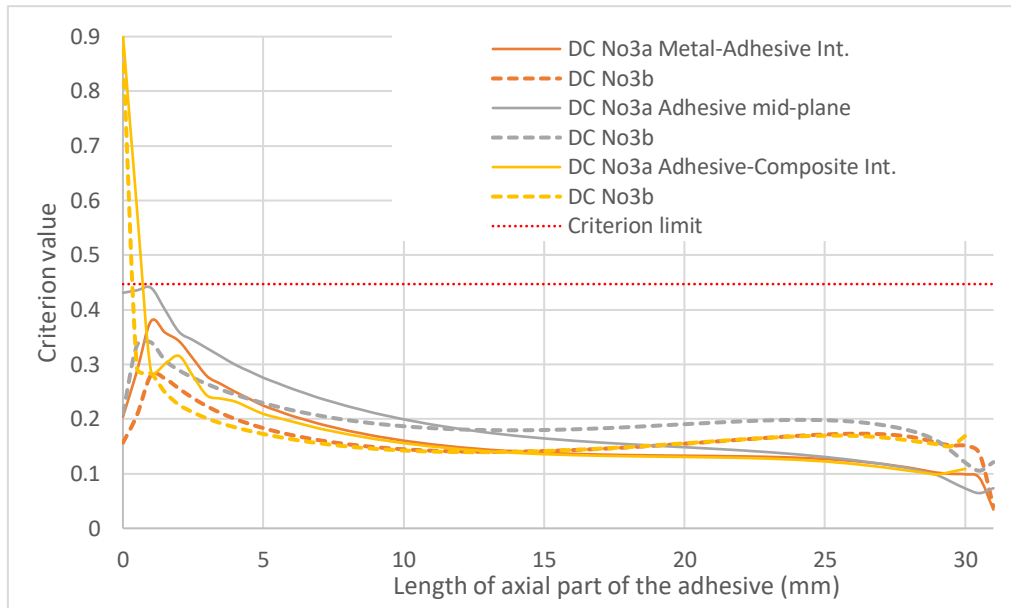
Deformed shape (deformation scale factor: 200)

Figure 4.13 Criterion value along the axial part of adhesive layer
(Continuous line: DC No 3a, Dashed line: DC No 3b)

Composite cylinder

Hashin criterion is applied in order to assess the structural behavior of the whole cylinder. The Fiber and the Out of plane Hashin criteria values satisfy the maximum permissible criterion value (0.45), hence, there is no need to be presented. The case is different with the Matrix Hashin criterion which exceeds the required limit. For that reason, it is considered the governing criterion. Figure 4.14 shows the contour plot of the governing criterion distribution (Matrix Hashin). Additionally, Figure 4.15 shows the through thickness Matrix Hashin criterion values of the two models. The position of the path used is shown with a red line in Figure 4.14 and corresponds to the area of adhesive joint end. It is observed that the higher values are localized in Ply 1 (in the interface with Ply 2) in the area of the end of the adhesive joint. Based on Matrix Hashin criterion, there is risk of matrix failure, whereas Fiber and Out of plane Hashin criteria values are significantly lower than the limit.
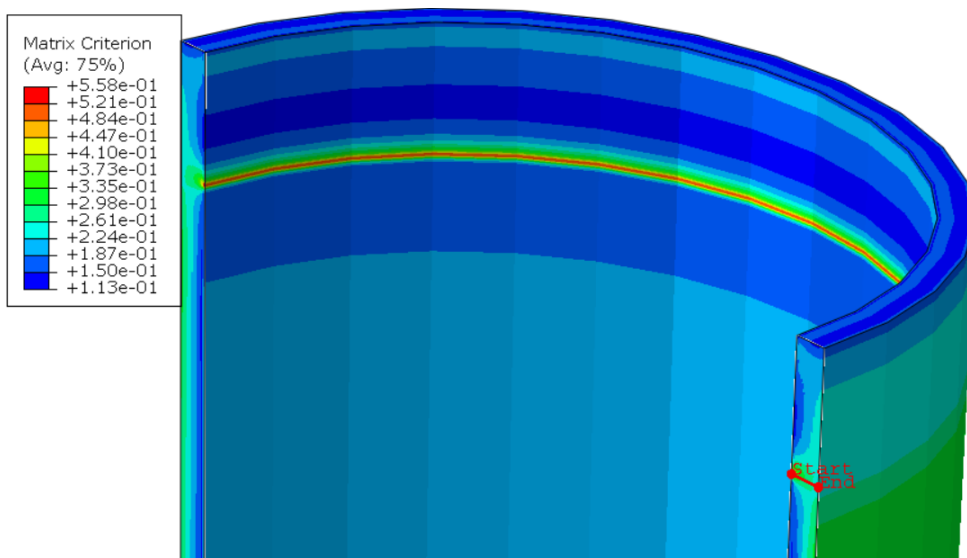

Figure 4.14 Contour plot of Matrix Hashin criterion distribution of the cylinder DC No 3b
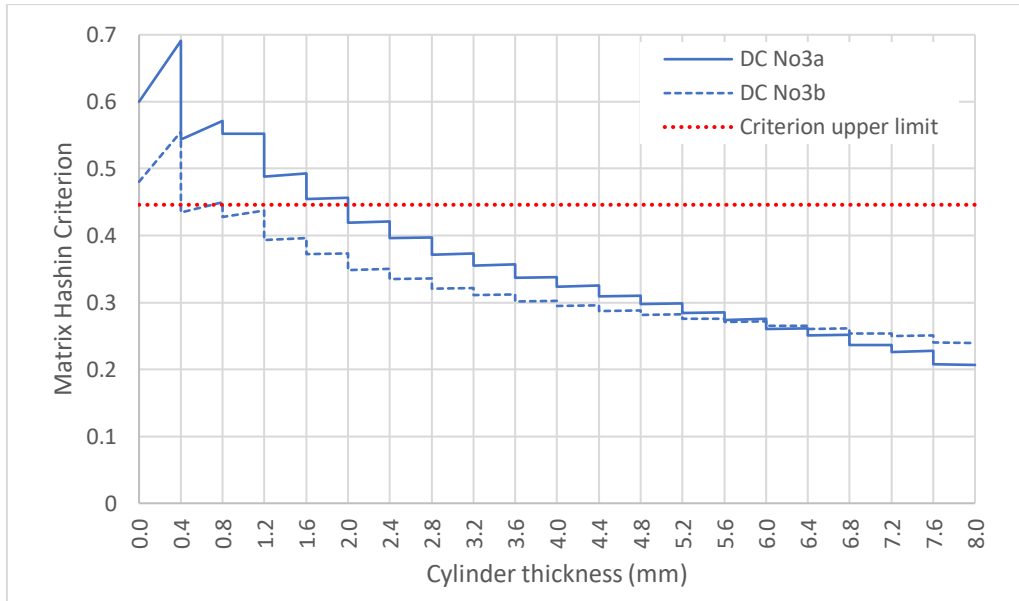
Figure 4.15 Matrix Hashin criterion value across the cylinder thickness
(Continuous line: DC No 3a, Dotted line: DC No 3b)

To sum up, DC No 3b is a very promising concept. It develops 40% lower Von Mises stresses in the metal part, 20%-25% lower stresses in the adhesive layer and results in approx. 17% lower Hashin criterion value in comparison with DC No3a. It is clarified that the eigenvalue and nonlinear buckling analysis will be conducted using the DC No3b in order to examine its mechanical behavior and optimize the geometry based on a more representative type of analysis. However, the verification study will be conducted using the DC No3a because the available slice model with a similar mesh pattern belongs to DC No3a.

4.2.3.2 Verification study

In this section, the results obtained from the slice model of optimized DC NO 3a (CFRP: 24K T700 epoxy, stacking sequence: $[\pm15/(\pm55)_9]$) are compared with the results calculated from the corresponding whole cylinder model. It is safely assumed that the whole cylinder model is more accurate than the slice model. The objective of this section is to conclude whether the results taken by the slice model were reliable.

The two models are developed with the following similarities: geometry, material properties and orientations, type of element, loading conditions and type of analysis. The differences concern the boundary conditions (section 3.1.3 for the slice model and section 4.1.3 for the whole cylinder model) and the mesh pattern. In particular, the slice model with the least fine mesh (consisting of 6 elements across adhesive thickness and 1 element per cylinder's ply, described in section 3.2.1) is used for the runs since it approaches more the relatively coarse mesh pattern of the whole cylinder.

The obtained results and the maximum difference between the corresponding values of every component are quantified in Table 4.5. The metal part presents the higher percentage of difference, which is expected because of the coarser mesh in that area of the full cylinder model. The adhesive layer presents negligible differences. The composite cylinder presents the

maximum difference in Out of plane criterion. It is observed that the slice model tends to give higher values than the full cylindrical one, which is explained probably by the more restrictive boundary conditions of the slice model. The application of restrictive boundary conditions results in reducing the displacements and increasing the stresses.

In order to assess it thoroughly, it would be interesting to check the through-thickness distribution of the typical stress components of the two models starting from the point with the higher compressive stresses. Note that this point was located in equivalent areas (internal ply at the end of adhesive joint) of the slice and full cylindrical model. The path used for the plot of stress components of the full cylindrical model is depicted in Figure 4.14, whereas the path used for the plot of stress components of the sliced model is chosen in corresponding way. In Figure 4.16 it is presented schematically that the stresses developed in composite cylinder through thickness in the area of the end of adhesive joint are almost the same. Moreover, the pair of [±15] is represented with an increase of the compressive stresses aligned with the fibers.

Plotting the through thickness distribution of the stress components in the mid-length of the cylinder (Figure 4.17) presents slight differences in Sff. This is probably owed to different mesh size of the elements situated in the mid-length of the cylinder between the two cases. Additionally, different boundary conditions (BC) are used in the two models. It is reminded that the sliced model has symmetric BC in the position of the transverse mid-plane of symmetry of the full cylinder, which has an impact on the results.

It is concluded that the slice model is effective in terms of computational cost and capable to replace reliably a full cylindrical model under specific conditions and if buckling is not considered. These conditions include that the mesh pattern should be similar with the corresponding full cylindrical model and the values taken into account from the slice model should be located near the longitudinal mid-plane of symmetry to avoid the effect of side boundary conditions.

Table 4.5 Maximum % differences between the results of slice model and whole cylinder model

| | Run time (min) | Metal part | | | Adhesive layer | | | | Composite cylinder | | | |
		Svm_max (MPa)	% Diff.	Quadratic Metal-Adhesive Int.	Von Mises Adhesive Mid-plane	Quadratic Adhesive-composite Int.	Max % Diff.	Hashin Fiber value	Hashin Matrix value	Hashin Out of plane value	Max % Diff.
Slice model	1	104.02	18.8	0.162	0.152	0.169	2.4	0.074	0.732	0.230	6.5
Whole cylinder model	12	84.51		0.164	0.148	0.167		0.073	0.695	0.215	
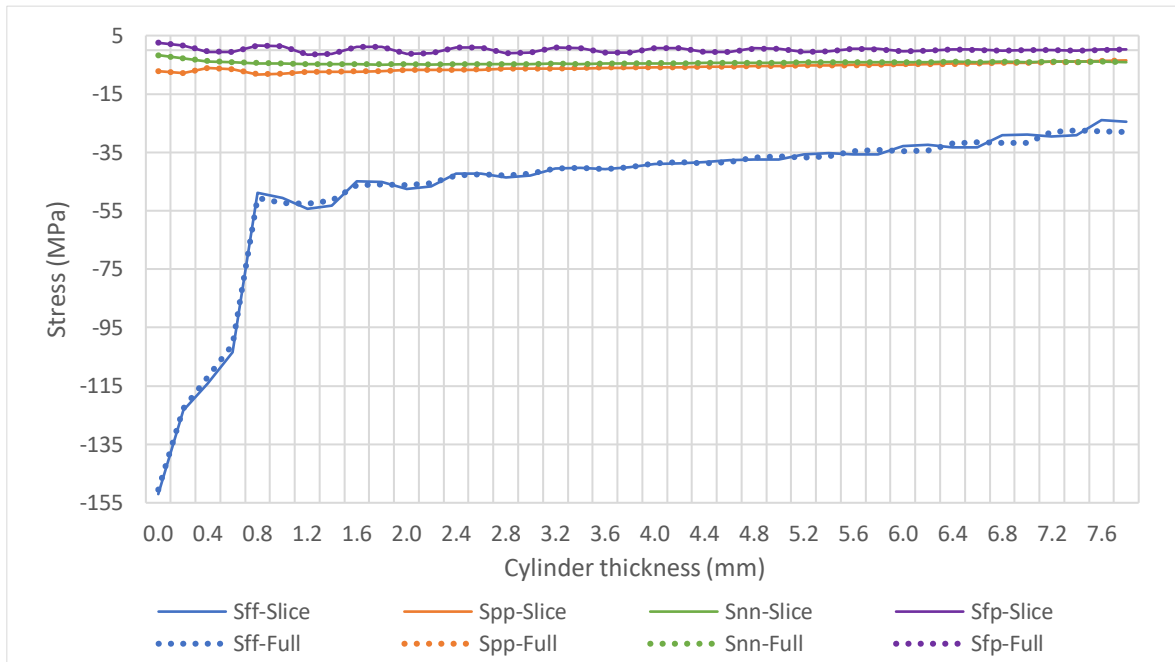
Figure 4.16 Through thickness stress distribution in the end of adhesive joint
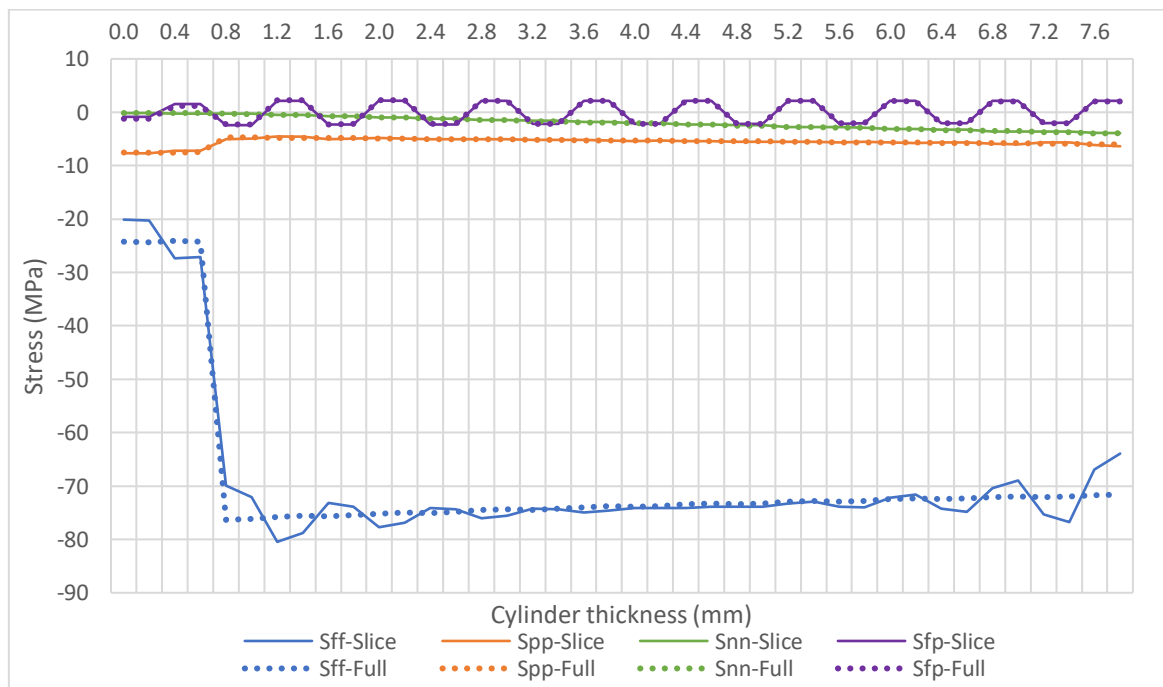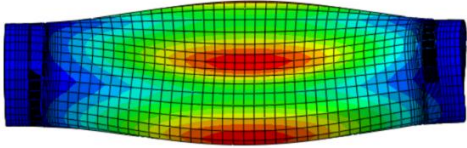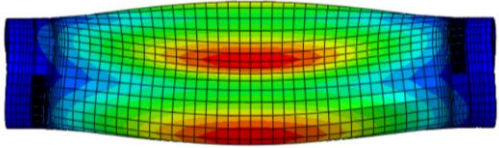(Continuous line: slice model, Dotted line: full cylindrical model)

Figure 4.17 Through thickness stress distribution in the mid-length of cylinder
(Continuous line: slice model, Dotted line: full cylindrical model)

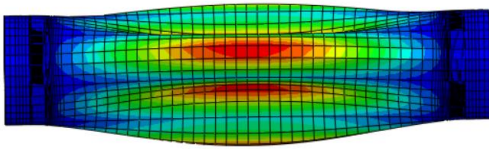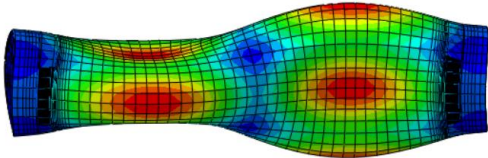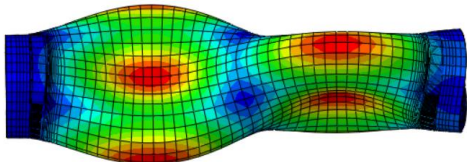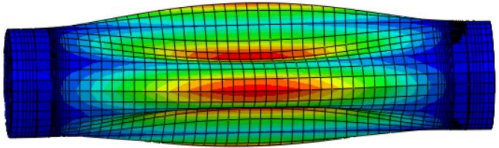## 4.2.3.3 Results of eigenvalue buckling analysis

The full cylinder model of DC No 3b enables an eigenvalue buckling analysis which will be useful also in the next step of the study. As it has been mentioned in section 4.1.3, two BC sets are tested. The results are listed in Table 4.6. The buckling loads are the product of the applied pressure multiplied by the eigenvalue buckling factor. All eigenvalue buckling factors are double which implies that the structure can buckle at the same load with a similar modeshape. After taking a closer look, they are exactly the same in terms of magnitude and displacements but they are rotated around the axial direction.

Table 4.6 Results of the eigenvalue buckling analysis

	BC set 1	BC Set 2
	End-cap1: circumference pinned Endcap2: central point with all DOFs fixed, except axial translation	End-cap1: central point pinned Endcap2: central point with all DOFs fixed, except axial translation
Buckling factor | modeshape 1	2.92 | 2.1	2.80 | 2.1
Buckling factor | modeshape 2	2.92 | 2.1	2.80 | 2.1
Deformed shape		
Buckling factor | modeshape 3	6.17 | 3.1	5.88 | 2.2
Buckling factor | modeshape 4	6.17 | 3.1	5.88 | 2.2
Deformed shape		
Buckling factor | modeshape 5	6.54 | 2.2	6.17 | 3.1
Buckling factor | modeshape 6	6.54 | 2.2	6.17 | 3.1
Deformed shape		

Comparing the two BC sets, the difference between the critical buckling factor is slight (4%). As it is expected, the more restrictive BCs present higher buckling factor, whereas both satisfy the buckling SF=1.91 (stated in Table 2.4). Additionally, the deformed shape of the critical buckling factor in case of BC set 1 is not symmetric with respect to the transverse plane of symmetry and the End-cap 1 keeps its flat shape. It is decided to proceed to the nonlinear

buckling analysis using the BC set 2 which, even if it gives lower buckling factors, is closer to actual realistic operation of the vessel.

4.2.3.4 Results of nonlinear buckling analysis

The nonlinear buckling analysis is conducted using the DC No 3b under higher external pressure than the nominal one (4 MPa) in order to investigate the failure pressure of the vessel and the behavior of the fibers. It is decided to run the model for 16 MPa maximum external pressure and observe which is the failure pressure for the different components of the structure. The FE analysis stops when the external pressure reaches the value of 7.638 MPa. This identifies that under this loading condition the structure had become unstable and convergence cannot be reached using the minimum load increment size (0.001).

Figure 4.18 shows the Hashin criteria and von Mises stress values evolution as a function of the incrementally applied external pressure. The first criterion which reaches the maximum permissible criterion value (0.45) is the Matrix Hashin at the adhesive joint end under external pressure of 3 MPa. This figure shows also that, when the external pressure reaches and surpasses 4.4 MPa, the higher values of Hashin Matrix criterion move to the internal ply of a mid-length crest from the adhesive joint end. As for the other Hashin criteria, the delamination risk begins for external pressure of 7 MPa and fiber failure risk is not predicted according to the calculations. Regarding the von Mises stress criterion values of metal parts, it seems that it exceeds the maximum permissible limit for external pressure of 4.8 MPa. It is underlined that the criterion values of the metal part probably are overestimated since they correspond to stresses developed in stress concentrations points which will be filleted in real manufacturing conditions.
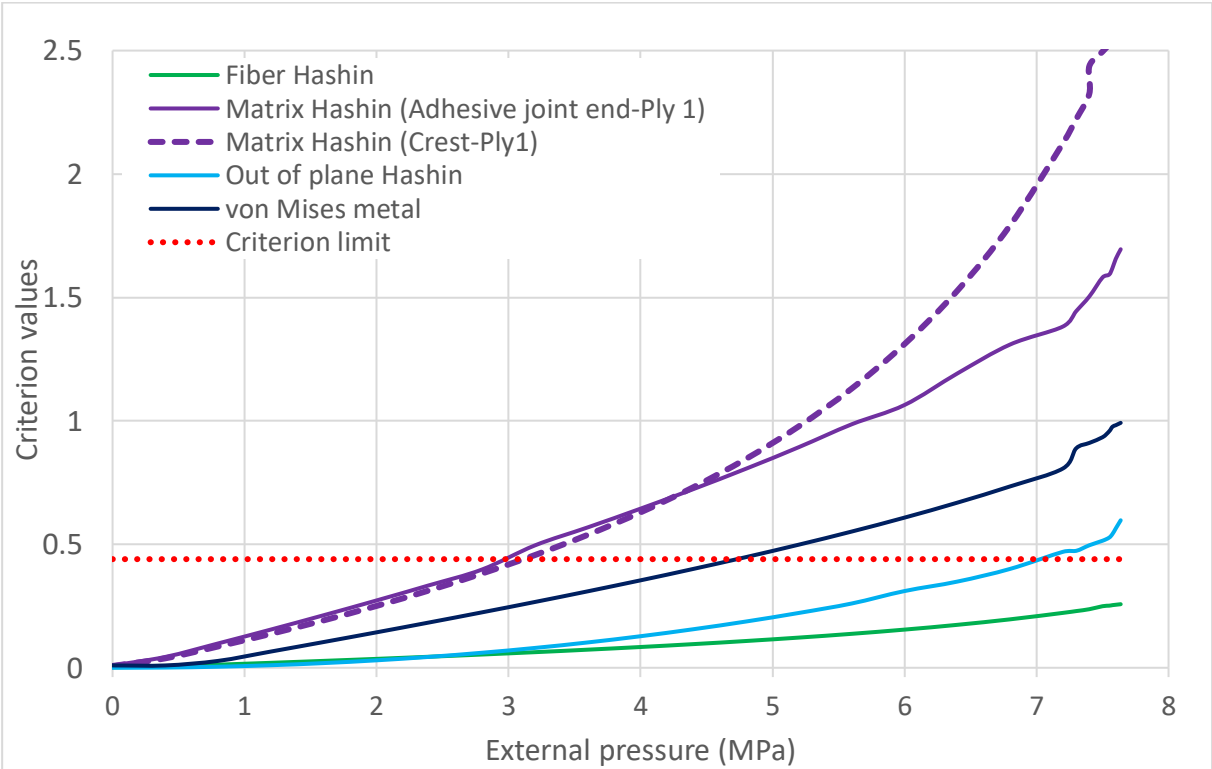

Figure 4.18 Criterion values of 8mm thick cylinder in function with the external pressure

Focusing on the results of the nominal external pressure of 4 MPa, Table 4.7 is set including the maximum criterion values and their locations. Figure 4.19 is complementary to the Table 4.7 information. It is obvious that Matrix Hashin criterion is the governing one and predicts failure in contrast with the Fiber and Out-of-plane criteria which satisfy the required limit by far. It is proved again that the "weaker" point of the structure is the end of adhesive joint where high stress concentrations occur.
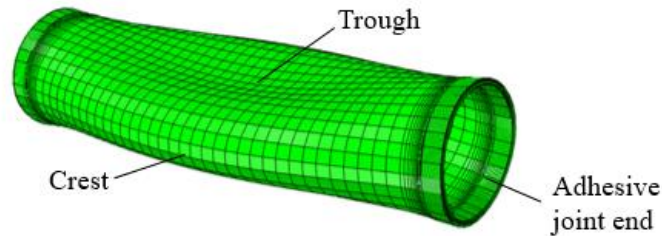

Figure 4.19 Explanatory sketch showing the locations of maximum calculated criteria values

Table 4.7 Results of nonlinear buckling analysis of the composite cylinder

External pressure 4MPa		DC No3b (CFRP: 24K T700 epoxy, stacking sequence: [±15/(±55)9])
Max Fiber Hashin	Value	0.08
	SF	12.5
	Location	Mid-length crest
	Ply	3
Max Matrix Hashin	Value	0.63
	SF	1.59
	Location	Adhesive joint end
	Ply	1
Max Out Of Plane Hashin	Value	0.12
	SF	8.33
	Location	Adhesive joint end
	Ply	1

In the framework of the nonlinear analysis, the elastic-plastic behavior of the adhesive layer is also investigated using the PE output, which gives the plastic strain components. The higher value of plastic strain for the nominal external pressure (4 MPa) is observed in the axial direction, using a cylindrical coordinate system. This value is obtained in the external edge of the radial part of the adhesive, which develops tensile stresses because of the trough of the composite cylinder, as illustrated in Figure 4.20. According to Figure 4.21, the adhesive layer begins to present plastic strain under 6 MPa external pressure.
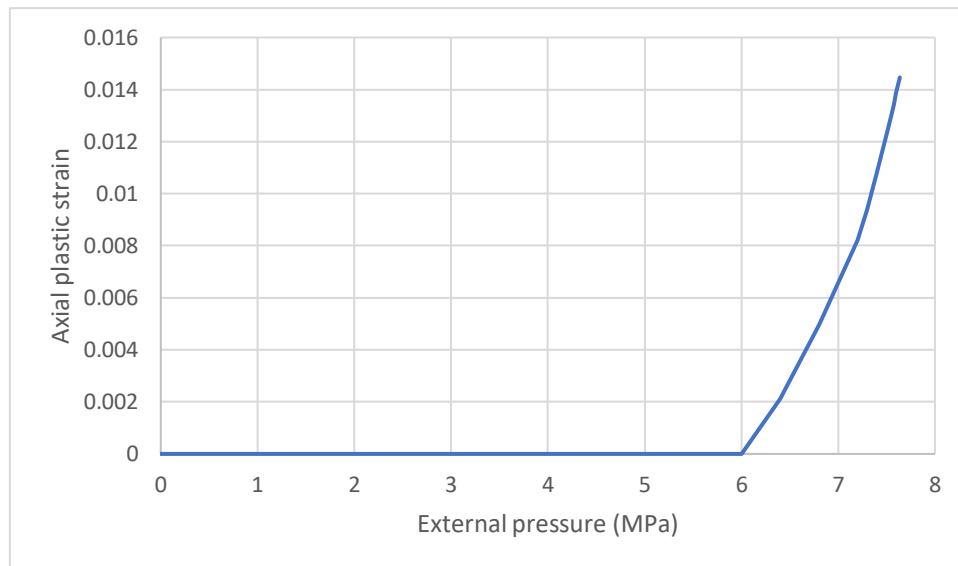
Figure 4.20 Axial plastic strain in function with the external pressure
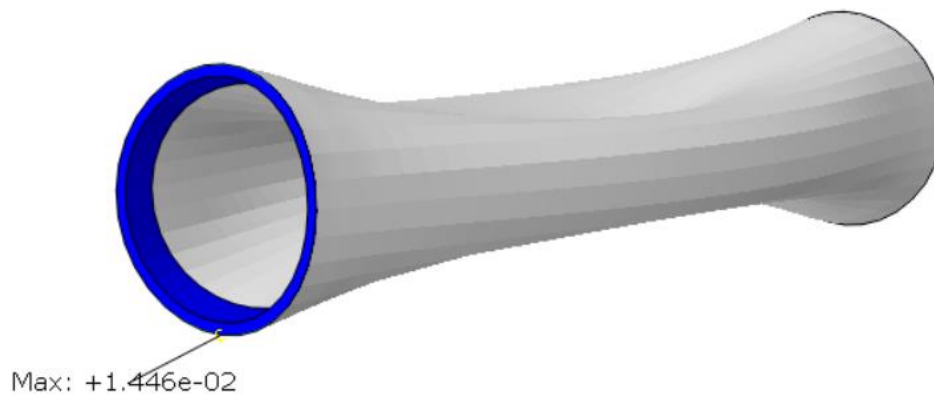

Max: +1.446e-02

Figure 4.21 Location and value of maximum axial plastic strain on the deformed shape
(Adhesive layer: blue, Composite cylinder: white)

The aim to design a pressure vessel that satisfies the criteria of every component under the nominal external pressure (4 MPa) has not been achieved so far. Given that the geometric configuration, the material properties and the stacking sequence are already optimized, the last option is the increase of cylinder thickness. A parallel study on the cylinder thickness using shell and solid elements indicated that a 50% increase of thickness gives the desirable results. Based on this study, the DC No 3b using 20 layers of $[\pm15/(\pm55)_9]$ stacking sequence and 24K T700 epoxy CFRP is now modeled with 12mm thickness keeping the external diameter constant. After the eigenvalue buckling analysis, the modeshape of the critical eigenvalue is introduced as initial imperfection for the nonlinear buckling analysis. Two magnitudes of initial imperfection are tested: 1% of the external diameter (2mm) and 0.5% of the external diameter (1mm). The results are illustrated in Figure 4.22. As it is expected, the smaller the magnitude of initial imperfection is, the lower the criterion values reach. Moreover, the Matrix Hashin criterion reaches the higher values compared to Fiber and Out of plane Hashin criteria and, hence, it is considered the governing one. All the failure criteria values, even the governing one, satisfy the maximum permissible criterion limit (0.45). Table 4.8 presents the values of the

Matrix Hashin criterion and the location where it is reached, comparing the two different magnitudes of initial imperfection. Hopefully, the solution of the DC No3b with a 12mm cylinder made of 24K T700 epoxy CFRP in combination with [±15/(±55)$_9$] stacking sequence works. It is clarified that this model predicts a safe and reliable structure under the given conditions and assumptions.
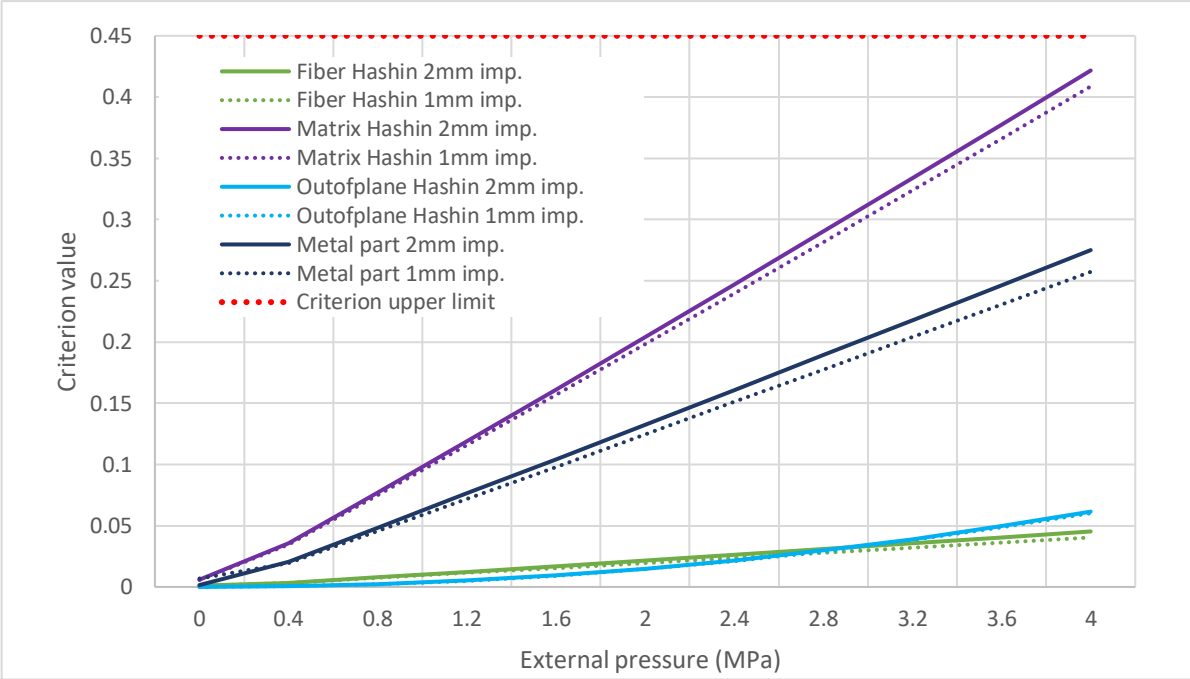
Figure 4.22 Criterion values of 12mm thick cylinder in function with the external pressure (Continuous line: 2mm imp., Dotted line: 1mm imp.)

Table 4.8 Results of nonlinear buckling analysis of the 12 mm composite cylinder regarding two different magnitudes of initial imperfection

External pressure 4MPa		DC No3b (CFRP: 24K T700 epoxy, stacking sequence: [±15/(±55)9])	
Initial imperfection		**2 mm**	**1 mm**
Max Matrix Hashin	Value	0.42	0.41
	SF	2.38	2.44
	Location	Adhesive joint end	Adhesive joint end
	Ply	1	1

CHAPTER 5

Conclusions and future work

5.1 Conclusions

After extensively discussing the finite element analysis and the structural optimization of the filament wound pressure vessel, a summary of the conclusions is made in this section.

The preliminary design concepts of the structure were set and evolved taking into account the initial technical specifications as well as design ideas from the literature. The selected design concept No 3a, No 3.1a and No 3.1b combined the best features in terms of manufacturing feasibility, functionality and structural reliability.

A FE linear static analysis was conducted in an initial stage, using a solid slice model of design concept No 3a, focusing on the adhesive joint area. The obtained results indicated no risk of failure for the metal part and the adhesive layer and high risk of matrix failure or delamination for the composite cylinder in the area where the adhesive joint ends and stress concentrations appear. This leaded to a parametric study in order to investigate the effect of different parameters and select their optimized versions in an attempt to eliminate the risk of matrix failure and delamination of the cylinder. The parameters, which were checked in this study, are stated in descending order regarding their positive effect on the strength of the adhesive joint:

- the stacking sequence with a pair of internal plies with winding angle close to the axial direction $[\pm15°/(\pm55°)_9]$,
- the use of a CFRP with higher strength limits (especially in shear strength),
- 50% thicker cylinder,
- thinner and more flexible protrusions of the metal end-cap,
- a 33% longer metal ring protrusion (this means also longer axial part of adhesive layer) and
- a 50% thinner adhesive layer.

Applying these results, the design concept No 3a was modelled with the CFRP with the higher strength and stacking sequence $[\pm15°/(\pm55°)_9]$. However, an asymmetric stress field with respect to the mid-width plane of the slice model was observed, being alarming for the reliability of the results.

The design concepts No 3.1a and No 3.1b were also modeled and analyzed using a slice model. The common feature of these two configurations was the cylinder with taper edges. The results of a parametric study showed that 25% higher taper angle gives higher structural reliability. However, it was concluded that this configuration of cylinder, apart from the special and cost-consuming manufacturing process that requires, is connected to high risk of local fiber damage at the location of the tapered edges of the cylinder.

A full cylindrical model of design concepts No 3a was developed and analyzed for the sake of a verification study. Comparing the failure criterion results for every component between this full model and the corresponding slice one, it was proved that the differences were up to 7% concerning the composite cylinder, up to 3% for the adhesive layer and approximately 20% for the metal parts. The different mesh patterns and the different boundary conditions

between the two models were responsible for these differences. The slice model was proven cost-saving and reliable under certain assumptions.

An additional model design concept (No 3b) was developed. It was a 50% thinner ring version of design concept No 3a. A comparison between the Hashin criterion values of the full cylindrical models of design concepts No 3a and No 3b showed the superiority of the latter in terms of composite cylinder strength.

A nonlinear buckling analysis was conducted using the full cylindrical model of design concept No3b in order to conclude to the final design optimization. The results showed that the metal part and the adhesive layer satisfied the maximum permissible criterion value, whereas the composite cylinder did not satisfy the maximum permissible Matrix Hashin criterion value under the nominal external pressure (4 MPa), fact that implied high risk of matrix failure. Therefore, a 50% increase of cylinder thickness was applied, leading to results that satisfied the maximum permissible criterion limit for every component of the structure.

Finally, this thesis arrived at two recommended solutions for the composite pressure vessel of the project, both regarding the design concept No 3b and stacking sequence $[\pm15°/(\pm55°)_9]$. The conservative recommended solution concerns a cylinder of 50% increased thickness (12 mm) compared to the nominal thickness, which does not present risk of failure at all. The other solution faces the results in a moderate way and regards the cylinder of the nominal thickness (8 mm) since the Fiber Hashin criterion is satisfied with a great margin of safety, even if the required upper limit of Matrix Hashin criterion is exceeded. The reason is that in the case of matrix cracking, no catastrophic failure of the cylinder is expected as the loading carrying constituents of the composite are the fibers.

5.2 Comparison with the parallel study focused on the composite cylinder

This thesis was conducted in parallel with another one which focused on the composite cylinder of the pressure vessel. The FE model of the parallel study was modelled under the same material and dimensional (concerning the cylinder) conditions. The loading and boundary conditions were similar with the ones of this study. The elements used were both shell and solid. It seems interesting to compare some representative results obtained from the parallel study with the corresponding results presented in this thesis.

In a linear static analysis of the parallel study, the Matrix and Out of plane Hashin criterion values of the initial composite cylinder (CFRP with lower strength values and stacking sequence $[(\pm55°)_{10}]$) exceeded the maximum permissible limit. The same Hashin criteria values predicted failure in this study as well using the corresponding model (design concept No 3a with CFRP with lower strength values and stacking sequence $[(\pm55°)_{10}]$.

In nonlinear buckling analysis, both studies observed that the Matrix Hashin criterion is the governing one, predicting risk of matrix failure in the case of cylinder of 8 mm thickness. The difference between the matrix criterion values of the two studies came up to 4%, while the parallel and the present studies used shell and solid elements, respectively. In addition, the two studies agree that the cylinder of 12 mm thickness is on the safe side taking into account the

Fiber and Matrix Hashin criteria values, whereas the differences between these values are 11% and 16%, respectively, while the models of both studies used solid elements. A point of difference between the two theses is the location of the predicted matrix failure in the case of the thicker cylinder. On one hand, the higher value of the Hashin Matrix criterion is situated in the adhesive joint end in the framework of this thesis. On the other hand, the higher corresponding values are situated in the mid-length crest in the context of the parallel study.

5.3 Future work

Some brief recommendations for future work are presented in this section. The material properties in this thesis are based on the literature. In real-life, the actual properties of a composite material may vary from the design ones or the properties found in literature. Therefore, the definition of real properties of composite cylinder is proposed ti be done experimentally after testing specimens. The introduction of these properties values in the existing ABAQUS models would make the study more accurate and reliable. Moreover, tools like Progressive Damage Modelling could be introduced to the finite element model in order to more accurately predict the evolution of damage and the structural behavior near catastrophic failure. This tool functions based on degradation rules, applied to the mechanical properties of each failed ply or component. The modelling of the adhesive layer using cohesive elements, with cohesive law parameters from experimental tests would also advance the study.

A step further to the study is the design and analysis of the bolted connection between the metal ring and the metal end-cap. It would be interesting to calculate the required dimensions from the perspective of the bolted connection and manage a compromise with the results of the adhesive joint study.

References

ABAQUS User Manual

Adams, R. D., & Comyn, J. (2000). Joining using adhesives. *Assembly Automation*, *20*(2), 109–117. https://doi.org/10.1108/01445150010321724

Adams, R. D., Comyn, J., & Wake, W. C. (1997). *Structural adhesive joints in engineering*. Chapman & Hall.

Adams, R.D., Harris, J.A., 1984. Strength prediction of bonded single lap joints by nonlinear finite element methods. International Journal of Adhesion and Adhesives 4: 65- 78.

Aldoumani, N., Giannetti, C., Abdallah, Z., Belblidia, F., Khodaparast, H. H., Friswell, M. I., & Sienz, J. (2020). Optimisation of the filament winding approach using a newly developed in-house uncertainty model. *Eng*, *1*(2), 122–136. https://doi.org/10.3390/eng1020008

Al-Mosawe, Alaa; Al-Mahaidi, Riadh; Zhao, Xiao-Ling (2016). Bond behaviour between CFRP laminates and steel members under different loading rates. Composite Structures, 148(), 236–251. doi:10.1016/j.compstruct.2016.04.002

Andrianakis, A. (2011). Experimental and numerical study of a steel-to-composite adhesive joint under bending moments, *Diploma Thesis*, School of Naval Architecture and Marine Engineering, National Technical University of Athens.

Anyfantis, K. (2012). Analysis and Design of Composite-to-Metal Adhesively Bonded Joints, *PhD Thesis*, School of Naval Architecture and Marine Engineering, National Technical University of Athens.

Arhant, M., Briançon, C., Burtin, C., & Davies, P. (2019). Carbon/polyamide 6 thermoplastic composite cylinders for deep sea applications. *Composite Structures*, *212*, 535–546. https://doi.org/10.1016/j.compstruct.2019.01.058

Azeem, M., Ya, H. H., Alam, M. A., Kumar, M., Stabla, P., Smolnicki, M., Gemi, L., Khan, R., Ahmed, T., Ma, Q., Sadique, M. R., Mokhtar, A. A., & Mustapha, M. (2022). Application of filament winding technology in composite pressure vessels and challenges: A Review. *Journal of Energy Storage*, *49*, 103468. https://doi.org/10.1016/j.est.2021.103468

Baishya, N., Das, R. R., & Panigrahi, S. K. (2017). Failure analysis of adhesively bonded tubular joints of laminated FRP composites subjected to combined internal pressure and torsional loading. *Journal of Adhesion Science and Technology*, *31*(19-20), 2139–2163. https://doi.org/10.1080/01694243.2017.1307498

Banea, M. D., & da Silva, L. F. (2009). Adhesively bonded joints in composite materials: An Overview. *Proceedings of the Institution of Mechanical Engineers, Part L: Journal of Materials: Design and Applications*, *223*(1), 1–18. https://doi.org/10.1243/14644207jmda219

Barbosa, N. G. C., Campilho, R. D. S. G., Silva, F. J. G. da, & Moreira, R. D. F. (2018). Comparison of different adhesively-bonded joint configurations for mechanical structures. *Procedia Manufacturing*, *17*, 721–728. https://doi.org/10.1016/j.promfg.2018.10.122

Barenblatt, G. I. (1959). The Formation of Equilibrium Cracks During Brittle Fracture. General Ideas and Hypotheses. Axially-Symmetric Cracks. *Applied Mathematics and Mechanics*, 23, pp. 622–636.

Bilalis, E. (2016). Experimental and Numerical Study of Composite Shafts, *Diploma Thesis,* School of Naval Architecture and Marine Engineering, National Technical University of Athens

Carrere, N., Martin, E., & Leguillon, D. (2015). Comparison between models based on a coupled criterion for the prediction of the failure of adhesively bonded joints. *Engineering Fracture Mechanics*, *138*, 185–201. https://doi.org/10.1016/j.engfracmech.2015.03.004

Cavalcanti, W. L., Brune, K., Noeske, M., Tserpes, K. I., Ostachowicz, W. M., & Schlag, M. (2021). *Adhesive bonding of aircraft composite structures: Non-destructive Testing and Quality Assurance Concepts*. Springer.

Chen, N.-Z., Sun, H.-H., & Guedes Soares, C. (2003). Reliability Analysis of a ship hull in composite material. *Composite Structures*, *62*(1), 59–66. https://doi.org/10.1016/s0263-8223(03)00084-9

Cornetti, P., Pugno, N., Carpinteri, A., Taylor, D. (2006). A Coupled Stress and Energy Criterion within Finite Fracture Mechanics. In: Gdoutos, E.E. (eds) Fracture of Nano and Engineering Materials and Structures. Springer, Dordrecht. https://doi.org/10.1007/1-4020-4972-2_549

Crocombe, A.D., 1989. Global yielding as a failure criteria for bonded joints. International Journal of Adhesion and Adhesives 9: 145- 153.

da Silva, L. F., Critchlow, G. W., & Figueiredo, M. A. (2008). Parametric study of adhesively bonded single lap joints by the Taguchi method. *Journal of Adhesion Science and Technology*, *22*(13), 1477–1494. https://doi.org/10.1163/156856108x309585

Das, R. R., & Pradhan, B. (2010). Adhesion failure analyses of bonded tubular single lap joints in laminated fibre reinforced plastic composites. *International Journal of Adhesion and Adhesives*, *30*(6), 425–438. https://doi.org/10.1016/j.ijadhadh.2010.02.008

Davies, P. (2016). Behavior of marine composite materials under Deep Submergence. *Marine Applications of Advanced Fibre-Reinforced Composites*, 125–145. https://doi.org/10.1016/b978-1-78242-250-1.00006-5

Delzendehrooy, F., Akhavan-Safar, A., Barbosa, A. Q., Beygi, R., Cardoso, D., Carbas, R. J. C., Marques, E. A. S., & da Silva, L. F. M. (2022). A comprehensive review on structural joining techniques in the Marine Industry. *Composite Structures*, *289*, 115490. https://doi.org/10.1016/j.compstruct.2022.115490

Dugdale, D. S. (1960). Yielding of Steel Sheets Containing Slits. *Mechanics and Physics of Solids*, 8, pp. 100–104.

Fors, F. (2010). Analysis of metal to composite adhesive joints in space applications, *Diploma Thesis*, School of Mechanical Engineering, Institute of Technology at Linköping University, Sweden

Gacoin, A., Lestriez, P., Assih, J., Objois, A., & Delmas, Y. (2009). Comparison between experimental and numerical study of the adhesively bonded scarf joint and double scarf joint: Influence of internal singularity created by geometry of the double scarf joint on the damage evolution. *International Journal of Adhesion and Adhesives*, 29(5), 572–579. doi:10.1016/j.ijadhadh.2009.01.006

Griffith, A. A. (1921). The phenomenon of rupture and flow in solids. Philosophical Transactions of the Royal Society. 221:163-198

Hashin, Z. (1980). Failure criteria for Unidirectional Fiber Composites. *Journal of Applied Mechanics, 47,* 329-334

Ji, G., Ouyang, Z., Li, G., Ibekwe, S., Pang, S.S., 2010. Effects of adhesive thickness on global and local Mode-I interfacial fracture of bonded joints. International Journal of Solids and Structures 47: 2445- 2458

Khosravani, M. R., Soltani, P., & Reinicke, T. (2023). Effects of steps on the load bearing capacity of 3D-printed single lap joints. *Journal of Materials Research and Technology*, *23*, 1834–1847. https://doi.org/10.1016/j.jmrt.2023.01.032

Kim, J. K., Lee, D. G., & Cho, D. H. (2001). Investigation of adhesively bonded joints for composite propeller shafts. *Journal of Composite Materials*, *35*(11), 999–1021. https://doi.org/10.1106/j5qd-b843-qexc-18eb

Le Pavic, J., Bonnemains, T., Lolive, É., Stamoulis, G., Silva, D. D., & Thévenet, D. (2020). Failure load prediction of a tubular bonded structures using a coupled criterion.

Theoretical and Applied Fracture Mechanics, *108*, 102531. https://doi.org/10.1016/j.tafmec.2020.102531

Meschini, A., Ridolfi, A., Gelli, J., Pagliai, M., & Rindi, A. (2019). Pressure hull design methods for unmanned underwater vehicles. *Journal of Marine Science and Engineering*, *7*(11), 382. https://doi.org/10.3390/jmse7110382

Monteiro, J. P., Campilho, R. D., Marques, E. A., & da Silva, L. F. (2015). Experimental estimation of the mechanical and fracture properties of a new epoxy adhesive. *Applied Adhesion Science*, *3*(1). https://doi.org/10.1186/s40563-015-0056-y

Moon, C.-J., Kim, I.-H., Choi, B.-H., Kweon, J.-H., & Choi, J.-H. (2010). Buckling of filament-wound composite cylinders subjected to hydrostatic pressure for underwater vehicle applications. *Composite Structures*, *92*(9), 2241–2251. https://doi.org/10.1016/j.compstruct.2009.08.005

de Morais, A. B., Pereira, A. B., Teixeira, J. P., & Cavaleiro, N. C. (2007). Strength of epoxy adhesive-bonded stainless-steel joints. *International Journal of Adhesion and Adhesives*, *27*(8), 679–686. https://doi.org/10.1016/j.ijadhadh.2007.02.002

Mouritz, A. P., Gellert, E., Burchill, P., & Challis, K. (2001). Review of Advanced Composite Structures for naval ships and submarines. *Composite Structures*, *53*(1), 21–42. https://doi.org/10.1016/s0263-8223(00)00175-6

Newhouse, N. L., Rawls, G. B., Rana, M. D., Shelley, B. F., & Gorman, M. R. (2010). Development of ASME section X code rules for high pressure composite hydrogen pressure vessels with non-load sharing liners. *ASME 2010 Pressure Vessels and Piping Conference: Volume 1*. https://doi.org/10.1115/pvp2010-25349

Ojalvo, I.U., Eidinoff, H.L. (1978). Bond thickness effects upon stresses in in single-lap adhesive joints. Journal of the American Institute of Aeronautics and Astronautics 16, 204-211.

Omairey, S., Jayasree, N. & Kazilas, M. (2021). Defects and uncertainties of adhesively bonded composite joints. *SN Appl. Sci.* **3**, 769. https://doi.org/10.1007/s42452-021-04753-8

Ouyang, Z., Ji, G., Li, G. (2011). On Approximately Realizing and Characterizing Pure Mode-I Interface Fracture Between Bonded Dissimilar Materials. *Journal of Applied Mechanics, 78(3), 031020–.* doi:10.1115/1.4003366

Ozel, A., Yazici, B., Akpinar, S., Aydin, M. D., & Temiz, Ş. (2014). A study on the strength of adhesively bonded joints with different adherends. *Composites Part B: Engineering*, *62*, 167–174. https://doi.org/10.1016/j.compositesb.2014.03.001

Papadakis, A. Z., Konstantinidis, G. K. and Tsouvalis, N. G. (2018). Long term deep sea exposure effect on the mechanical properties of filament wound composites. ECCM18 - 18th European Conference on Composite Materials 2018

Papanicolaou, G. C., Charitidis, P. J., Mouzakis, D. E., & Jiga, G. (2015). Experimental and numerical investigation of unbalanced boron/epoxy-aluminum single lap joints subjected to a corrosive environment. *Journal of Composite Materials*, *50*(2), 145–157. https://doi.org/10.1177/0021998315571773

Pate, K. D. (2002). Applications of adhesives in Aerospace. *Adhesion Science and Engineering*, 1129–1192. https://doi.org/10.1016/b978-044451140-9/50025-1

Peters, S. T. (2011). *Composite filament winding*. ASM International.

Razavi Setvati, M., Mustaffa, Z., Shafiq, N., & Syed, Z. I. (2014). A review on composite materials for offshore structures. *Volume 5: Materials Technology; Petroleum Technology*. https://doi.org/10.1115/omae2014-23542

Richter, J., (2004) ASME Section X, Class II - A Case Study. Paper presented at the NACE CORROSION 2004, New Orleans, Louisiana

Rice, J. R. (1968). A Path Independent Integral and the Approximate Analysis of Strain Concentration by Notches and Cracks, ASME, *Applied Mechanics*, 35, pp. 379–386

Romanowicz, P. J., & Szybiński, B. (2021). Determination of optimal flat-end head geometries for pressure vessels based on numerical and experimental approaches. *Materials*, *14*(10), 2520. https://doi.org/10.3390/ma14102520

Ross, C. T., Little, A. P., Haidar, Y., & Waheeb, A. A. (2009). Buckling of carbon/glass composite tubes under uniform external hydrostatic pressure. *Strain*, *47*. https://doi.org/10.1111/j.1475-1305.2008.00475.x

Rubino, F., Nisticò, A., Tucci, F., & Carlone, P. (2020). Marine application of fiber reinforced composites: A Review. *Journal of Marine Science and Engineering*, *8*(1), 26. https://doi.org/10.3390/jmse8010026

Seong, M.-S., Kim, T.-H., Nguyen, K.-H., Kweon, J.-H., & Choi, J.-H. (2008). A parametric study on the failure of bonded single-lap joints of carbon composite and aluminum. *Composite Structures*, *86*(1-3), 135–145. https://doi.org/10.1016/j.compstruct.2008.03.026

Sørensen, B.F., Jacobsen, T.K. (2003) Determination of cohesive laws by the J integral approach. Engineering Fracture Mechanics 70: 1841- 1858.

Sorensen, B.F., Kirkegaard, P. (2006). Determination of mixed mode cohesive laws. *Engineering Fracture Mechanics*, 73, 2642–2661.

Sun, L., Li, C., Tie, Y., Hou, Y., & Duan, Y. (2019). Experimental and numerical investigations of adhesively bonded CFRP single-lap joints subjected to tensile loads. *International Journal of Adhesion and Adhesives*, *95*, 102402. https://doi.org/10.1016/j.ijadhadh.2019.102402

Tsouvalis, N. G., & Karatzas, V. A. (2010). An investigation of the tensile strength of a composite-to-metal adhesive joint. *Applied Composite Materials*, *18*(2), 149–163. https://doi.org/10.1007/s10443-010-9137-z

Tsouvalis, N. G., Zafeiratou, A. A. & Papazoglou, V.J. (2000). Parametric study of composite cylinders under hydrostatic load: Effect of end closures and lay-up

Tsouvalis, N. G. (1998). Analysis and Design of Composite Material Crafts.

Volkersen, O., 1938. Die Niektraftverteiling in Zugbeanspruchten mit Konstanten Laschenquerschritten. Luftfahrtforschung 15, 41-47.

Yudhanto, A., Watanabe, N., Iwahori, Y. (2011). Thickness Effect on the Damage Mechanism in Stitched Carbon/Epoxy Composites containing Circular Holes, Inovasi, 19 (3), 16-32

Zhan, X., Gu, C., Wu, H., Liu, H., Chen, J., Chen, J., & Wei, Y. (2016). Experimental and numerical analysis on the strength of 2060 al–li alloy adhesively bonded t joints. *International Journal of Adhesion and Adhesives*, *65*, 79–87. https://doi.org/10.1016/j.ijadhadh.2015.11.010

Zhao, X. (1991). Stress and failure analysis of adhesively bonded joints. PhD Thesis

An overview of assembly tooling for adhesive bonding. (2005). *Materials Technology*, *20*(2), 68–73. https://doi.org/10.1080/10667857.2005.11753112

American Society for Testing and Materials – ASTM. ASTM D5573: Standard Practice for Classifying Failure Modes in Fiber-Reinforced-Plastic (FRP) Joints. ASTM; 2005